UNIVERSITÀ DEGLI STUDI DI TRIESTE

UNIVERSITÀ DEGLI STUDI DI TRIESTE

XXXVI Ciclo del Dottorato di Ricerca in Fisica

Project funded by the European Union's Horizon 2020 research and innovation program under the Marie Skłodowska-Curie Grant Agreement No. 860553.

Ultrafast electronic and lattice dynamics in Al/Fe_2O_3 composite probed with the FERMI free electron laser

Settore scientifico-disciplinare: FIS03/ FISICA DELLA MATERIA

Candidate
Ettore Paltanin

Coordinator
Prof. Francesco Longo

Supervisor
Dr. Claudio Masciovecchio

Co-Supervisor
Dr. Riccardo Mincigrucci

Anno Academico 2022-2023

It is true, I never assisted the sun materially in his rising, but, doubt not, it was of the last importance only to be present at it.

— Henry David Thoreau

Light and matter are both single entities, and the apparent duality arises in the limitations of our language.

— Werner Heisenberg

Science is not only compatible with spirituality; it is a profound source of spirituality.

— Carl Sagan

Abstract

The aim of the thesis is that of investigating ultrafast dynamics in Al/Fe_2O_3 composite using time-resolved and chemically selective spectroscopic techniques. The experiments discussed in the thesis were performed at the EIS-TIMEX and EIS-TIMER beamlines at the FERMI free electron laser (FEL) and consisted of time-resolved absorption spectroscopy and four wave mixing (FWM) measurements with ultrashort extreme ultraviolet (EUV) pulses. TIMEX is an instrument developed to investigate matter in extreme conditions with a pump-probe approach. The beamline is equipped with a robust pump-probe setup that exploits the seed laser for users (SLU) and the FEL radiation, providing a time resolution of ~ 100 fs with a jitter of just a few fs (< 10 fs). An introduction of FEL radiation and a description of FERMI and of the aforementioned beamlines is followed by a discussion of the main project: the sudy of the ultrafast dynamics of the heterogeneous solid-state redox reaction between Al and Fe_2O_3. The innovation of this work consists of using EUV pulses to investigate the reaction dynamics between two (heterogeneous) reaction partners, while, so far, spectroscopic investigations in this wavelength range have been restricted to intramolecular process in the gas phase. Al/Fe_2O_3 is the prototypical composition of energetic materials that, upon activation, results in the commonly known thermite reaction. A lot of research has been conducted on the family of thermite reactions, because they have several applications in different fields, ranging from propellants, explosives and pyrotechnics to industrial waste treatment and material synthesis. The experiment was performed at the TIMEX end-station, photoexciting the sample with the laser at 785 nm to initiate the reaction and probing the process with chemical selectivity at the Fe $M_{2,3}$ edge absorption edge and at the Al $L_{2,3}$ edge absorption edge. The experiments conducted during my stay at FERMI proves the capability of EUV transient absorption spectroscopy, which is sensitive to the variations of the atomic species oxidation state, to investigate chemical reaction dynamics. A blue shift of the isosbestic point in the transient absorption trace of Fe_2O_3 has been observed and it has been associated with the formation of a small polaron in Fe_2O_3. We have compared the behaviour of the prototypical thermite mixture in the transient absorption traces with bare hematite deposited on parylene. We attributed the substrate dependent spectral divergences to the injection of electrons from Al to Fe_2O_3, supporting this interpretation with the simulations of the static absorption spectra of Fe_2O_3 and one of the expected reaction intermediates, FeO. The calculations were performed by our CALTECH collaborators.

Then, a selection of experiments performed at FERMI will be shortly treated. In these projects the staff of the beamline was largely engaged for the development and the post-processing. The experimental techniques that were explored are of interest for this thesis because they differ from the conventional transient grating (TG) and they have the capability to be employed for investigating chemical problems.

In conclusion, the main topic of my PhD project has been that of moving the first steps towards the investigation of heterogeneous solid-state chemical reaction with the FERMI FEL light source. Although we did not observe all the steps of the reaction, we were able to monitor chemically relevant dynamics, *i.e.* small polaron formation and an electron transfer process. The work conducted in this project shows that chemically-selective and time-resolved spectroscopy is a valuable tool for studying chemical reactions. Additionally, I had the chance to actively participate in the development of novel EUV based techniques beyond conventional TG at the TIMER beamline.

Contents

Preface

The aim of my PhD project is that of investigating ultrafast electronic processes and consequent lattice dynamics in materials with a focus on chemical processes by using ultrashort extreme ultraviolet (EUV) pulses. The main goal of my research has been that of paving the way towards monitoring the evolution of an heterogeneous solid-state chemical reaction. In order to face this scientific challenge, I have exploited the technique of time-resolved EUV spectroscopy, which merges a sub-picosecond time-resolution together with the intrinsic chemical selectivity associated with core-hole transitions that are excited by EUV photons. The original aspect of the project is that of using ultrashort EUV pulses to study the kinetics of a heterogeneous process, while, so far, ultrafast EUV light sources have been employed only to study intramolecular reactions in the gas phase. The experiments presented were performed at the elastic inelastic scattering (EIS) beamlines, TIMEX and TIMER, exploiting the EUV radiation produced by the FERMI free-electron laser (FEL). TIMEX is an instrument developed to investigate matter in extreme conditions with a pump-probe approach. The beamline features a robust pump-probe setup that exploits the combination of the seed laser for users (SLU) and the FEL. The TIMER beamline is designed with a non-collinear geometry to perform transient grating (TG) experiments, opening the possibility to perform different kinds of four wave mixing (FWM) experiments with elemental specificity to probe chemical phenomena with novel experimental techniques.

The first part of the thesis is dedicated to the fundamentals of the generation of FEL radiation and then to a description of the FERMI facility. Basics aspects involving the experimental techniques employed are provided, followed by an elucidation of the EIS beamlines and their capabilities. The central body of the thesis is dedicated to the main project: the investigation of the heterogeneous solid-state redox reaction between α-Fe_2O_3 and Al. As a beamline scientist at FERMI, I participated several beamtimes as user support, but I also had the chance to work more extensively on some projects and to contribute to the development of innovative experimental techniques. In the last part of the thesis, I will present such techniques, in which the non-collinear geometry is merged with non-linear effects in the EUV range to foster experimental tools for tackling the challenge of studying chemical phenomena with sub-picoseconds time-resolution.

Among them, inelastic coherent scattering and self-diffraction are novel techniques which exploit non-linear effects, namely FWM, and a noncollinear geometry to generate a signal characterized by an enhanced contrast and also to open the way to measure properties that are not directly accessible with other techniques, *e.g.* electronic coherences in the case of inelastic scattering.

Structured illumination microscopy is a well-known technique with visible light, but the work reported here aims to pave the way towards the extension of super-resolution microscopy in the EUV and X-Rays region of the electromagnetic spectrum.

Chapter 1

Introduction

1.1 Principle of functioning of free electron lasers

1.1.1 Synchrotron Radiation

Bremsstrahlung [1] is a German term that is used in physics to refer to the production of electromagnetic radiation that occurs when a charged particle in motion is decelerated. Basically, the reduction of the kinetic energy of the particle is balanced by the emission of electromagnetic radiation according to the principle of energy conservation. Synchrotron radiation is a specific type of Brehmsstrahlung, *i.e.* magnetobrehmsstrahlung [2, 3], which occurs when a relativistic particle is decelerated by a force that acts perpendicularly to its velocity. This particular situation, where the acceleration is perpendicular to the velocity ($\vec{a} \perp \vec{v}$), leads to the natural generation of electromagnetic radiation as a consequence of Maxwell's equations. The power of the emitted radiation is calculated using the relativistic Larmor formula [4]:

$$P_\gamma = \frac{1}{6\pi\epsilon_0}\frac{q^2a^2}{c^3}\gamma^4 \tag{1.1}$$

where ϵ_0 is the vacuum permittivity ($8.85 \times 10^{-12}\ F \cdot m$), q is the charge of the particle ($-1.6 \times 10^{-19}C$ is the charge of an electron), a is the magnitude of the acceleration, c is the speed of light ($3 \times 10^8 m/s$) and γ is the Lorentz factor, which quantifies how much the measurement of a physical quantity of an object varies as the object is moving with a certain velocity with respect to a reference frame. The Lorentz factor is defined as follows:

$$\gamma = \frac{1}{\sqrt{1-\beta^2}} \qquad \text{with} \quad \beta = \frac{v}{c} \tag{1.2}$$

The generation of Brehmsstrahlung and synchrotron radiation is a phenomenon that encompasses several fields of research, such as astrophysics, particle physics and materials science. Understanding these processes is crucial for controlling the properties of the generated radiation, which is a powerful tool for developing new technologies and gaining insights into the behavior of matter at the atomic and subatomic scales.

Synchrotron radiation is naturally emitted when charged particles move through magnetic fields in deep space, *e.g.* ions that orbit around supermassive black holes[5], electrons trapped in the intense magnetic field around a pulsar [6], electrons that interact with plasma in the intergalactic medium [7]. Synchrotron radiation is characterized by some distinctive features: a power-law distribution for the frequencies of the electromagnetic radiation produced and a specific polarization.

These features make it a valuable tool in astrophysics for probing the properties of electromagnetic fields thanks to the presence of relativistic charged particles.

Synchrotron radiation is as well artificially produced in particle accelerators, where charged particles, *i.e.* electrons, are accelerated to relativistic velocities in the presence of magnetic fields. The generation of synchrotron radiation intrinsically occurs in these facilities and was first observed in 1947 [8], though at the time it was considered merely a nuisance and a source of energy loss. The more intense the electromagnetic radiation produced, the greater the energy loss.

Physicists began to carry out parasitic measurements using synchrotron radiation (first-generation light sources), and what was initially considered a side effect of particle physics experiments soon became a valuable resource for science. Thanks to their high brilliance and tunability, storage rings dedicated to material science and fundamental research in physics were built all over the world starting from the 1970s (second-generation light sources), and synchrotron facilities became established as the preferential sources for many experimental techniques that relied on high-energy photons, such as X-rays and UV radiation.

Further developments led to the installation of wigglers and undulators in straight sections alternating with bending magnets in curved sections, resulting in a third generation of synchrotrons that are optimized for increased brightness.

Wigglers and undulators are insertion devices consisting of two parallel arrays of electromagnets with alternating polarities that generate a spatially periodic magnetic field transverse to the longitudinal axis of the wiggler. These devices have revolutionized synchrotron radiation sources by producing beams of high-energy photons that are brighter and more tunable than those generated by the first generations of synchrotrons. The resulting increase in brightness has enabled the development of new experimental techniques that allow researchers to study matter at previously inaccessible levels of detail.

Synchrotron radiation produced in third generation storage rings possesses remarkable qualities:

- High brilliance, up to 10^{19} photons $\cdot s^{-1} \cdot mm^{-2} \cdot mrad^{-2} / 10^{-3} \dfrac{\Delta\lambda}{\lambda}$, being λ the electromagnetic radiation wavelength;
- Tunability of the light produced and possibility of finely selecting the wavelength;
- Possibility of controlling the polarization;
- Low emittance (small angle of emission) and high collimation.

Such features have made synchrotron radiation appealing for several kinds of experimental techniques such as X-Ray diffraction, X-Ray Absorption Spectroscopy (XAS), Resonant Inelastic X-Ray Scattering (RIXS), Near-Edge X-Ray Fine Structure (NEXAFS), Angle-Resolved X-Ray Photoemission Spectroscopy (XARPES).

1.1.2 Free electrons and undulators

The following section is based on Ref. [9–11] and it aims to provide a brief description of FEL radiation properties and their underlying physical principles.

In the context of particle accelerators, the term free electrons is used to refer to unbound electrons, *i.e.* electrons that are not bound to an atom. When free electrons are accelerated to relativistic velocities and injected in undulators along the longitudinal axis, the emission is bright and confined in a small cone which is centered on the instantaneous velocity vector. As stated above, an undulator consists of a pair of arrays of magnets which produce a periodic magnetic field

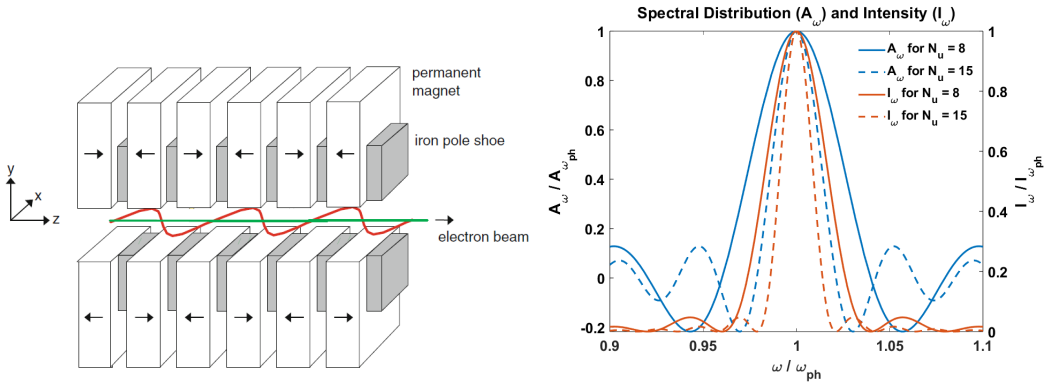

(a) (b)

Figure 1.1: On the left panel, the illustration schematically depicts an undulator and its conventional axis orientation. The red line traces the trajectory of an electron beam as it interacts with the periodic magnetic field. The image is taken from Ref [11]. On the right panel, the plot shows spectral distribution (blue, vertical axis on the left) and intensity(orange, vertical axis on the right) for FEL undulator radiation in the case of 8 (solid lines) and 15 (dashed lines) oscillations (wiggles).

oriented vertically. By convention, the z axis is the longitudinal axis of the undulator, the y axis is the transversal vertical axis and the x axis is the transversal horizontal axis (see Fig.1.1a). The magnetic field produced by the undulator is oriented on the y axis and it varies sinusoidally along the z axis with a period λ_u:

$$\vec{B} = B_0 \cdot cos(k_u z) \qquad \text{with} \quad k_u = \frac{2\pi}{\lambda_u} \tag{1.3}$$

The electron beam entering the undulator with a relativistic velocity in z interacts with the magnetic field of eq. 1.3 and wiggles periodically in the xz plane in the transverse direction x. The transverse acceleration of a relativistic electron subjected to the magnetic field of the undulator is given by the Lorentz equation:

$$\gamma\, m_e \frac{d\,\vec{v}}{dt} = -e\,(\vec{v} \times \vec{B}) \tag{1.4}$$

which in turn leads to the pair of coupled equations:

$$\frac{d^2\,\vec{x}}{d^2t} = \frac{e}{\gamma m_e} B_y \frac{d\,\vec{z}}{dt} \qquad \frac{d^2\,\vec{z}}{d^2t} = \frac{e}{\gamma m_e} B_y \frac{d\,\vec{x}}{dt} \tag{1.5}$$

whose first order solution is obtained iteratively by considering $\dot{z} \approx \beta c$ and $\dot{v_x} \ll \dot{v_z}$. For the derivation, the interested reader could address Ref. [11]. The solution is the electron trajectory:

$$x(z) = \frac{K}{\gamma\beta k_u}\, sin(k_u z) \tag{1.6}$$

and the transversal velocity is given by:

$$v_x(z) = \frac{Kc}{\gamma}\, cos(k_u z) \tag{1.7}$$

where K is a dimensionless quantity of great relevance in FEL physics known as the undulator parameter:

$$K = \frac{eB_0}{m_e c k_u} \tag{1.8}$$

In order to obtain the second-order solution, the assumption of a constant longitudinal velocity ($\dot{z} \approx \beta c$) can no longer be considered justifiable. The modulus of the longitudinal velocity would then be written as:

$$v_z(t) = \sqrt{v^2 - v_x^2} = \sqrt{c^2\left(1 - \frac{1}{\gamma^2}\right) - v_x} = \left(1 - \frac{1}{2\gamma^2}\left(1 - \frac{K^2}{2}\right)\right)c - \frac{cK^2}{4\gamma^2} cos(2\omega_u t) \tag{1.9}$$

with $\omega_u = \langle\beta\rangle c k_u$. The average longitudinal velocity then becomes:

$$\langle v_z \rangle = \left(1 - \frac{1}{2\gamma^2}\left(1 - \frac{K^2}{2}\right)\right)c \equiv \langle\beta\rangle c \tag{1.10}$$

Once the average longitudinal velocity has been determined, it is convenient to move from a static coordinate system to a coordinate system which is moving to the average longitudinal velocity of the electrons. This is achieved through the Lorentz transformations:

$$t^* = \langle\gamma\rangle\left(t - \frac{\langle\beta\rangle z}{c}\right) \approx \langle\gamma\rangle t(1 - \langle\beta\rangle^2) = \frac{t}{\langle\gamma\rangle}$$

$$x^* = x = \frac{K}{k_u \gamma} sin(\omega_u t)$$

$$z^* = \langle\gamma\rangle(z - \langle\beta\rangle ct) \approx -\frac{K^2}{8\gamma k_u \sqrt{1 + \frac{K^2}{2}}} sin(2\omega_u t)$$

resulting in:

$$x^* \propto sin(\omega^* t^*) \qquad and \qquad z^* \propto sin(2\omega^* t^*) \tag{1.11}$$

where:

$$\omega^* = \langle\gamma\rangle\omega_u = \langle\gamma\rangle c k_u \approx \gamma c k_u \left(1 + \frac{K^2}{2}\right)^{-1/2} \tag{1.12}$$

Therefore, the motion of the electron inside the undulator in the moving frame could be decomposed to a transversal harmonic oscillation of frequency $\omega^* = \langle\gamma\rangle\omega_u$ and a small longitudinal oscillation of double the frequency ($2\omega^*$).

The frequency of the photon emitted by such electron in the laboratory frame is affected by the Doppler shift because of the motion of the source with respect to the observer:

$$\omega_{ph} = \frac{\omega^*}{\langle\gamma\rangle(1 - \langle\beta\rangle cos\theta)} \tag{1.13}$$

Invoking eq. 1.12, the wavelength of the undulator radiation λ_{ph} could be written in terms of the undulator period λ_u :

$$\lambda_{ph} = \frac{2\pi c}{\omega_{ph}} = \frac{2\pi c}{\omega^*} = \frac{2\pi}{k_u}\langle\gamma\rangle(1 - \langle\beta\rangle cos\theta) = \lambda_u\langle\gamma\rangle(1 - \langle\beta\rangle cos\theta) \tag{1.14}$$

For relativistic electrons in a magnetic field, the emitted radiation propagates in the forward direction and falls within a narrow cone with an aperture angle $1/\gamma$, hence the higher the Lorentz factor the more the radiation is concentrated in the forward direction. The central axis of the cone is aligned with the tangent to the instantaneous velocity of the electrons. The direction of such tangent varies along the sinusoidal trajectory that the electrons follow inside the undulator, and the maximum value of the angle between the tangent and the longitudinal axis of the undulator is determined by:

$$\theta_{max} = \left|\frac{dx}{dz}\right|_{max} \approx \frac{K}{\gamma} \tag{1.15}$$

In the case of FEL undulators, $K \leq 1$ and so $\theta_{max} \leq 1/\gamma$, with $\gamma \gg 1$. This property is critical for FEL radiation because the radiation field collects contributions from various sections of the trajectory that interfere provided that the spatial overlap is large enough. Consequently, the spectrum of undulator radiation in the forward direction is not continuous but almost monochromatic, consisting of a narrow spectral line at a well-defined frequency and its odd higher harmonics.

Given these considerations, it is possible to approximate $cos\theta$ by a truncated Taylor series ($cos\theta \approx 1 - \theta^2/2$). Recalling the expression of average longitudinal velocity $\langle\beta\rangle$c from eq. 10, the angular dependent undulator radiation in the proximity of the z axis can be expressed as:

$$\lambda_{ph} = \frac{\lambda_u}{2\gamma^2}\left(1 + \frac{K^2}{2} + \gamma^2\theta^2\right) \tag{1.16}$$

The total radiant power of spontaneous emission of undulator radiation summed over all harmonics and all angles is calculated starting from the Larmor formula (see eq. 1.1) and the terms of the undulator parameters, and it is expressed as follows:

$$P_{rad} = \frac{e^2 c\gamma^2 K^2 k_u^2}{12\pi\epsilon_0} \tag{1.17}$$

To estimate the spectral distribution of undulator radiation A(ω), one can consider that when an electron passes through N_u periods of oscillation (wiggles), it generates a pulse train with a duration of $T = N_u \lambda_{ph} c^{-1}$. As mentioned earlier, the emission of undulator radiation in a free-electron laser is narrow with a well-defined frequency, and since it has a finite pulse duration, its bandwidth is determined by the Fourier transform of the pulse duration.

$$A(w) = E_0 \int_{-T/2}^{T/2} e^{-i(\omega_{ph}-\omega)t} dt = 2E_0 \, \frac{sin\big((\omega_{ph}-\omega)T/2\big)}{\omega_{ph}-\omega} = T \, E_0 \, sinc\left(\pi N_u \frac{\omega_{ph}-\omega}{\omega_{ph}}\right) \tag{1.18}$$

While the spectral intensity is

$$I(\omega) \propto \big|A(\omega)\big|^2 \propto sinc^2(\xi) \qquad with \qquad \xi = \pi N_u \frac{\omega_{ph}-\omega}{\omega_{ph}} \tag{1.19}$$

Therefore, the emission of undulator radiation for the first harmonic[1] appears as a peak with its maximum at the well-defined frequency ω_{ph}, and its bandwidth is transform-limited, approximately equal to $\omega_{ph}/\pi N_u$, see Fig. 1.1b.

1.1.3 Interaction of the electron bunch with a radiation field inside an undulator

If one considers an electromagnetic field propagating along the undulator z axis and polarized in the x axis, it would be described by

$$\vec{E} = E_0 cos(k_l z - \omega_l t + \psi_0) \tag{1.20}$$

where k_l, ω_l and ψ_0 are respectively its momentum, its frequency and its phase. The variation of the energy of the electron bunch caused by the interaction with the co-propagating light is given by

$$\begin{aligned} \frac{d(\gamma mc^2)}{dt} &= -ev_x(t)E_x(t) = -\frac{ecK}{\gamma} \, cos(k_u z) E_0 cos(k_l z - \omega_l t + \psi_0) = \\ &= -\frac{ecKE_o}{2\gamma} \left[\underbrace{cos\big((k_l + k_u)z - \omega_l t + \psi_0\big)}_{\text{slowly varying term}} + \underbrace{cos\big((k_l - k_u)z - \omega_l t + \psi_0\big)}_{\text{fast oscillating term}} \right] \end{aligned} \tag{1.21}$$

where the phase factor ψ_0 accounts for the fact that the radiation field will always be shifted with respect to sinusoidal motion of the electron bunch, being the latter much larger in size than the wavelength of the oscillating electromagnetic field. Eq. 1.21 could be conveniently rewritten in a simpler form as follows:

$$\frac{dW}{dt} = -\frac{ecK}{\gamma} \Big[cos\psi + cos\chi \Big] \tag{1.22}$$

[1] In the simple derivation presented in this text, the longitudinal oscillations of the velocity are neglected, and only the generation of the first harmonic can be analyzed within this approximation.

where ψ is the slowly varying function, which in FEL physics is referred to as the ponderomotive phase. This is a key quantity because its value determines whether the radiation field is gaining energy from the electron bunch or vice versa. Energy transfer from the electron bunch to the radiation field occurs when the light is slipping[2] over the bunch with a specific phase difference and this condition is in turn satisfied only for well-defined wavelengths:

$$\lambda_{ph} = \frac{n\lambda_u}{2\gamma^2}\left(1 + \frac{K^2}{2}\right) \qquad \text{with} \quad n = 2m + 1 and m \in \mathbb{N} \tag{1.23}$$

These wavelengths correspond to the fundamental spontaneous undulator radiation and its odd harmonics at $\theta = 0$. This is the reason why spontaneous undulator emission can act as a seed for the electron bunch from which it has been generated. That is a process of great relevance, because it lies at the root of SASE (self-amplified spontaneous emission) FELs. In this situation (λ_{ph} satisfying the condition given by eq. 1.24), the ponderomotive phase could be considered constant $\psi = \text{const}$ and the fast oscillating term $cos\chi$, which completes two oscillations over an undulator period, averages out to zero. This leaves only the first cosine in eq. 1.22, which we assumed to be constant, and by looking at different values of the ψ_0 phase from eq. 1.21 we can depict three main scenarios:

- $\psi_0 = -\frac{\pi}{2}$:no net energy exchange;
- $\psi_0 = 0$: sustained energy transfer from the electrons to the light;
- $\psi_0 = -\pi$ sustained energy transfer from the light to the electrons.

The ponderomotive phase is useful to define an internal coordinate for the electron bunch:

$$\xi = \frac{\psi + \pi/2}{2\pi}\ \lambda_{ph} \tag{1.24}$$

According to this definition, ξ is defined in such a way that $\xi = 0$ corresponds to the $\psi_0 = -\pi/2$ phase, which identifies the condition of no energy transfer between the light and the electrons at that position in the bunch. All the other values of ξ are associated with a transfer of energy in either direction.

The undulator radiation with a wavelength equivalent to that of the seed λ_{ph} is produced only by electrons with a specific value of energy, called the resonant electron energy W_r:

$$W_r = \gamma_r m_e c^2 \tag{1.25}$$

where the resonant Lorentz factor γ_r is found by λ_{ph}, λ_u and the undulator parameter K:

[2]Light is moving faster than the electron bunch, not only because c is greater than $\langle v_z \rangle$, but also because electron are wiggling transversally on the horizontal plane of the undulator.

$$\gamma_r = \sqrt{\frac{\lambda_{ph}}{\lambda_u}\left(1 + \frac{K^2}{2}\right)} \tag{1.26}$$

Once the resonant condition is established, the energy of an electron, W, may be defined in a relative scale with respect to the resonant energy:

$$\eta = \frac{W - W_r}{W_r} = \frac{\gamma - \gamma_r}{\gamma_r} \qquad \text{with } |\eta| \ll 1 \tag{1.27}$$

At this point, we can write the FEL pendulum equations, which represent a milestone in FEL physics and owe their name to the fact that they are formally similar to the equations that describe the motion of a classical pendulum:

$$\frac{d\psi}{dt} = 2k_u c\eta \tag{1.28a}$$

$$\frac{d\eta}{dt} = -\frac{eE_0K}{2mec\gamma_r^2} cos\psi \tag{1.28b}$$

In this framework where η and ψ are chosen as coordinates for the motion of the electrons inside the undulator, hence the electron trajectories can conveniently be described in the so called phase space, as a function of η and ψ. The power of this representation lies in its simplicity for depicting the dynamics of interaction between electrons and electromagnetic radiation inside the undulator. For instance, an electron which has coordinates (0,0) will be stationary in the phase space throughout the undulator. Electrons that are at resonance ($\gamma = \gamma_r$, $\eta = 0$) will have no net energy exchange with the radiation field, while if $\eta > 0$, the electrons will lose more energy than they gain with a net energy transfer to the radiation field.

1.2 Low gain and high gain free electron lasers

The derivation reported so far is based on the assumption of a light wave with constant amplitude interacting with the electron bunch. This assumption is reasonable in the case of a low gain FEL. In a low gain FEL an electron bunch passes several times through the undulator and it is either seeded by an external source such as a laser (FEL amplifier) or by the spontaneous undulator emision (FEL oscillator). The distinctive component of a low-gain FEL is the optical cavity. The light wave is reflected between the two mirrors of the optical cavity and it interacts several times with the recirculated electrons in the undulator. At each cycle the intensity of the light wave only increases by just a small percentage (from which the name low-gain FEL), but this sort of device can anyway reach high output power because the number of turns can be very large. The gain function in a low-gain FEL is defined as the relative increase in the intensity of the light wave during each passage through the undulator. Therefore, the gain follows the same trend as η. In

order for the gain to be positive, η must also be positive. Additionally, it is important for the electron energy, W, to be in proximity to the resonant energy, W_r, to ensure that the relative energy deviation, η, remains smaller than the bandwidth of the undulator radiation emission. The latters are the conditions to be fulfilled according to the Madey theorem[12] to obtain a significant gain in an FEL driven by a seed radiation. This design of FELs only works in the infrared and visible regimes, where it is feasible to build efficient optical cavities. FELs in the EUV and X-rays have to rely on a different strategy for achieving light amplification, due to the technical challenges of realizing optical resonators in these wavelength intervals. These kinds of FELs are named high-gain FELS and they are designed to reach light amplification through a single pass within a long array of undulator magnets. Therefore, the intensity of the radiation increases considerably along the undulator and the assumption of constant intensity at the base of low-gain FEL theory becomes inadequate in this scenario. The exponential growth of intensity in FELs is attributed to a phenomenon called microbunching. This process enables a large number of electrons to radiate coherently, which is fundamental to one of the defining characteristics of FEL radiation: its brightness. Indeed, the intensity of radiation in a high-gain FEL is proportional to N^2 (where N is the number of electrons in the electron bunch), whereas the intensity of undulator radiation is only proportional to N. Concentrating a large number of electrons ($\sim 10^9$) in a region smaller than a unit of the radiation wavelength[3] would be impossible in the EUV / X-Rays, because of the charge repulsion among many electrons in a confined volume. This problem is overcome with microbunching. In the electron beam, the electrons that are in phase with the radiation field will gain kinetic energy and hence they will be slightly accelerated, whilst the electrons which are not in phase with the radiation field will lose kinetic energy and will be decelerated, causing an overall modulation of the longitudinal velocity. This process results in a modulation of the space charge density, which effectively concentrates electrons into small groups (*i.e.* microbunches), which are individually shorter than the wavelength of light. Such modulation plays a crucial role by grouping the electrons at the locations of the electron bunch where the exchange of energy from the electrons to the radiation is maximized. As the charge density modulation becomes more pronounced along the undulator, the intensity of the radiation is as well progressively augmenting because of the increasing number of electrons emitting in phase. These two processes are strongly correlated and therefore a positive feedback loop is established that leads to microbunching and to light amplification. The intensity of radiation will not grow indefinitely, but it grows until the saturation regime is entered (the plateau in Fig. 1.2b). The saturation occurs when the electrons have lost a critical amount of energy by radiation and so they can no longer transfer energy to the radiation field, and they approach regions of the phase space where they actually reverse the process and withdraw energy from the radiation field, which is an undesirable condition for FEL efficiency.

1.3 SASE FELs

In the ideal case of an electron beam with a perfectly homogeneous spatial charge distribution entering the undulator, the lasing process from the electrons would have to be started necessarily by an external perturbation, *i.e.* an oscillating electromagnetic field. In reality, the charge distribution of the electron bunch is never uniform and the small random fluctuations of charge density generates a white noise spectrum which always possesses non-zero Fourier components within the bandwidth of the FEL emission, that is centered at the resonant wavelength of the undulator λ_{ph}. Since the aforementioned feedback loop starts only when the radiation has a wavelength that is close to λ_{ph},

[3] Condensing a large number of electrons in a region smaller than the radiation wavelength would allow the electron beam to be considered as a sort of "macroparticle" with charge N ·e, that would radiate coherently.

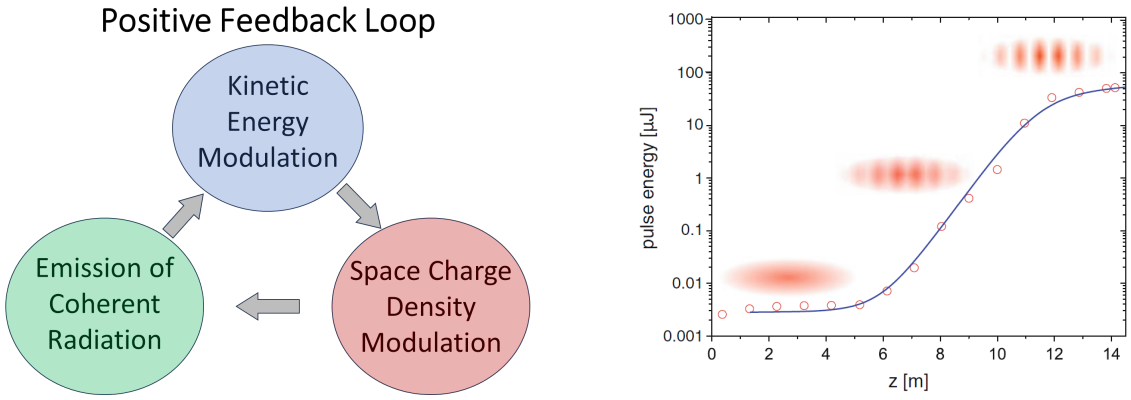

(a) (b)

Figure 1.2: On the left panel, a schematic representation of the positive feedback loop that settles in along the array of undulator magnets of single pass high-gain FELs leading to microbunching and amplification of the radiation. On the right panel, the plot shows the logarithm of the radiation intensity for an FEL pulse as a function of the position of the baricenter of the electron beam in the undulator. The circles are the measured intensities, while the solid line is the fit. The progressive development of the microbunches is schematically depicted. The image is taken from Ref.[11]

this is the only range of wavelengths that is amplified in the FEL radiation generation, while the other wavelengths (outside of the FEL bandwidth) will retain their initial values arising just from the "noise" in the charge distribution of the electron bunch. This mechanism of generation of FEL radiation without an external seed pulse is called self-amplified spontaneuos emission (SASE)[13, 14]. The FEL bandwidth can be quantified by the dimensionless Pierce parameter, ρ_{FEL}:

$$\rho_{FEL} = \frac{1}{4\pi\sqrt{3}} \cdot \frac{\lambda_u}{L_g^0} \tag{1.29}$$

where L_g^0 is the power gain length[4], defined as:

$$L_g^0 = \frac{1}{\sqrt{3}} \left[\frac{4\gamma_r^3 m_e}{\mu_0 \hat{K}^2 e^2 k_u n_e} \right] \tag{1.30}$$

The physical meaning of the gain length is that of indicating the efficiency of the process of amplification of the radiation in an FEL undulator. Intuitively, the gain length is the distance that the bunch has to travel along the undulator in order to increment the power of the FEL radiation by a factor e (base of the natural logarithm). Hence, the shorter the gain length, the more efficient and faster the amplification of radiation, which in turn would result in a larger FEL parameter and a broader spectral bandwidth of the FEL emission. The gain length is related to the transverse emittance ϵ of the electron beam[5] and to its peak current I_{peak} ($L_g^0 \propto \epsilon / I_{peak}$)[15].

[4]The superscript 0 is there to clarify that this is the idealized gain length in the one-dimensional framework of FEL theory, assuming a perfectly mono-energetic electron beam and neglecting space charge effects, energy offset, betatron oscillations and diffraction. In a real FEL, the gain length would be larger, because all the phenomena just mentioned would hamper the exponential grow of the radiation intensity, calling for a longer undulator to reach saturation.

[5]ϵ is a quantity associated with the intrinsic electron beam volume in the phase space

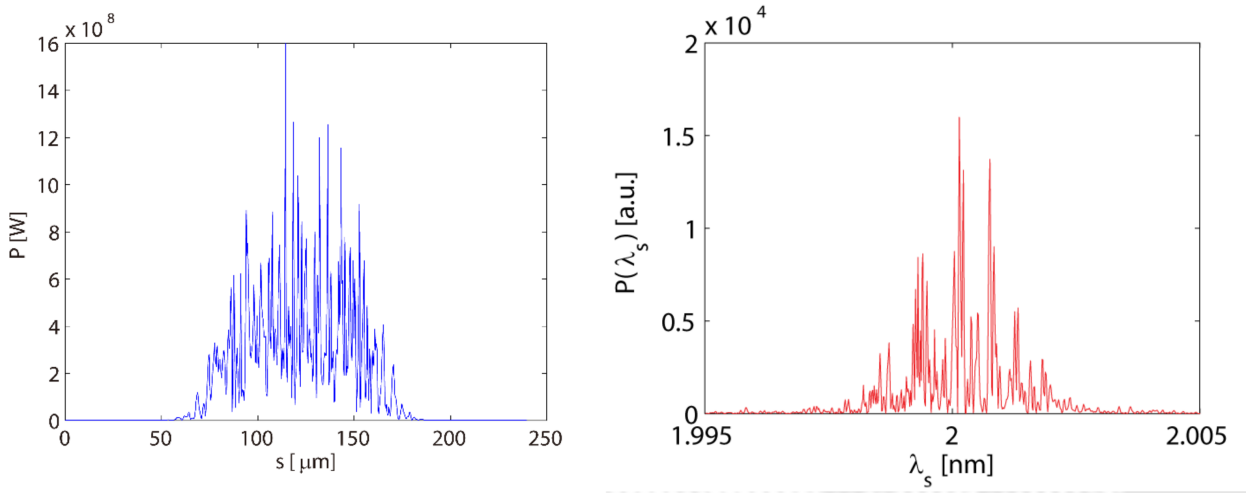

Figure 1.3: On the left pane, typical longitudinal emission profile (temporal profile) of a single shot SASE FEL pulse. On the right panel, typical spectral profile of a single shot SASE FEL pulse. The image is taken from Ref.[16]

The spectral and temporal properties of SASE radiation stem from the stochastic nature of the startup process from shot noise. A portion of the electron bunch can only interact with the radiation produced by the neighbouring portion of the electron bunch which is behind it and whose size can not exceed the total slippage of the electromagnetic pulse over the electron beam $N_u\lambda_{ph}$. In practice, the distance of interaction within the electron beam is limited by a quantity defined as cooperation length, which is substantially given by the slippage over a single gain length:

$$l_c = \frac{\lambda_{ph} L_g^0}{\lambda_u} \tag{1.31}$$

Therefore, at the end of the amplification stage, the SASE emission consists of a train of coherent pulses uncorrelated with one another, each of which is generated by a portion of the beam with a size equal to the cooperation length. Hence, the overall SASE emission is actually a collection of M independent longitudinal modes, where $M = \tau \ / \ l_c$, with τ being the length of the overall electron beam. So the spatial and temporal profiles of the SASE emission are given by a series of spikes whose intensities fluctuate from shot to shot due to stochastic nature of the SASE process (see Fig. 1.3). To some extent, each lasing event is unique and non-reproducible. Since the longitudinal modes have a random phase relation, there is no longitudinal coherence in SASE pulses. However, SASE emission can achieve almost full transversal coherence. This is because the fundamental harmonic is the one with the best overlap with the electron beam and hence it dominates over the higher orders in the amplification stage of a SASE FEL (mode competition).

SASE FELs lack control over spectral and temporal properties of the emission. Nevertheless, the SASE scheme allows for FELs to produce radiation up to the Hard X-Rays, with pulse durations that can be as short as hundreds of attoseconds and extremely high output peak powers, up to GWs[15–18].

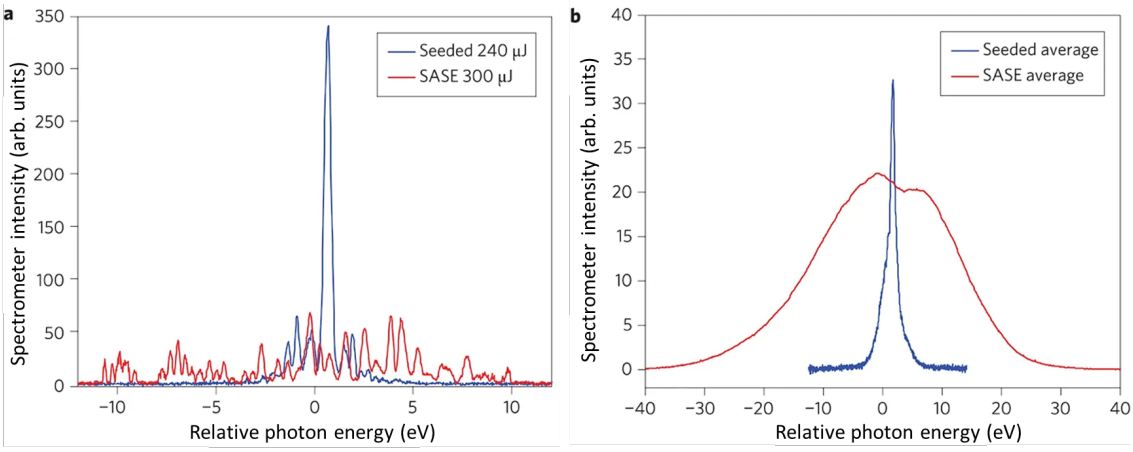

Figure 1.4: In the figures above, a comparison between the spectra obtained with SASE scheme and the self-seeded scheme of the LCLS XFEL are reported. The central photon-energy is 8.3 keV. The left panel shows the single shot spectra, while the right panel displays the spectra averaged over 20000 shots for the SASE scheme and over 200 shots for the self-seeded scheme. The images are taken from Ref.[19]

1.4 Seeded FELs

External seeding offers several advantages over the SASE operation mode. Firstly, it allows for greater control over the central wavelength, bandwidth, intensity, and duration of the FEL output pulses, resulting in a consistent shot-to-shot stability. Furthermore, external seeding enables full coherence, because in addition to the transversal coherence which is gained also with the SASE scheme, the longitudinal coherence is inherited from the seed laser, leading to improved brilliance and quasi Fourier-transform limited pulses (see Fig. 1.4).

However, the crucial factor of this scheme is the seed itself. A seeding source capable of wide tunability is desirable to preserve this important characteristic of FEL light, especially towards shorter wavelengths. This is a major problem, but efforts are made to provide laser-like radiation at shorter than ultraviolet (UV) wavelengths.

Different types of seeding have been developed for FELs. Here, I will just report a brief description. For more thorough explanations, the reader can refer to the citations.

Direct seeding It refers to all the methods that involves the seeding of the electron bunch with a laser-like external source. The wavelength of the seed is the same of the resonant frequency of the undulator, but the intensity of the seed laser is required to be considerably higher than the shot noise in order to efficiently act on the properties of the electron beam[20]. Direct seeding in the EUV/soft X-Rays (SXR) region is performed using the pulses produced with high harmonic generation in gases[21, 22].

Self-seeding This scheme employs the SASE emission generated in a first array undulator, which is then filtered by a monochromator and used to seed the electron bunch in a second chain of undulators, where the amplification takes place up to saturation. After the first undulator series, the electron bunch is delayed and manipulated (the partial microbunching developed is smeared), and it enters the second undulator array where it interacts with the spectrally filtered FEL pulse[19].

There are also different schemes of self-seeding[23], but the idea at the root of it is always that of exploiting the FEL radiation produced in a first stage as a seed.

High-gain harmonic generation (HGHG) This is a scheme to produce FEL radiation by high harmonics of an external laser-like seed radiation pulse. The scheme of single stage HGHG FEL is reported in the top panel of Fig. 1.6. The seed pulse and the electron beam travel together through a short undulator, *i.e.* the modulator, where the energy of the electron beam is periodically modulated according to the properties of the seed pulse. After the modulator, the energy modulation is converted into space charge density modulation by a magnetic dispersive section (DS in Fig. 1.6). The charge density expressed as a function of the internal bunch coordinate results as a series of periodically spaced narrow peaks separated by a distance that equals the seed wavelength (controlled bunching). The structured bunch enters then the second array of undulators, *i.e.* the radiators, where the FEL radiation is produced and amplified to saturation. The difference with respect to direct seeding consists in the fact that the undulators are tuned to amplify a specific harmonic (n) of the seed frequency, so among the terms in the Fourier expansion of the charge density, only the component associated with n^{th} harmonic will be amplified, leading to final FEL emission with frequency $n\omega_0$, with ω_0 being the frequency of the seed. Such scheme has already been successfully implemented[24–26].

Echo-enabled harmonic generation (EEHG) This scheme resembles the HGHG scheme, but there is an additional modulation stage with a second seed pulse, which may have a different wavelength or even the same with respect to the first. The net effect is that of introducing a periodic substructure in the individual microbunches formed in the first modulator, which have a gaussian charge distribution, as in the case of HGHG. The electron beam at the exit of the second magnetic chicane will be spatially modulated in the longitudinal direction with a wavenumber $k = nk_1 + mk_2$, with m,n being integers, 1 and 2 referring to the first and the second seed and being $n > m$. The result is a ditribution of the charge density with largely separated groups (microbunches formed in the first modulator) of narrow peaks close one another within the same group (substructure formed in the second modulator). Such a charge density distribution is characterized by a Fourier expansion that extends to very high order harmonics. The radiator could then be tuned to amplify a frequency which is equal to $n\omega_1 + m\omega_1$, enabling up-conversion factors larger than HGHG to be attained. The EEHG mechanism has already been demonstrated and implemented[27–30].

1.5 The FERMI FEL

The Free Electron Laser for Multidisciplinary Investigations (FERMI) is a HGHG seeded FEL located in Trieste, next to the Elettra synchrotron. It produces ultra-short pulses in the EUV and SXR with a high brilliance ($\sim 10^{13}$ photons per pulse). Thanks to its design of seeded FEL, FERMI is a compact facility and it is less than 500 meters long (see Fig. 1.5). FERMI is highly tunable in terms of photon energies and it can generate an output power of the order of few GWs with a maximum repetition rate of 50 Hz, but the properties that make it a unique light source are the full control of the polarization and the high degree of both transversal and longitudinal coherence. FERMI is a high-gain harmonic generation (HGHG) FEL[31]. A schematic representation that describes graphically the differences between FERMI and a SASE FEL is reported in Fig. 1.7.

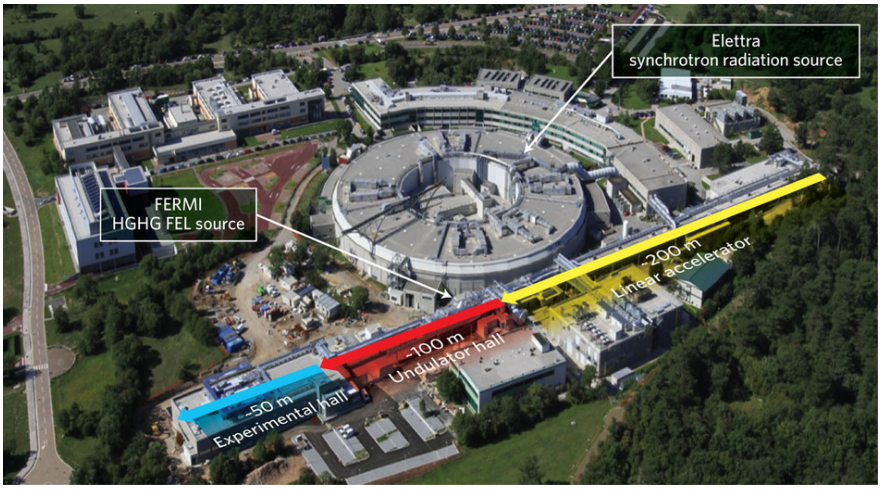

Figure 1.5: Top view of the FERMI free-electron laser and the Elettra synchrotron. The image is taken from Ref.[32]

1.5.1 FEL1 and FEL2

The first portion of FERMI is the linear accelerator which is composed of a photoinjector and two short LINAC sections, LINAC0 which generates an electron beam of 100 MeV and LINAC 1-4 which compresses the beam in time and accelerates the beam up to 1-5 GeV. The undulator hall features two separate lines of undulators. FEL1, the first to operate, is a single stage HGHG line that can produce photons from $\sim$ 100 to 20 nm. FEL2 is a cascaded HGHG line, which operates in the fresh bunch[33], two-stages harmonic upshift configuration[26]. In the first HGHG stage, the electron beam is seeded with a seed pulse that has a shorter duration than the one of the electron bunch ($\tau_{seed} < \tau_{bunch}$). The FEL radiation produced in the first stage is then employed itself as a seed for the electron bunch in the second stage. Between the first and the second stage, the electron bunch is delayed by means of a magnetic chicane (Delay line in Fig. 1.6) by a delay τ, with $\tau > \tau_{seed}$, so that the second seed acts on a portion of the electron bunch that did not interact with first seed pulse, hence the name fresh bunch. Thanks to this configuration, FEL2 allows photons from 20 nm down to 3 nm to be produced, in the SXR regime. A scheme of the layout of FEL1 and FEL2 is reported in Fig. 1.6.

Recently, at FERMI it has been demonstrated the possibility of operating in the EEHG mode as well[30]. The EEHG configuration has some advantages over the two-stage HGHG, namely:

- Smaller sensitivity to the electron bunch imperfections;
- narrower and cleaner spectra, with a smaller jitter around the central wavelength;
- multiwavelength emission without the constraint of harmonic upconversion of the first stage;
- the possibility of reaching shorter wavelengths, down to 2 nm or even further.

For a more comprehensive description of the photoinjector, the LINAC and the undulators of the FERMI FEL the reader can refer to the conceptual design report[34].

1.5.2 Seed laser and SLU

The FERMI Ti:Saphhire (Ti:Sa) femtosecond laser facility[35] generates and shapes the seed pulses employed in the HGHG free-electron lasing process and it is located in a dedicated room above the

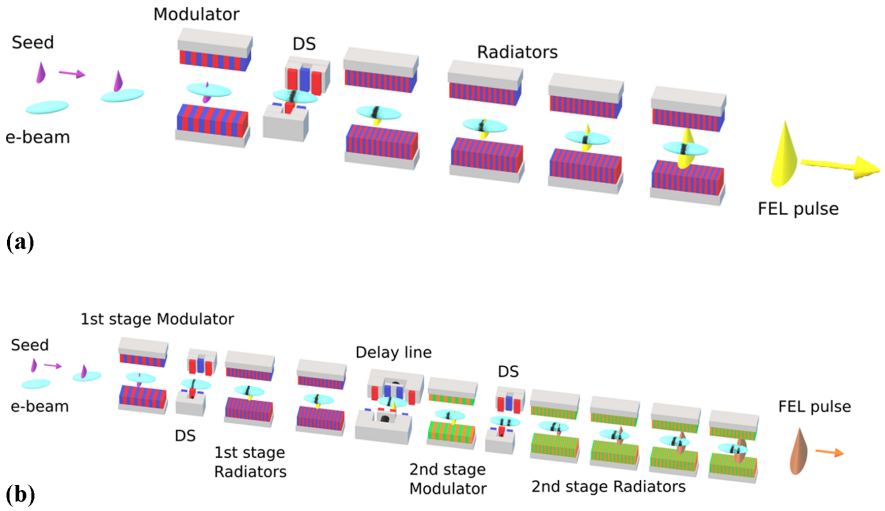

Figure 1.6: Scheme of the HGHG FEL radiation generation for the single stage FEL1 (top panel) and for the cascaded fresh bunch two-stages FEL2 (bottom panel). The picture is taken from Ref. [35]

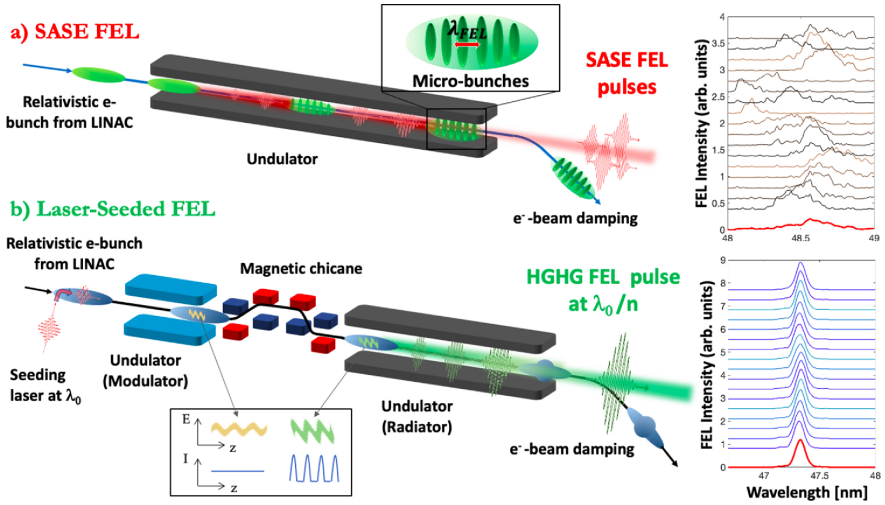

Figure 1.7: Scheme of the generation of radiation in the case of a SASE FEL (top panel) ad in the case of a HGHG FEL (bottom panel). The picture is taken from Ref. [36]

tunnel containing the undulator chain, where two optical tables hold the laser system. The initial pulse train is created by a mode-locked Ti:sapphire oscillator (Vitara-HP from Coherent). This oscillator is synchronized to a timing reference signal given by a stabilized fibre link. The output of the Ti:Sa oscillator is divided to seed two regenerative amplifiers (RegenAmp1 and RegenAmp2 from Coherent). The beam exiting one of the regenerative amplifiers is sent through a customized optical parametric amplifier (OPA) followed by a sequence of frequency mixing processes. Such manipulation allows for a coherent seed pulse which is intense and tunable from $\sim$ 230 - 360 nm (see Fig. 1.8), which is then employed in the seeding of the electron bunch. For an effective bunching of the electron beam, the seed laser needs to exceed a peak power of 100 MW over the whole tunability range. The scheme adopted in the laser facility provides an additional external coherent light source, which is the beam exiting the second regenerative amplifier, with a wavelength that

corresponds to the fundamental emission of the Ti:Sapphire amplifier at 784 nm. The beam is delivered to the experimental hall of FERMI through a low vacuum pipe with a jitter of just a few femtoseconds with respect to the FEL[37, 38]. This source is called the Seed Laser for Users (SLU) and it is a fundamental resource for performing pump-probe experiments. The implementation of the combo HGHG FEL and SLU constitutes a robust experimental tool for performing pump-probe experiments of different nature at the end stations of FERMI.

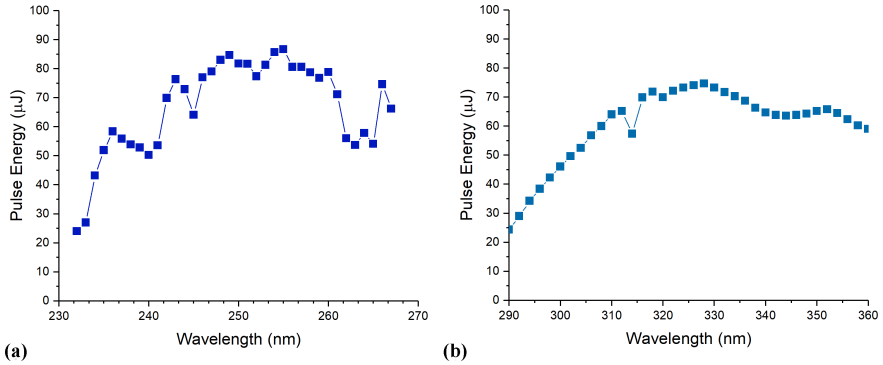

Figure 1.8: Performances of the seed laser over the available tunability range. The picture is taken from Ref. [30]

1.5.3 Photon transport and diagnostics

As the electrons are directed by a series of bending magnets towards a beam dump at the exit of the undulators, the FEL radiation moves towards the experimental hall. It passes through the Photon Analysis Delivery and Reduction System (PADReS), which is a section of FERMI that includes photon diagnostics and FEL beam manipulation optics. The purpose of PADReS is to characterize and modify the photon beam while transporting it to the various end-stations. Fig. 1.9 illustrates the layout of PADReS.

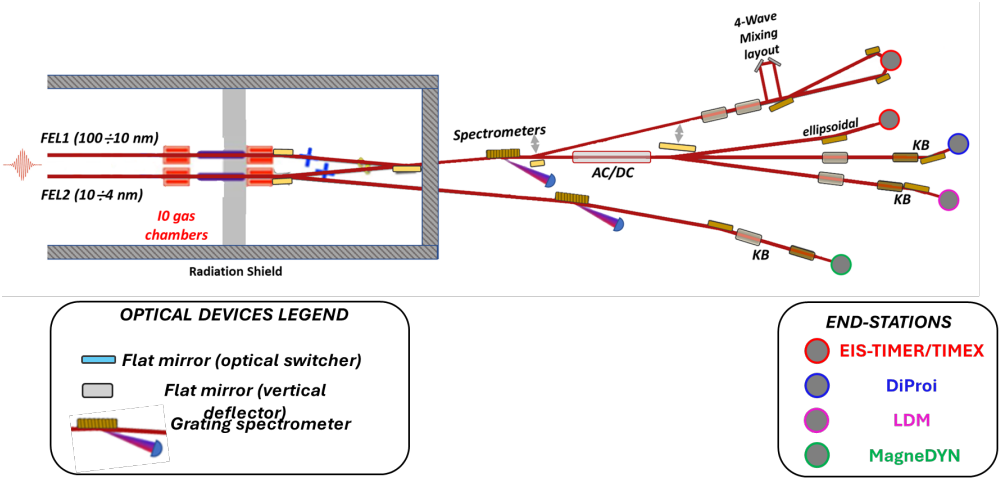

Figure 1.9: Scheme of the beam transport and diagnostic system at FERMI. The picture was provided by Alberto Simoncig via private communication.

For both FEL1 and FEL2, there is a sequence of components in order: a shutter, a beam defining aperture (BDA), a beam position monitor (BPM), an intensity monitor (I0M UH), a differential

pumping system, a gas absorber, two solid-state filter wheels and, on the opposite side of the wall separating the undulator hall and the safety hutch, a second differential pumping system, a second intensity monitor (I0M SH), a second beam position monitor, two additional filter wheels and two sets of two mirrors, which respectively operate on FEL1 (PM1a and PM1b) and on FEL2 (PM2a and PM2a_MD). In the experimental hall, two energy spectrometers (one that is common for four out five end-stations and one that is operating only on MagneDyn beamline) monitor the FEL spectrum.

The aforementioned instruments can be split in two groups: "online" instruments, that characterize the FEL pulses shot-by-shot, and "offline" instruments, whose response time is much larger than the separation between two successive FEL pulses, so they can not be adjusted during the time interval separating one pulse and the following one.

The online devices are the following:

- The intensity monitors are ionization chambers filled with N_2 at $\sim 10^{-5}$ mbar. The incident EUV/SXR radiation generates ion pairs that migrate respectively to the electrode with the opposite polarity, giving rise to a measurable current. These chambers absorb a negligible fraction of the FEL radiation and their response is immediate. Furthermore, they work effectively over the whole wavelength interval spanned by FERMI thanks to their large dynamic range. Hence, they act as real-time diagnostic tools.

- The Pulse-Resolved Energy Spectrometer, Transparent and Online (PRESTO)[39] works for both FEL1 and FEL2 at FERMI. Presto is located along the beam transport and it is composed of a diffraction grating, a YAG screen and CCD camera (Hamamatsu). The diffraction grating separates the different spectral components onto the cerium doped yttrium aluminum garnet (YAG) screen, whose fluorescence is captured by the movable charge-coupled device (CCD) camera, so to avoid damaging the sensor. PRESTO features 3 variable line spacing diffraction gratings, each covering a specific energy range with the first order of diffraction: the Low Energy (LE) grating covers 100-24nm, the High Energy (HE) grating covers 27-6.7nm, and the Super High Energy (SHE) grating covers 12-3.2nm. The majority of radiation is delivered in zeroth order to the endstations, accounting for over 97% of the total output. Therefore, only a small fraction of every FEL shot is employed for the online determination of the photon beam spectral characteristics by working on the first order-diffracted beam. If necessary, up to the third diffraction order can be utilized to extend the measuring range or to determine the wavelength in use with absolute precision.

The following devices belong to offline instruments:

- The BDA consists of a couple of pyramid trunks that can be moved with respect to the ideal beam longitudinal axis and with respect to one another, so to act on the effective beam aperture. The FEL spatial profile is monitored by a CCD camera that captures the fluorescence of a YAG screen generated by the FEL radiation.

- The gas absorber is a 6 meters long cell equipped with a differential pumping system that makes it possible to finely control the flow of gas up to 0.1 mbar. This tool is employed to attenuate the FEL intensity over four orders of magnitude. The standard option for the gas is N_2, but also He, Ne and Ar are available if required, depending on the photon energy of the FEL pulses that need to be attenuated. A considerable uptake can be observed in the gas absorber: it attenuates the FEL intensity while leaving the characteristic of the beam almost

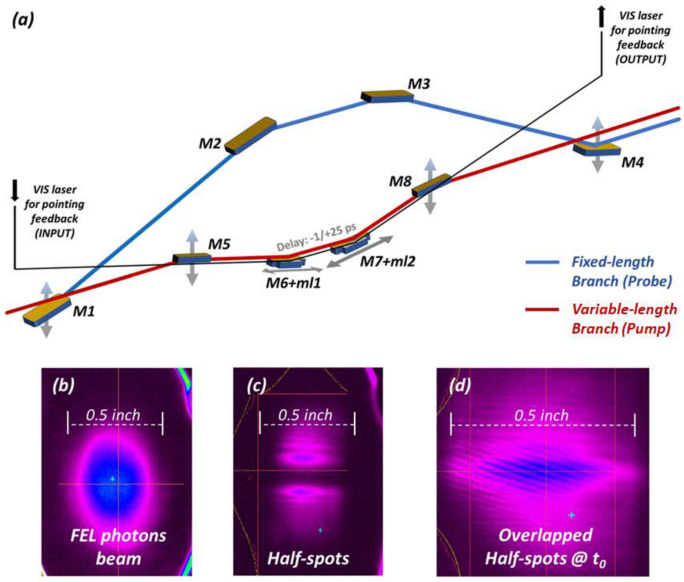

Figure 1.10: Sketch of the AC/DC system (a). The blue line represent the FEL trajectoery along the fixed-length optical branch that will be employed as the probe pulse. The red line depicts the FEL trajectory along the variable-length optical branch. The double-sided arrows show the allowed degrees of freedom of the mirrors. The black line displays the trajectory of the optical laser employed to mimic the pump trajectory in order to detect and monitor the instabilities that arise during a temporal scan. The laser is used as a feedback signal to correct possible misalignments. FEL beam without the AC/DC manipulation on a far-field Ce:YAG screen (b). Split FEL beams on the same YAG screen as **b**. Overlapped and synchronized FEL beams (c), identified by the appearence of interference fringes. The figure is taken from Ref. [40].

unaffected[6]. The latter is an important consideration, because other strategies of attenuating the FEL intensity, e.g. modifying the current of the dispersive section, varying the seed laser intensities, detuning undulators, may have more relevant effects on the properties of the pulses, such as spectral and temporal profiles.

- Solid-state filters are placed along the beam transport. PADReS features 4 filter wheels, two in the undulator hall and two in the experimental hall, that are equipped with different sets of filters. They give the possibility to attenuate the intensity of the FEL in a discrete way according to the absorption edge of the differrent materials. The filters are partucularly useful when working with two wavelengths because they allow to selectively block one wavelength.

- The auto-correlater/delay-creator[40] (AC/DC) is an ad hoc optical device installed along PADReS. The AC/DC system splits the incoming FEL photon beam into two exact half-spots using a grazing incidence flat mirror (M1 in Fig. 1.10a). These spots then travel along two different optical paths, with the first path having a fixed length (blue line in Fig. 1.10a) and the second path having a variable length (red line in Fig. 1.10a) that can be adjusted by moving two grazing incidence mirrors mounted on mechanical rails (M6 and M7 in Fig. 1.10a). By doing so, a tunable temporal delay that ranges from -1 to +25 ps can be introduced between the two EUV/SXR pulses, enabling time-resolved experiments with

[6]The refractive index of the gaseous medium is different with respect to that of the vacuum, inducing a small chirp in the pulse.

two FEL pulses. The time resolution of the device is limited by mechanical factors, *i.e.* the mechanical resolution of the longitudinal actuators of M6/M7 is 10 microns, and it amounts to $\sim$ 360 as. AC/DC also enables polychromatic time-resolved FEL-FEL experiments with non-degenerate pump and probe pulses, which are tuned to different wavelengths. This is made possible by the double cascade HGHG scheme of FEL2, which generates two FEL pulses with different colors, and the use of selective solid-state filters inside the AC/DC. As a result, two delayed FEL pulses with different colors can be delivered to the experimental end-station to perform multidimensional spectroscopy studies.

1.6 The EIS beamlines at FERMI: TIMEX and TIMER

1.6.1 Introduction to the experimental techniques

The present section is inspired by textbooks and papers on non-linear optics (Ref. [41–43]).

Non-linear optics describes the interaction of an intense oscillating electromagnetic field with matter. At the root of the formalism used to describe such interactions lies the expansion of the polarisation $\mathbf{P}$ in terms of the electric field $\mathbf{E}$[7]:

$$\mathbf{P} = \epsilon_0 \Big[\chi^{(1)}\mathbf{E} + \chi^{(2)}\mathbf{EE} + \chi^{(3)}\mathbf{EEE} + ... \Big] \tag{1.32}$$

where the $\chi^{(i)}$s are the i-th order magnetic susceptibilities, tensors of rank i+1 that models the response of the material to the incoming electric field.

In linear optics, only the first term of the right side of eq. 1.32 is considered, so the response of the material to the incoming field in terms of polarization is linearly dependent on the intensity of the field ($\mathbf{P} \propto \mathbf{E}$). When the intensity of radiation is higher, the polarization can no longer be considered a linear function of the electric field because higher order terms become significant and cannot be neglected. Optical nonlinearities can be generated by different phenomena, such as motion of bound electrons, field-induced vibrations or orientational motions, optically-induced acoustic waves and thermal effects. A simple phenomenological interpretation of nonlinearities can be given based on the anharmonic oscillator model, where the motion of the electrons driven by the field are described with the analogy of a spring, whose force constant represents the force that binds the electrons to the nucleus. Within this model, the nonlinearities appear as a variation of the spring constant when the spring is stretched or compressed significantly, *i.e.* when the electron-nucleus is varied by a relevant amount [41]. Limiting to the simplest case of two fields with different frequencies (the second order), several processes can take place, *e.g.* second harmonic generation, sum and difference frequency generation and optical rectification.

The work presented in this thesis deals with time-resolved processes, so thoroughly presenting non-linear optical effects goes beyond the scope of this section. I will provide an introduction to the techniques employed in my PhD project: pump-probe and Transient Grating (TG)

1.6.2 Pump-probe spectroscopy

Pump-probe is an approach that allows to perform time-resolved investigations of ultrafast phenomena, harnessing the interplay between two pulses separated by a precise delay. The first pulse, *i.e.* the pump, is intense and it drives the investigated system towards non-equilibrium conditions, a transient state, which relaxes within a certain time span. The evolution of the state of the system

[7] Both the polarisation and the electric field are vector quantities, hence the susceptibilities are tensors.

is monitored with the second pulse, *i.e.* the probe, which is much less intense and ideally does not significantly perturb the system. The probe interrogates the state of the system at given delays and at the end of the experiment a time dependence of a specific osservable (O) accessed by the probe can be traced:

$$O(t) \rightarrow O(t_0) + \Delta O(t - t_0) \tag{1.33}$$

where $O(t)$ is the value of the osservable measured at the time t, $O(t_0)$ is the value of the osservable before the action of the pump pulse, and the last term can be interpreted as the variation induced by the pump. Several different types of properties may be monitored by the probe pulse to access different information:

- Transmission measurements: The trend of the transmitted probe beam intensity is traced as a function of the pump-probe delay. The time-resolved absorption of the probe beam is usually emploied to unravel the relaxation dynamics of a photoexcited state generated by the pump pulse [44].

- Fluorescence yield: Used to monitor the occupation of a particular state, often analyzed with time-resolved fluorescence intensity through nonlinear interactions like sum frequency generation gated by a short probe pulse[45].

- Refractive index changes: Detection methods include interferometric methods or observing changes in the optical spectrum due to time-varying phase [46]. Changes may also affect the spatial profile, inducing focusing or deflection of a probe beam [47]. In the case of noncollinear pump-probe geometries (*e.g.* TG, presented in the next section), the noncollinear pair of pump pulse induces a spatial modulation of the refractive index which can be monitored by the diffraction of the probe beam [43]

- Dichroism and birefringence: Indicate anisotropic absorption and refractive index, respectively, due to polarization changes induced by a pump pulse. Time-resolved measurements offer insights into reorientation dynamics. However, a control of the polarization of the probe beam is required [48].

- Coherent vibrations: Detected through third-order nonlinear polarization responses related to molecular or lattice vibrations. Output fields may show frequency-shifted [49] or time-varying refractive index changes [50](see four wave mixing presented inthe next section).

- Structural information: Various methods explore atomic-level order, like surface second-harmonic generation [51], which detects the transition from ordered to disordered structures, or diffraction patterns from laser-generated X-ray or electron pulses to measure changes in lattice constant [52].

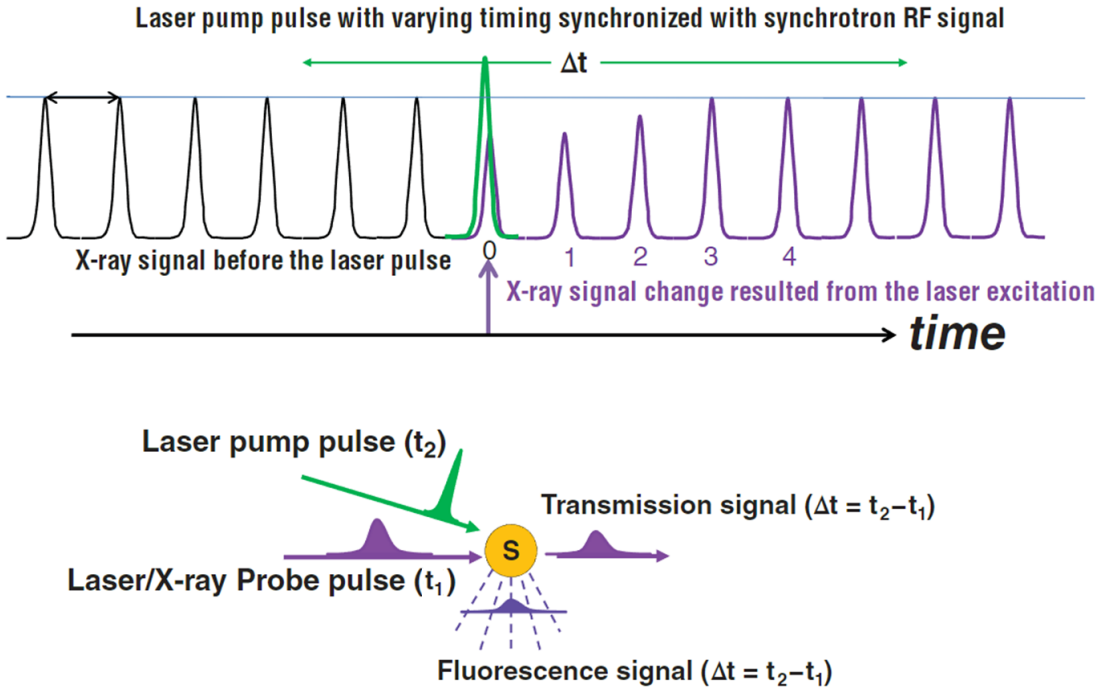

Figure 1.11: (Top panel) Illustration of the ratio behind an optical pump/X-rays probe experiment. Before the arrival of the pump pulse, the absorption of the x-Rays is consistent, while after the perturbation operated by the pump pulse, the absorption of X-Rays is subjected to time-dependent variations, in which the information about electronic and structural dynamics are encoded. (Bottom panel) Scheme of an an optical pump/X-rays probe experiment. Image adapted from [53].

The development of fs laser systems had opened the possibility of investigating with an unprecedented time resolution ultrashort phenomena of paramount importance in several field, such as the bonding dynamics during a chemical process [54]. A short pulse duration allows to deposit a high energy density on the target, hence the pump-probe approach can be employed to study the dynamics of materials driven to short-lived conditions of extreme temperature and pressure by an intense and short pump pulse. The advent of high harmonic generation and FELs has made available ultrashort pulses in the wavelength range of EUV and Soft X-Rays, combining for the first time a sub-picosecond time resolution with chemical selectivity associated to core-hole transitions. In the specific case of the main project of this thesis, an optical pump-EUV probe setup has been employed, with a time resolution limited by the cross-correlation between the pump and the probe pulses. One interesting aspect of the transient EUV/X-ray approach consist in the fact that the valence-excited states generated by the optical pulse are considerably longer lived, *e.g.* $10^{-13} - 10^{-6}$ with respect to the core-hole excitations produced by EUV/X-Ray photons, *e.g.* few femtoseconds or less [53]. The time-resolved approach applied to X-ray absorption spectroscopy of a photoexcited system, which allows for the determination of the electronic structure and of the local geometry in the surroundings of an atom, makes the technique of EUV/X-Rays transient absorption a unique tool for resolving both electronic and structural dynamics and their interplay [55].

1.6.3 Transient grating

Transient grating is a third-order non-linear optical process.

In materials with inversion symmetry the even-order susceptibilities are zero tensors for symmetry reasons, while odd-order susceptibilities have non-zero elements regardless of whether or not the inversion symmetry is present. Therefore, third-order non-linear processes, $\chi^{(3)}\mathbf{EEE}$, are the lowest order non-linear phenomena which have non-zero cross-section in all materials. A third-order process requires the interaction of three electromagnetic fields with the material, which in response generates a fourth field, *i.e.* the signal. These phenomena are described with the term four wave mixing (FWM). The sketch of a generic FWM experiment is shown in Fig. 1.12a. Each incident photon beam has its momentum and frequency, respectively k_i and ω_i, its associated polarization unit vector, $\widehat{p}_i$ and a relative arrival time with respect to the other beams, $\Delta t_{i,j}$, with i,j = 1,2,3. The resulting signal beam will have its own k_4, ω_4, $\widehat{p}_4$ depending on the combination of k_i, ω_i, $\widehat{p}_i$. Different FWM schemes will give rise to different phenomena, *e.g.* 3^{rd} harmonic generation, anti-stokes Raman scattering, multidimensional spectroscopy, TG etc. TG is a non-collinear pump-probe where two beams with identical wavelength (λ_{pump}) are spatially and temporally overlapped on the sample with a defined crossing angle (2θ); hence the associated wavevectors (k_1 and k_2) would have the same magnitude but a different orientation. In the scenario of a sample with an ideally flat surface perpendicularly disposed with respect to the bisector of the excitation crossing angle 2θ, the sinusoidally modulated TG spatial excitation would be characterized by a periodicity $\mathrm{L_{TG}}$:

$$\mathrm{L_{TG}} = \frac{\lambda_{\mathrm{pump}}}{2sin\theta} \tag{1.34}$$

The periodicity depends only on λ_{pump} and 2θ and the emerging wavevector associated with the TG excitation (k_{exc}) is oriented parallel to the sample surface, in the plane defiined by the two interfering excitation pulses, as illustrated in Fig. 1.12b:

$$k_{\mathrm{exc}} = \quad \pm \quad k_{\mathrm{TG}} \qquad\qquad with \qquad\qquad k_{\mathrm{TG}} = \frac{2\pi}{\mathrm{L_{TG}}} \tag{1.35}$$

The modulation of the intensity of the electromagnetic field arising from the interference of the pump beams induces a transient sinusoidal modulation of the complex refractive index of the material along the x axis[8] [56, 57]:

$$n(\lambda_{\mathrm{probe}}; x, \Delta t) = n(\lambda_{\mathrm{probe}}) + \Delta n(\lambda_{\mathrm{probe}}; \Delta t) \cdot cos\left(\frac{2\pi x}{\mathrm{L_{TG}}}\right) \tag{1.36}$$

Where the variation of refractive index is assumed to be linearly dependent with respect to the intensity of the interference pattern and the excitation is considered to be uniform along the z direction (sample thickness). The refractive index modulation thus generates an actual grating, where excited and unperturbed fringes alternate. Provided that the term $\Delta n(\lambda_{\mathrm{probe}}; \Delta t)$ from eq. 1.36 is non-zero, the spatial excitation acts as a diffraction grating for a third pulse of wavelength λ_{probe} and wavevector $\mathrm{k_{probe}}$, whose time of arrival can be controlled in order to probe the dynamic behaviour of the aforementioned non-linear excitation. The interaction of the probe beam with the transient grating generated by the pump beams produces an output which is itself a beam: the signal. The associated wavevector $\mathrm{k_{sig}}$ is given by the vector sum of the input pulses:

[8] The orientation of the spatial coordinates is illustrated on the top right corner of Fig. 1.12b.

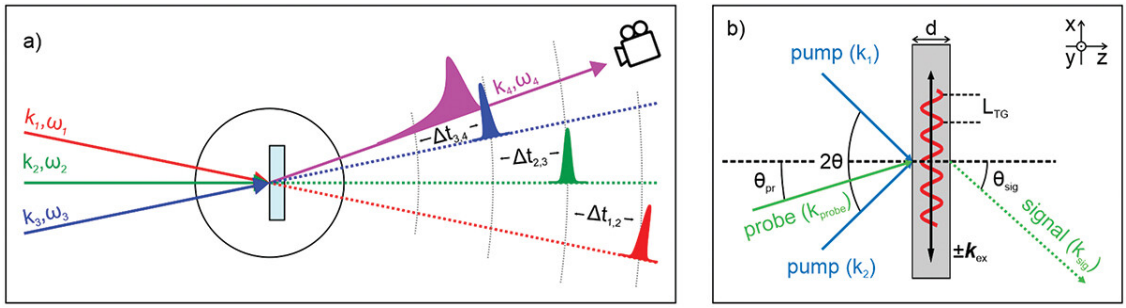

Figure 1.12: (a) Sketch of a four-wave mixing (FWM) experiment. The red, green, and blue pulses represent the three incident beams interacting in the sample. The magenta pulse is the generated FWM signal beam. $\Delta t_{i,j,k}$ are the time delays between the four pulses. (b) Scheme of a transient grating (TG) experiment illustrating relevant parameters that are described in text. The reference frame is depicted in the top right corner. Image reproduced from [43].

$$\mathbf{k}_{\text{sig}} = \mathbf{k}_1 - \mathbf{k}_2 + \mathbf{k}_{\text{probe}} \tag{1.37}$$

The signal has the same wavelength as the probe beam, but a different orientation that result from eq. 1.37 and that for the first-order of diffraction can be calculated as follows:

$$\theta_{\text{sig}} = arcsin\left(\frac{\lambda_{\text{probe}}}{\text{L}_{\text{TG}}} - sin\theta_{\text{probe}}\right) \tag{1.38}$$

The diffraction arises from the phase differences and the variations in absorption that builds up for different portions of the probe beam while it is crossing the sample after the spatial excitation generated by the pump beams. The different regions of the sample traversed by the the probe beam are characterized by different values of the refractive index $n(\lambda_{\text{probe}}; x, \Delta t)$, which upon the TG excitation is modulated in space along the x direction. Eq. 1.36 presumes a uniform excitation along z, but such condition is not realistic for EUV TG. Indeed, EUV radiation is strongly absorbed by any material and it is characterized by absorption lengths L_{abs} that are comparable with the values of the L_{TG} generated by a EUV TG excitation ($\sim$ 10s $-$ 100s nm). Therefore, a more appropriate description of EUV TG excitation would include an additional term with respect to eq. 1.36, that accounts for the dependence in z and L_{abs} :

$$n(\lambda_{\text{probe}}; x, z, \Delta t) = n(\lambda_{\text{probe}}) + \Delta n(\lambda_{\text{probe}}; \Delta t) \cdot cos\left(\frac{2\pi x}{\text{L}_{\text{TG}}}\right) \cdot exp\left(\frac{-z}{\text{L}_{\text{abs}}}\right) \tag{1.39}$$

The experimental observable in a TG experiment like the one depicted in Fig. 1.12 (forward diffraction) is the intensity of the diffracted signal, which is determined by the diffraction efficiency η and depends on $\Delta n(\lambda_{\text{probe}}; \Delta t)$:

$$\eta(\Delta t) = \frac{\text{I}_{\text{sig}}(\Delta t)}{\text{I}_{\text{probe}}} = |\Delta n(\lambda_{\text{probe}}; \Delta t)|^2 \text{F}(\lambda_i, \theta_i, L_i, d)\xi(\sigma_i, \Delta t_{\text{pump}}) \tag{1.40}$$

where the factor $\xi(\sigma_i, \Delta t_{\text{pump}})$ accounts for the spatial overlap of the three beams and specific parameter of the experimental scheme, while $\text{F}(\lambda_i, \theta_i, L_i, d)$ is a factor that contains static optical properties of the sample together with effects of energy and momentum conservation in the diffraction process which determine the wavevector mismatch:

$$\Delta K_z = n(\lambda_{\text{probe}}) k_{\text{probe}} |cos\theta_{\text{sig}} - cos\theta_{\text{probe}}| \tag{1.41}$$

The effect of ΔK_Z in the EUV regime does not have a strong impact, allowing diffraction to happen even without the Bragg condition satisfied. Nevertheless, the exponential decrease of the signal intensity due to absorption imposes an optimal value of the sample thickness (d usually < 100 nm) for which the diffraction efficiency is maximized.

The excitation mechanisms in the optical regime vary significantly depending on the material being studied, whether it is a weakly absorbing dielectric, semiconductor, or metal. The mechanisms range from field-driven density modulations (electrostriction) to intensity-driven thermal and electronic population gratings. Additionally, optical photons are essentially not transmitted into metals because their frequency is typically lower than most plasma frequencies. This makes optically-excited transient grating studies of bulk metals barely feasible [58].

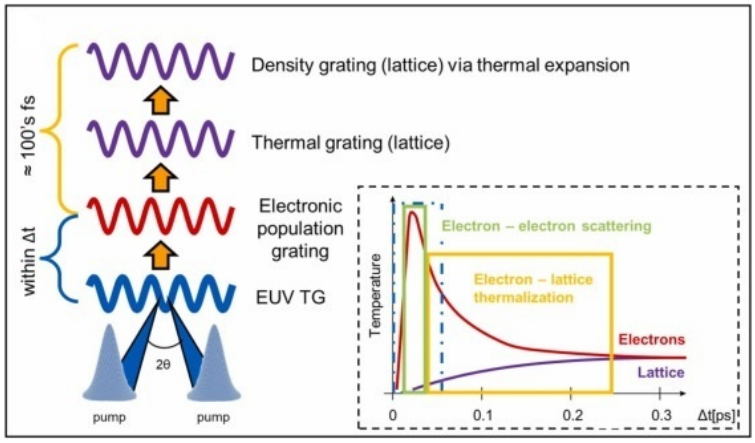

Figure 1.13: Main excitation mechanism for EUV transient grating: An electronic population grating in excited states is generated "instantaneously." Within hundreds of fs, hot electrons thermalize with the lattice according to the two-temperature model, as illustrated in the inset for temperature. The green and orange boxes indicate typical timescales for electron-electron scattering and electron-lattice equilibration, respectively. The blue dashed-dotted box depicts the typical excitation pulse duration of the FERMI FEL. Image reproduced from [58].

The situation is drastically different for EUV pumps, where photon energies in the 10s-100s eV range exceed plasma frequencies and electronic band gaps in all materials. This makes the distinctions between dielectrics, semiconductors and metals less relevant in the excitation process.

The same applies to the EUV probe frequency. Assuming it is also far from core resonances, the refractive index approximation commonly used for X-Rays can be applied: $\text{n} = 1 - \delta + i\beta$, where $\delta \text{and} \beta$ depend linearly on the total electron density [59].

In the EUV regime, the primary excitation mechanism is generating a photoexcited electron population with very high excess energy. This energy is exchanged with the surrounding electrons within tens of femtoseconds, typically without substantial diffusion on the length scale of L_{TG}. Since this process is much faster than the FEL pulse duration $\Delta \text{t}_{\text{FEL}} \sim 50$ fs used in EUV TG

experiments so far, it can be considered "instantaneous." This results in alternating stripes of hotter and colder electrons with the same periodicity of the TG (population grating). The modulated hot electron population thermalizes with the lattice through electron-phonon scattering, forming a thermal grating within hundreds of fs. Thermal expansion leads to an alternation between cold sample regions with increased density $\rho + \Delta\rho$ (unexcited stripes) and hot regions with decreased density $\rho - \Delta\rho$, where ρ is the unperturbed density. Similarly, at the surface, photoexcitation and subsequent thermal expansion produces periodic surface displacement, with a peaks and valleys structure emerging that correspond to the hot and cold areas. Bulk and surface expansion generates longitudinal and surface acoustic waves respectively, with wavevector k_{exc}. Once the thermal grating is formed, it is accompanied by a periodic modulation of not just the density, but of all the physical quantities coupled to the temperature, *e.g.* magnetization. Neglecting electronic diffusion[9] (which means considering the electron mean free path $\mathrm{L_e}$ over a time comparable to that of the electron-lattice thermal equilibration $\tau_{\text{e-l}}$ significantly smaller than the TG period $\mathrm{L_{TG}}$) the periodicity of the thermally-induced gratings matches that of the excitation light pattern, *i.e.* $\mathrm{L_{TG}}$. These gratings evolve over time following specific dynamics monitored by the probe pulse. At moderate EUV excitation intensities, the sample returns to its initial unperturbed state at longer times. If this recovery time is shorter than the interval between the pulses associated with two separate excitation events, given by the inverse of the pulsed EUV source repetition rate, the dynamics can be probed stroboscopically. EUV TG experiments so far have exploited low repetition rate FELs (< 1 kHz), but higher repetition rates up to the MHz level may be feasible. A graphical representation of the consideration presented in this paragraph is provided in Fig. 1.14.

[9]This condition simplifies the picture of the excitation process, but it is unrealistic. The electronic excitation generated with ~ 50 fs pulse cannot be considered impulsive, since the duration of the pulse is similar to or probably even longer than the hot electrons relaxation. Within the typical time of electron-lattice equilibration $\tau_{\text{e-l}}$, $\mathrm{L_e} \approx \mathrm{L_{TG}}$. Therefore, electronic diffusion is a process that cannot be neglected in the current state of EUV TG experiments, as it provokes a substantial reduction in the contrast of thermal gratings.

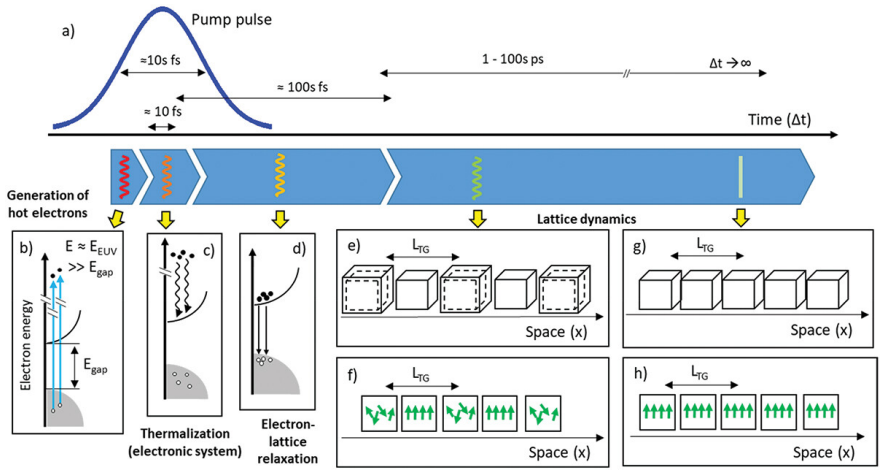

Figure 1.14: (a) Illustration of the EUV TG excitation process: the blue curve shows an EUV pulse with duration $\Delta t_{pump} \sim$ tens fs. EUV photons with energy EUV are predominantly absorbed by valence electrons (blue vertical lines in Panel b), initially generating hot electrons (black dots) and valence band holes (white dots). The valence and conduction bands are depicted as grey and white parabolic regions respectively. (c) On a $\sim$ 10 fs timescale, this hot electron population relaxes (black wavy downward arrows), generating electron-hole pairs across the valence band. (d) Relaxation due to carrier-phonon interactions on hundreds of fs timescale (black downward arrows). The EUV TG excitation thus produces an electronic population grating that relaxes by transferring energy to the lattice, periodically heating it (thermal grating). This induces periodic changes like density modulations (via thermal expansion; panel e) or magnetization gratings (panel f). For moderate EUV excitation, these gratings evolve to recover the initial unperturbed state. Core-level electronic transitions are ignored here. Image reproduced from [43].

1.6.4 TIMEX

The EIS TIMEX beamline is conceived to perform time-resolved studies of matter under extreme and metastable conditions with a sub-picosecond resolution [60, 61]. The design of the beamline and its dedicated beam transport is as simple as possible (see Fig. 1.15 a) in order to minimize FEL intensity losses whilst allowing for the possibility to focus the FEL radiation on the sample with a spotsize of just a few μm^2 [62]. This construction choice permits to concentrate the high FEL photon flux ($\sim 10^{13}$ photons per pulse) onto a small portion of the sample, reaching fluences up to 10^2 Jcm^{-2} [63]. The SLU (see section 1.5.2 on pag. 14) is the external optical coherent light source available at TIMEX for pump-probe experiments and it can be employed at its fundamental wavelength (784 nm) or at the second (392 nm) or third (261 nm) harmonic. The combination of such light sources opens different options for performing pump-probe experiments using the SLU as the pump and the FEL as the probe or viceversa. In both the cases the jitter will be of the order of just few femtoseconds. The core of the beamline is the 5-axis motorized sample-holder, that gives the possibility of performing raster scan single-shot pump-probe, which is ideal for destructive measurements and irreversible processes, as well as conventional pump-probe, working at 10 or 50 Hz, the operating repetition rates of the FERMI FEL.

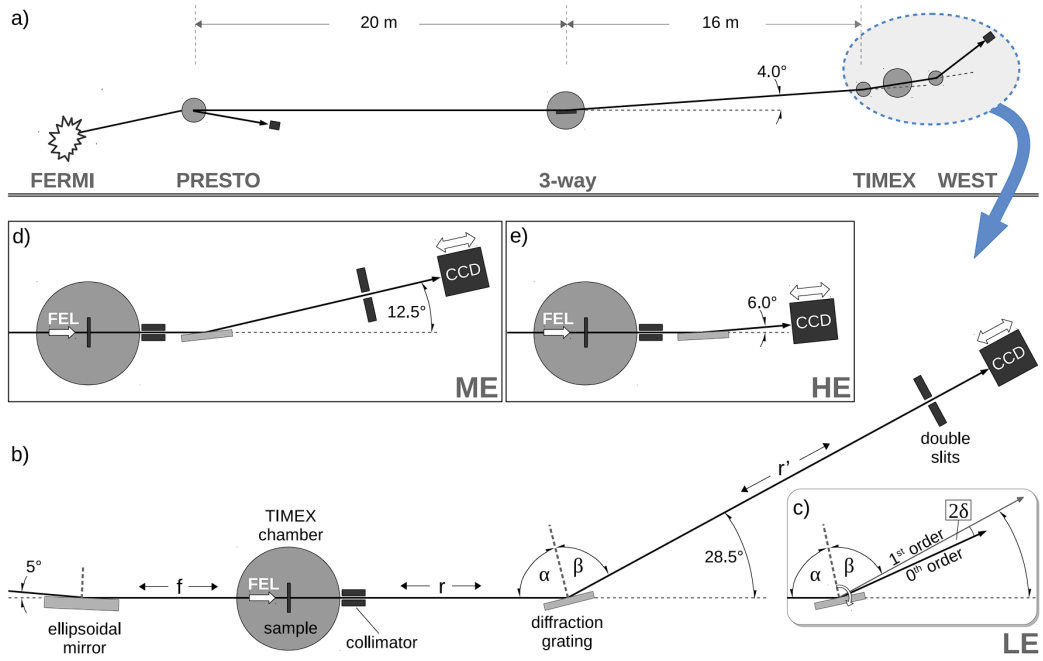

Figure 1.15: (a) Sketch of the beam transport to TIMEX and geometry of the beamline with the position of the two spectrometers PRESTO and WEST. (b) Detail of the geometry of the beamline which include the orientation of the ellipsoidal mirror, the position of the sample, the orientation of the diffraction grating and the position of the CCD in the low energy configuration (LE). (c) Angular relationship between the 0^{th} and the 1^{st} order of diffraction: the deviation angle $2\theta = \alpha + \beta$ is independent on the FEL wavelength while the scan angle $2\delta = \alpha - \beta$ increase with increasing FEL wavelength going from the 0^{th} to the 1^{st} diffraction order. Geomtetry of the (d) medium emergy (ME) configuration and of the (e) high energy (HE) configuration. The image is reproduced from [64]

TIMEX is an instrument devoted to the study of the following topics:

- matter under extreme conditions and warm dense matter: time-resolved XAS is employed to investigate transient conditions of high temperature and high pressure driven by isochoric heating induced by an intense and ultrashort laser pulse [65, 66];

- ultrafast carriers dynamics in photocatalysts: dynamics of photoinduced charge transfer probed with chemical sensitivity [67];

- visualization of molecular motion: pump-probe technique that use impulsive stimulated Raman scattering as the pump and EUV ultrashort pulses from the FEL as the probe to visualize molecular motion in real time with element- and enantio-specificity [68];

- EUV non-linear optical effects: exploitation of the high photon flux delivered by the FERMI FEL in the EUV range to observe non-linear spectral features, *e.g.* self-phase modulation [69], second harmonic generation [70], saturable absorption [71].

Furthermore, the robust pump-probe setup with sub-picosecond time resolution provided by the combo SLU-FEL, makes the beamline a suitable tool as well for the study of chemical reaction dynamics with elemental selectivity.

The standard samples at TIMEX are large-area free-standing thin films, which makes it possible to work in transmission with EUV radiation and provide sufficient amount of specimen for rastering. Currently, there are ongoing developments for two setups: a submicrometric liquid jet setup, which would enable working in the liquid state, and a high-pressure gas capillary designed specifically for studying non-linear effects in gas phase. Moreover, the possibility of exploiting the AC/DC device (see section 1.5.3) combined with the capability of FERMI of producing two FEL colors is being explored to perform EUV pump-EUv probe experiments, although the setup is not yet robust and consolidated.

As shown in Fig. 1.15, the first portion of the dedicated TIMEX beam transport is the plane mirror inside the 3-way switching chamber, that directs the FEL towards TIMEX. Moving 15 meters downstream along the transport, is located the ellipsoidal mirror, the key focusing element of TIMEX, which precedes the experimental chamber by 1.4 m. The ellipsoidal mirror is an EUV focusing optics that allows to focus the FEL beam on the sample with a gaussian-like spotsize of a few microns FWHM, which is crucial for maximizing the number of photons per surface unit and hence the energy density deposited on the sample. Furthermore, whenever the FEL pulses impinge on it, the ellipsoidal mirror produces a current. This makes the mirror eligible to serve as an on-line shot-to-shot diagnostic tool, *i.e.* I0 monitor, for obtaining an additional measure of the FEL intensity right before the sample. The experimental chamber is cylindrical in shape with a diameter of 500 mm and the standard working conditions inside it require a pressure of $\sim 10^{-6}/10^{-7}$ mbar, reached through a pumping system composed by a scroll pump and a turbo pump. A broad view of the sample holder inside the chamber is obtained with two GigaEthernet cameras from Axis Communications, while a telemicroscope from Questar provide a close view of the region where the pump-probe measurement is performed, allowing for inspection of the local sample quality and to monitor eventual radiation damages as well as the focus of the beams on the sample shot by shot during the acquisition of the raster scan. The objective of the telemicroscope is placed at 350 mm from the axis of the chamber at an angle of 20° with respect to the axis of the FEL beam. The resolution of the telemiscrope is of 10 µm with a focal depth of fews tens of µm and a lateral field o view of 600 µm. It is equipped with three motors for moving it along its axis (zooming) and tilting it vertically and horizontally. In combination with a YAG screen, it gives the possibility to determine the FEL focal plane and to visually estimate the FEL spotsize by examining the fluorescence. The telemicroscope enables also to check the spatial overlap between the FEL and the SLU by using a frozen YAG screen (the rough surface maximizes the scattering of the optical laser). The beamline is equipped with several possibilities for detection:

Photodiodes Solid state semiconductor devices (Si p-n junction photodiodes from IRD Inc) that detect EUV photons by generating charge separation that is transformed into a current. They cover the whole spectral range of interest at FERMI and they have a large dynamic range, which could be further adjusted by applying a reverse bias (high photon flux end) or by using an amplifier (low photon flux end). The beamline is equipped with a moving stage on a circular rail that allows to position these devices at the desired angle with respect to the sample holder.

Multi channel plates (MCPs) these devices are sensitive to EUV ionizing radiation or secondary ions generated by the FEL ionizing radiation. The sensitivity of the MCPs is extremely high, they can detect low photon intensities because the primary electrons generated by the detected particles (photons or ions) are amplified by a cascade process. MCPs are also placed along the circular rail and hence they can be employed both as detectors in transmission or in reflection geometries and off-beam as non-invasive beam diagnostics in the experimental chamber.

WEST the wide energy range spectrometer at TIMEX [65] is located downstream with respect to the experimental chamber and it is composed of a diffraction gratind and a CCD camera. The diffraction grating (provided by the Helmholtz Zentrum Berlin and kept at a pressure similar to that of the experimental chamber by a scroll pump and a turbo pump) disperses different wavelengths directly onto the the sensor of the CCD camera (Oxford Instruments, Andor iKon-M SO equipped with an uncoated back-illuminated 1024 × 1024 sensor with a pixel size of 13 µm, thermo-electric cooling). The camera is normal to the FEL beam and it is positioned on a longitudinal translator for optimizing the distance between the CCD and the grating. There is no entrance slit before the spectrometer, a strategic construction choice for the detector of a beamline designed to perform experiments with high FEL fluences, that would provoke radiation damage to the slits. The few µm FEL focal spot produced by the ellipsoidal mirror of TIMEX maximizes both the photon flux at the grating and the resolving power, validating the design of the spectrometer. WEST is equipped with a filter wheel at the exit of the experimental chamber, between the sample holder and the diffraction grating, which provide some options for attenuating the incoming FEL radiation with several solid-state filters when needed, in order to avoid saturation or damaging of the camera. WEST features three different fixed geometries (see Fig. 1.15), that were determined by balancing the energy resolution and efficiency: low energy (LE), medium energy (ME) and high energy (HE). As their names suggest, the schemes of the different configurations are optimized for the spectrometer to operate in the best conditions over the different spectral regions spanned by the emission of FERMI.

1.6.5 TIMER

The possibility of investigating elastic and thermal properties in nanostructured material, thin films and layered materials and in disordered systems, both static (*e.g.* glasses) and dynamic (*e.g.* liquids), as well as the chance for gaining a better understanding of phenomena whose knowledge is still fragmentary, *i.e.* the coupling of magnetic spin to electron and lattice degrees of freedom observed in magnetically ordered metals, where light can induce ultrafast demagnetization within 100 fs [72, 73], require accessing nanoscale properties with sub picosecond time resolution. Such temporal resolution is suitable to study dynamic magnetic processes, which are fundamental for technological applications like magnetic storage and spintronics and whose characteristic timescales are in the ps regime and beyond [74, 75]. Besides, magnetic dynamics are as well strongly dependent on the length scale, because they are affected by both long- and short-range magnetic interactions, *e.g.* such as spin orbit coupling, dipolar exchange and Dzyaloshinskii-Moriya interactions.

The need to fill this knowledge gap has called for an instrument that could access ranges of k values (momenta) in matter that are not accessible with other techniques, such as optical TG, inelastic UV scattering, inelastic neutron scattering, inelastic X-Ray scattering. The TIMER beamline has been designed to perform EUV TG exploiting the radiation produced by FERMI, granting the possibility of generating nanoscale TGs to access nanoscale properties with sub picosecond resolution.

Building a four wave mixing setup operating in the EUV presented technical challenges. For this sort of experimental schemes, it is necessary to split the incoming beam, generate a delay and then overlap the pulses on the sample. The critical aspect of working with EUV radiation is that it is strongly absorbed in all media (see Fig. 1.16a) and this determines two limitation: i) the need of performing all the experiments in vacuum ($\sim 10^{-6}$ mbar) and ii) the lack of efficient transmission optics. The solution employed at FERMI to overcome the issue of absorption is to use only reflective optics, which are achromatic and allow working over the full tunable range of

the FEL. However, the reflectivity of mirrors is very low at short wavelengths. This dictates the use of grazing incidence geometries in order to preserve the beam intensity as much as possible.

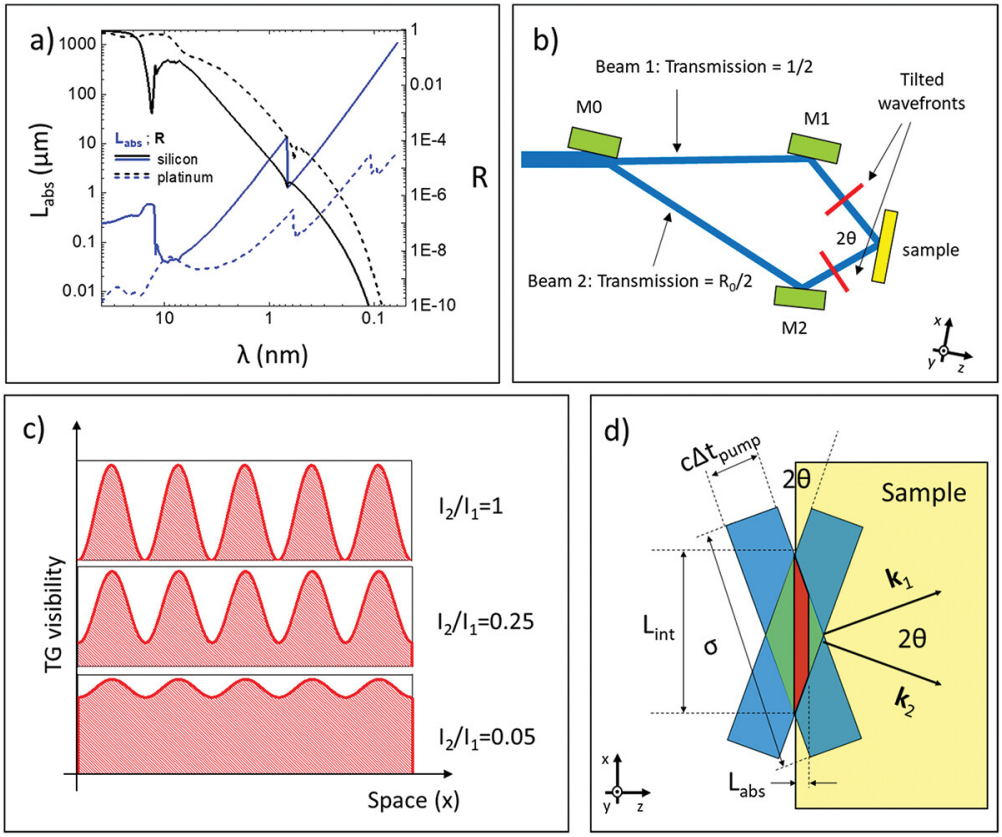

Figure 1.16: a) The graph displays the relationship between the absorption length (L_{abs}; shown in blue lines on the left vertical scale) and the reflectivity (R; indicated by red lines on the right vertical scale) for both silicon (represented by solid lines) and platinum (represented by dashed lines). The calculations for R were based on a grazing angle of 10 degrees and a surface roughness of 0.1 nm. b) This diagram illustrates the reflective split-recombination system utilized at the EUV TG instrument, currently available at FERMI. The components M1 through M3 are EUV mirrors. The ratio of the intensity between the two split beams after M0 is denoted as R_0, while the wavefront tilt corresponds to 2θ. c) Shown here is the TG intensity for three specific values of I_2/I_1. It is noteworthy that the TG visibility is significantly diminished at $I_2/I_1 = 0.05$. d) The figure demonstrates the wavefront tilt at the sample position resulting from two intersecting pulses with wavevectors k_2 and k_1. Its primary consequence is the reduction in the size of the interaction region (L_{int}) when using short values of Δt_{pump} and large values of 2θ. Panels a) and d) have been adapted from [58]. Panels b) and c) are taken from [43].

A fully reflective split and recombination scheme has been designed to fulfill the aforementioned requirements and a generic sketch to illustrate the principles behind this approach is reported in Fig. 1.16b. The plane mirror M0 geometrically divides the incoming beam into transmitted and reflected halves, which are recombined at the sample by mirrors M1 and M2. This scheme results in the two beam halves having different intensities. The half not reflected by M0, called pump 1, has intensity I_1=$I_0/2$, where I_0 is the upstream beam intensity. The reflected half, pump 2, has intensity I_2=$R_0I_0/2$, where R_0 is the reflectivity of M0. As shown in panel c of Fig. 1.16, an imbalance in the

pump intensities leads to decreased transient grating (TG) contrast and diffraction efficiency. The decrease becomes substantial ($\sim 50\%$) when the ratio $I_2/I_1=R_0$ is about 0.1. However, a reflectivity well above 10% mitigates the reduction in TG contrast and efficiency.

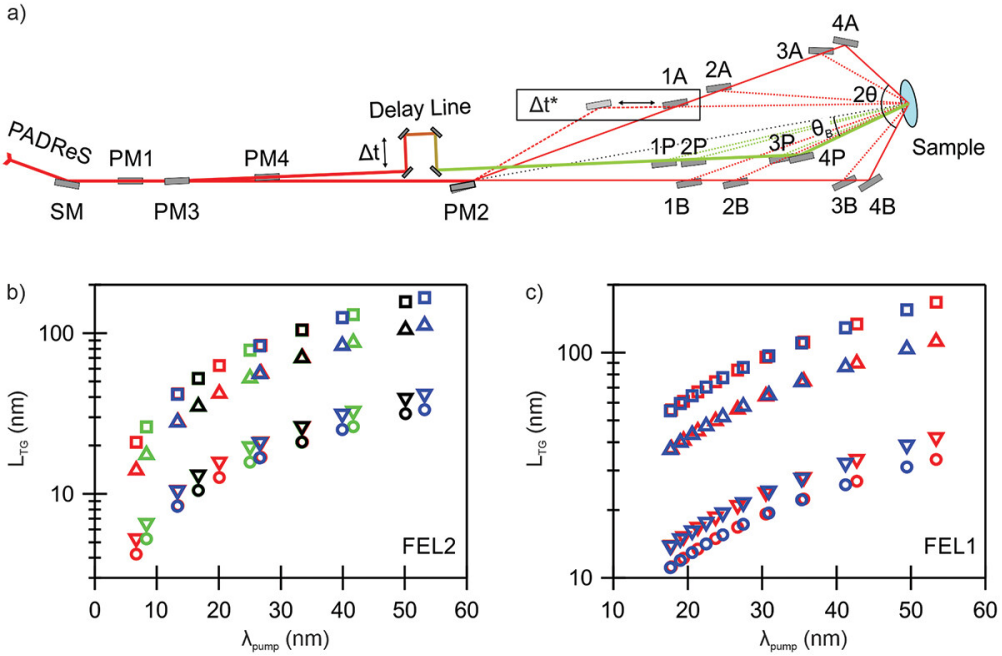

Figure 1.17: a) This schematic illustrates the beamline components. SM represents the switching mirror from the FERMI transport. PM1 is a plane mirror beam splitter that vertically divides the probe beam from the excitation beams. PM3 and PM4 serve as plane steering mirrors for the probe beam, while PM2 is a plane mirror beam splitter that horizontally separates the two excitation beams. Numbered from 1A to 4A are focusing toroidal mirrors for pump A, and from 1B to 4B are focusing toroidal mirrors for pump B. Similarly, from 1P to 4P are focusing toroidal mirrors for the probe. The diagram also indicates key angles and time delays: 2θ represents the excitation crossing angle, θ_B is the probe incidence angle, Δt^* indicate the relative delay between the two excitation beams, and Δt represents the relative delay between excitation and probe. b) The graph displays L_{TG} values as a function of λ_{pump} for FEL2. Different colors correspond to four possible probe wavelengths (6.7 nm in red, 8.34 nm in green, 13.3 nm in blue, and 16.7 nm in black). Shapes denote four crossing angles: 18.4° as squares, 27.6° as triangles, 79° as inverted triangles, and 105° as circles. c) The chart illustrates L_{TG} values as a function of λ_{pump} for FEL1. Various colors represent the two available probe wavelengths (17.8 nm in blue and 20.6 nm in red). Shapes represent the same four crossing angles: 18.4° as squares, 27.6° as triangles, 79° as inverted triangles, and 105° as circles. Image reproduced from [43].

In the EUV range, high reflectivity is readily achieved at small grazing angles, facilitating implementation of such setups. Another critical aspect emerges in the stage of recombination of the pump beams onto the sample: the wavefronts are tilted with respect to one another with an angle equal to 2θ (see Fig. 1.16d). The geometry of the recombination poses an intrinsic constraint on the size of the interaction region ($L_{int} = c\Delta t_{FEL}/\tan\theta$) and decreases the contrast of the fringes as the radial distance from the center of the interaction region grows. The larger the angle between the beams, the stronger these effect will be. Therefore, achieving the smallest possible TG periods is very challenging. Furthermore, the larger the tilt of the wavefronts with respect to the surface

of the sample, the broader the distribution of the arrival times of the individual pulses will be, contributing together with the pulse duration to limiting the time resolution ($\Delta t > \sigma_{pump} \cdot \tan\theta$).

The TIMER instrument was built for and has demonstrated the possibility of performing full EUV TG experiments, overcoming the constraints on the grating periodicity imposed by the wavelength of the optical probe. A schematic representation of the setup is reported in Fig. 1.17a. The PM1 mirror splits vertically the incident beam into two halves: one is reflected (it will become the probe beam) and the other transmitted. Afterward, the transmitted half is horizontally split by a second planar mirror (PM2), generating the two pump beams. The two pump beams are then recombined at the sample using sets of focusing toroidal mirrors (TM; labelled with numbers from 1 to 4 and with the letters A and B in Fig. 1.17a),[10] each housed in a separate vacuum chamber and selected by vertical translation. This design allows for four possible pump crossing angles: 2θ = 18.4°, 27.6°, 79° and 105°. Temporal overlap is controlled through translation of TM in branch A along the propagation direction to preserve the incidence angle, along with a corresponding pitch adjustment of PM2 and the TM itself. This arrangement permits the variation of the relative delay between the two pump pulses within a range of -3 to $+7$ ps $\pm$ 1 fs, albeit with limited mechanical reproducibility. The arrival time of the two pulses concerning a reference optical laser pulse can be determined with ≈10 fs precision by EUV-optical pump-probe measurements, using the low-jitter optical laser system available at all beamlines of the FERMI FEL [37, 38].

The vertically-split probe is redirected by two plane mirrors (PM3 and PM4) to be coplanar with the pump beams before reaching the delay line. The delay line precisely sets the arrival time of the probe relative to the pump in order to investigate dynamics lasting from a few femtoseconds to nanoseconds. To achieve this broad temporal range, the TIMER delay line utilizes four multilayer mirrors arranged at 45° angles of incidence. Such angles of incidence with EUV radiation come with a price to pay: i) the reflections causes a significant loss of the intensity, ii) multilayer mirrors optimized for a single wavelength need to be employed at the expense of the broad tunability of λ_{probe} provided by the FEL. The beamline can be equipped with four sets of mirrors for the delay line, that allow to work with 4 different λ_{probe} that could be interchanged by using encoded mechanical motors. The available sets of optimized multilayer mirrors at TIMER cover the following λ_{probe} values: 3.1, 6.7, 8.34, 13.3, 16.7, 17.8 and 20.6 nm. The condition on λ_{probe} dictates the whole geometry of the beamline, which is designed to satisfy Bragg conditions for $\lambda_{\text{pump}} = 3\lambda_{\text{probe}}$. This also determines the incidence angle of the probe: θ_{probe}= 3.05°, 4.56°, 12.24° and 15.38°. Similarly to the pump branch lines, the probe beam is focused at the sample with one of the four TM available for the probe.

On the sample the beams are overlapped and spots have a shape which differs from a circle, as it can be observed in Fig. 1.18.

The beamline is equipped with different options concerning the detectors:

EUV in-vacuum CCD cameras The standard choice for detection at TIMER is to use a CCD camera. The beamline is equipped with 2 fully in-vacuum CCD camera from Teledyne Princeton Instruments (PI-MTE) with scattering angle flexibility, which are tailored to work in low pressure vacuum chambers for diffraction experiments (direct detection of the diffracted beam). The cameras are equipped with an efficient liquid cooling system for reducing the noise arising from dark current, facilitating long exposures, and large format sensors (2048×2048 pixels, 15μm pixel size) with sensitivity in the range 10 eV - 30 keV.

[10] In the scheme of the beamline, the numbers 1 to 4 are assaciated with the four available transient grating geometries, while the letters A and B are used to denote the two different pump beams, respectively reflected and transmitted.

UV-VIS CCD camera An option for UV-VIS detection is provided by the Oxford Instruments Andor Newton CCD, equipped with thermo-electric cooling to minimize dark current noise and a 1024×256 pixel sensor (13.5μm pixel size) with fringe suppression technology.

CCD optical cameras The beamline has 2 compact CCD cameras from BASLER that can be used to perform faraday detection of the SLU in combination with a Wollaston polarimeter. These cameras are routinely used in the timing operation, where the the transient absorption of the SLU in a Ce doped Yttrium Aluminum garnet screen is monitored to locate in time the arrival of the FEL pulse.

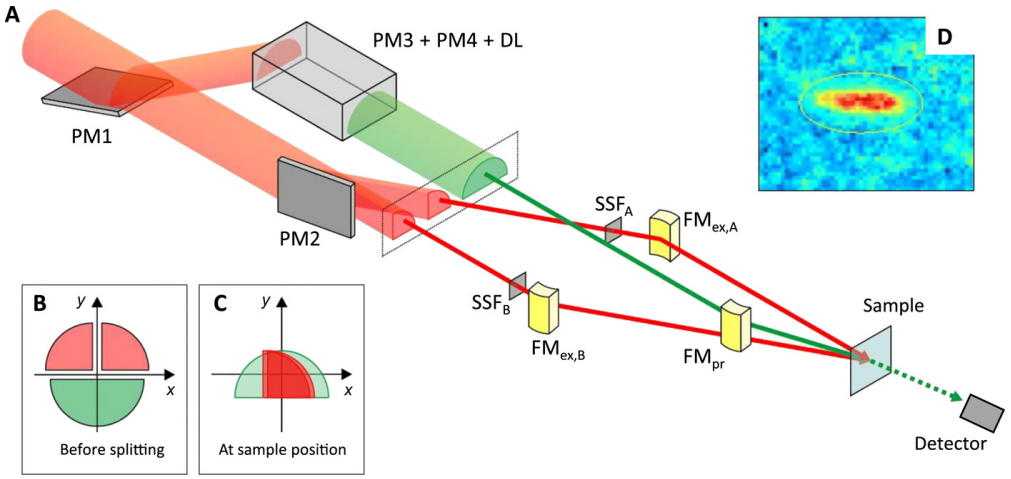

Figure 1.18: a) Schematic representation that depicts the standard configuration employed in the beamline, focusing on illustrating the beam splitting. The red beams denote the excitation pulses (λ_{pump}), while the green beam corresponds to the probe (λ_{probe}). Downstream, the green dashed line represents the signal beam. PM1 direct half of the beam into the probe's branch line. The probe branch line comprises two additional plane mirrors (PM3 and PM4) and a DL, constructed using four multilayer mirrors (see Fig. 1.17a) with high reflectivity at λ_{probe}. Consequently, the DL also serves as a λ_{probe} bandpass filter. Solid-state filters (SSFA and SSFB) eliminate radiation at λ_{probe} in the branch lines of the pump pulses. The three beams are ultimately focused at the sample at the desired angles by three TM (in the image, $\text{FM}_{\text{ex,A}}$ and $\text{FM}_{\text{ex,B}}$ for the two pump beams and FM_{pr} for the probe beam). Illustrated in (b) and (c) is the wavefront division beam-splitting approach.(d) Image of the signal beam as it appears on the detector. Image reproduced from [76].

Chapter 2

Time-Resolved Study of Thermite Reaction

2.1 Thermite reaction

The term "thermit" (from German) was coined by Goldschmidt [77] in 1908 to refer to exothermic processes in which metallic oxides were reduced with aluminum to produce aluminum oxide and other metals or alloys. During this sort of reaction, a significant amount of thermal energy is released, which is frequently sufficient to heat the intermediates/products phases over their melting temperatures. For instance, the well-known thermite mixture of aluminium and iron oxide give the following reaction:

$$2\mathrm{Al} + \mathrm{Fe_2O_3} \longrightarrow 2\mathrm{Fe} + \mathrm{Al_2O_3} \tag{2.1}$$

in such process, the temperature may reach more than 3000 K, which is above the melting point of both the materials. Generally, the term "thermite reaction" is used to indicate a much broader family of redox reactions, in which a metal reacts with a metallic or non-metallic oxide to produce a more stable oxide and the corresponding metal or non-metal of the reactant oxide. The characteristic feature of thermites is the high reaction enthalpy. A thermite reaction can often be thermally initiated locally by heating one of the components above its melting point. Thanks to its huge exothermicity, the reaction can then become self-sustaining when the heat released by the process is enough to initiate the reaction in the neighbouring reactants. Once the process becomes self-sustaining and begins to propagate, the reaction is said to be ignited. The time of ignition is defined as the time that the system needs in order for the energy released by the reaction to exceed the thermal energy externally provided to initiate the process.

Many thermite reactions yield a molten product consisting of a heavier metallic phase and a lighter oxide phase that can be separated by gravity. This fact in addition to the energetic efficiency of these reactions makes beneficial in a range of metallurgical applications. Indeed, the $\mathrm{Al/Fe_2O_3}$ mixture has been employed since the end of the 19^{th} century for the welding of the rail tracks. Thermite reactions are as well employed in processing of materials, as portable heat source or as high-temperature igniters. Self-sustaining reactions are exploited for environmental protection processes, ranging from the fixation and consolidation of high-level radioactive wastes, the treatment and recycling of a highly toxic solid waste from electrolytic zinc plants to the recycling of silicon sludge and aluminum dross produced by semiconductor industries and aluminum foundries, the degradation of chlorinated aromatics and the treatment of wastes containing asbestos and of by-products deriving from steel industries [78, 79]. The addition of inert additives to control the

propagation of the reaction have made thermite mixtures suitable for solid combustion studies, for applications as pyrotechnic materials, explosives and propellants [80–83]. Thermite reactions with Al and Mg have been proposed for *in situ* exploitation of resources on the Moon and on Mars, *e.g.* lunar regolith, for producing construction materials during future space missions [84–86]. Thermite reactions have found several application also in material science, such as synthesis of refractary ceramic and composite materials, magnatic granular films, iron aluminades and preparation of ceramics linings in metallic pipes.

Regardless of all the examples listed above, the use of thermite reaction for some types of application was hampered by an insufficient rate of energy release. Indeed, the kinetics of this class of solid-state reactions is governed by the mass-transport, which is the limiting factor for the reaction rate and, consequently, for the power generated by the reaction. Nanosizing[1] has proven to be an effective solution to the aforementioned issue and has significantly enhanced the potential of thermite reactions. Indeed, many of the desirable energetic properties of this family of redox processes can be considerably improved when at least one of the components of the reaction mixture has nanometric dimensions. Direct comparison between micron-sized particles and nano-sized particles has shown that nanoscaling leads to relevant benefits: i) drastic reduction of the ignition delay, ii) significant increase of the reactivity and iii)a higher rate of power release[87]. These distinctive features stem from the increase of the surface contact between the reactants and from the shorter average path that the species need to cover for meeting the reaction partner. Both these factors improve intermixing, that promotes homogeneity and mass transport, which accelerates the overall kinetic of the process. Nanosizing have developed significantly different properties compared to the analogue micron-sized mixtures, *i.e.* high exothermicity and fast energy release. These differences have led energetic nano composites of fuel and oxidizer to be categorized into a distinct class known as Metastable Interstitial Composites (MICs).

2.2 Motivation of the experiment

In this project, the redox reaction between hematite and aluminium has been investigated using ultrafast extreme ultraviolet (EUV) absorption spectroscopy. This process is an aluminothermic reaction that belongs to the family of chemical reactions commonly known as thermites. These reactions need a certain amount of energy to start, but once they are triggered, they are extremely exothermic and irreversible. The improvement in energetic performances obtained by nanoscaling, mentioned in the previous section, has revived and increased the interest in this class of reactions, which have been studied with different techniques, e.g. differential scanning calorimetry,[87] X-ray diffraction,[88, 89] Mössbauer spectroscopy,[88] mass spectrometry,[90] photoemission spectroscopy,[91] and with different ignition modes, e.g. wire heated via electrical discharge,[88] heating in a furnace[89] or nanosecond pulsed laser irradiation.[87, 90, 92]

All the aforementioned studies investigated the process in a microseconds to seconds timescale, looking at the reaction mechanisms from the standpoint of the slower steps of the whole process, i.e. the oxigen migration in the self-sustaining regime, up to the complete transformation of the reagents into the products. Moreover, the ignition mechanisms usually adopted have themselves a duration which is longer than nanoseconds/ hundreds of picoseconds, inherently limiting the time resolution. Conversely, our study focuses on the ultrafast dynamics, from the sub-picoseconcds to hundreds of

[1]Nanosizing refers to the process of reducing the size of particles or materials to the nanometer scale, typically ranging from 1 to 100 nanometers. This reduction in size often leads to significant changes in the properties and behaviors of the material. The aspects which result more relevant to thermite reaction are the reduction of the melting temperature and the significant increase of the surface to volume ratio.

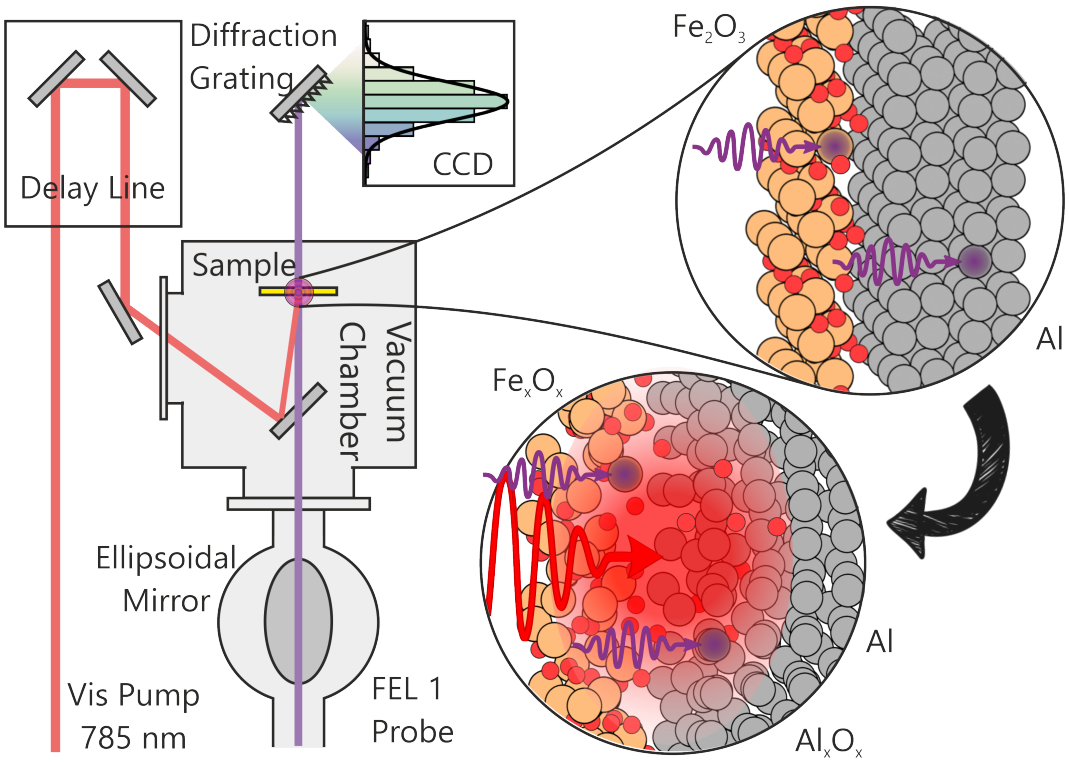

Figure 2.1: Illustration of the experimental setup. The red line mimics the path of the pump laser, which is generated in the FERMI femtosecond laser facility and transported to the experimental vacuum chamber. The pump beam is focused on the sample using a lens. The FEL radiation probes the Fe $M_{2,3}$ absorption edge and the Al $L_{2,3}$ absorption edge and it represented by the violet line. The FEL beam is delivered on the sample through the beam transport vacuum pipes and focused on the sample with an ellipsoidal mirror. The laser pump and the FEL arrive at the sample with a quasi-collinear geometry thanks to a motorized hollow mirror that reflects the laser while letting the FEL pass through the hole. The transmitted EUV radiation is detected with the WEST spectrometer, while the residual pump is filtered. The laser pump drives the sample out equilibrium, reaching high temperatures and triggering the redox process between α-Fe_2O_3 and Al.

picosends. To this end, we have employed an ultrashort laser pulse to drive the reaction system out of equilibrium and photothermally excite aluminium. Doing so the redox process is initiated and the dynamics are probed by EUV radiation at the Fe $M_{2,3}$ edge and at the Al $L_{2,3}$ edge through absorption spectroscopy (a graphical representation of the idea of the experiment is illustrated in Fig. 2.1). These edges are associated with shallow core levels which are atom-specific and sensitive to variations of both oxidation states and chemical environment, hence monitoring their behaviour is convenient to investigate a chemical reaction. Time-resolved X-ray absorption spectroscopy (XAS) at the Fe $M_{2,3}$ edge with table top high harmonic generation (HHG) has already been shown to be a powerful tool. Ultrafast dynamics were probed with sensitivity to the change of oxidation state in α-Fe_2O_3. Vura-Weiss et al. have demonstrates with this technique that the optical excitation (400 nm) in α-Fe_2O_3 has a ligand-to-metal charge transfer (LMCT) nature, *i.e.* upon excitation, en electron is transferred from the oxygen 2p orbital to the iron 3d orbital, changing the oxidation state from Fe^{3+} to Fe^{2+} [93]. In the work from Carneiro et al., tr-XAS at Fe $M_{2,3}$ edge is employed to prove that carrier mobility in α-Fe_2O_3 is limited by self-trapping of carriers in the form of a small polaron, whose formation and hopping probabilities are proven to depend on the optical excitation wavelength and whose appearance is associated to a specific spectroscopic feature of the Fe $M_{2,3}$ edge [94].

The study of chemical processes with time-resolved spectroscopy was pioneered in the work from Zewail [54], where the the I-C bond cleavage of ICN molecule was monitored upon excitation to the dissociative excited state. More recently, the development of FELs and tabletop HHG sources has paved the way for the progression of soft X-ray and EUV spectroscopic techniques, combining femtosecond time resolution and chemical selectivity. Such techniques have been successfully used to study intramolecular photoactivated processes. Attar et al. investigated a prototypical pericyclic photochemical reaction: the ring-opening of 1,3-cyclohexadiene. The light-activated process was initiated with UV photoexcitation and monitored at the carbon K edge with a soft X-ray HHG source [95]. Pathak et al. have employed time-resolved photoelectron spectroscopy with the EUV radiation produced by the FERMI FEL to trace the ultrafast ring opening of gas-phase thiophenone molecules following ultraviolet photoexcitation [96]. To the best of our knowledge, there is no study of bimolecular reactions by ultrafast spectroscopy using EUV/soft X-ray light. Here, we take the first steps towards chemically resolved monitoring of a chemical reaction between two reaction partners in the solid state. The aim of this work is to exploit the potential of tr-XAS to access the electron transfer between Al and α-Fe_2O_3 and follow the dynamics of the redox process with chemical selectivity.

2.3 Experiment

2.3.1 Results

Overview of the experimental results

Dynamics were measured for 7 photon energies across the Al $L_{2,3}$ edge and 6 photon energies across the the Fe $M_{2,3}$ edge in two different experiments. The energies that were selected for the measurements are highlighted in Fig. 2.2, respectively for a) Al $L_{2,3}$ edge and b) Fe $M_{2,3}$ edge.

The temporal sampling was selected to probe both the ultrafast dynamics near time zero (steps of 100 fs), and the slower lattice dynamics at larger delays (steps of 10 ps), with intermediate steps (1 ps) for the transitioning region. In Fig. 2.3, the pump-probe traces measured at several energies are plotted together for α-Fe_2O_3 (left panel) and Al (right panel). This provides a comprehensive picture of the measurement results across the two absorption edges and visualizes the dynamic

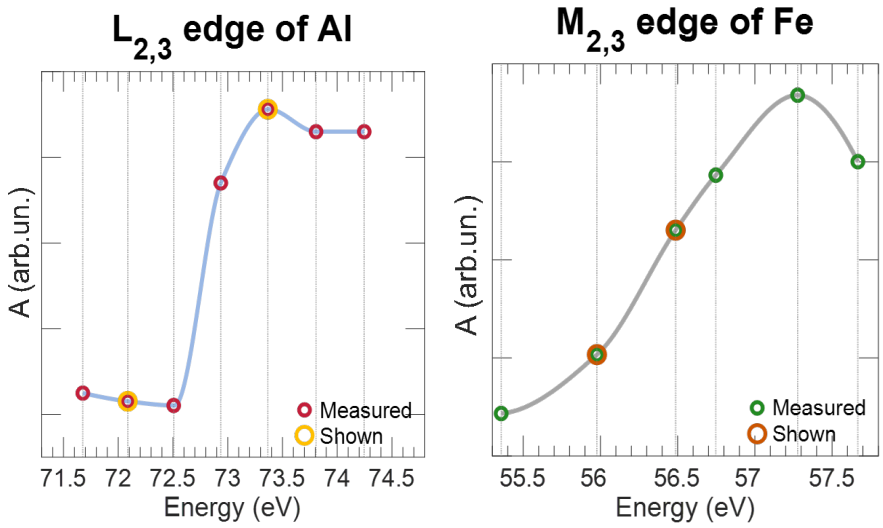

(a) (b)

Figure 2.2: Static absorption spectra of (a) $L_{2,3}$ of aluminium and (b) $M_{2,3}$ of iron in hematite. The photon energies which were investigated with the FERMI FEL are highlighted, and the photon energies whose dynamics are shown in the panels b and d have been highlighted with a different color. The blue line in panel a and the gray line in panel c are interpolated over the experimental points and are meant to serve as a guide for the eye.

trace trends. Specifically, the blue regions indicate increased absorbance at lower energies, while the red regions show decreased absorbance at higher energies. The panels below the TA maps show static and transient spectra, further illustrating the absorbance trends.

In both TA maps, a variation of the absorbance consistently occurs after few picoseconds, visible as the blue becoming weaker and the red more intense. This reflects the local density variation of the two materials caused by the ultrafast isochoric heating, which exerts a strong compressive pressure in the along beam direction that results in an expansion along the transversal directions. The net effect of such process is a reduction of the number of atoms probed by the FEL beam inside the spot.

Illustrative pump-probe traces are shown in Figs. 2.4a and 2.4b along with their fits. The fitting functions used are described in section (2.3.5). The complete set of fits is shown in appendix A. The time constants obtained from the fitting procedure are listed in table 2.1.

		Fast τ_1 (ps)	Slow τ_2 (ps)
Pre-edge	Al	1.18 ± 0.13	8.3 ± 1.1
	Fe	2.60 ± 0.08	42.0 ± 10.9
Post-edge	Al	1.54 ± 0.21	3.3 ± 0.3
	Fe	1.58 ± 0.16	40.0 ± 6.9

Table 2.1: Kinetic constants from the fits of the pump-probe traces for aluminium and hematite.

Transient absorption spectra have been fitted on the experimental data at some representative delays and are reported in Fig. 2.5. The functions employe for the fits are described in data processing section (2.3.5).

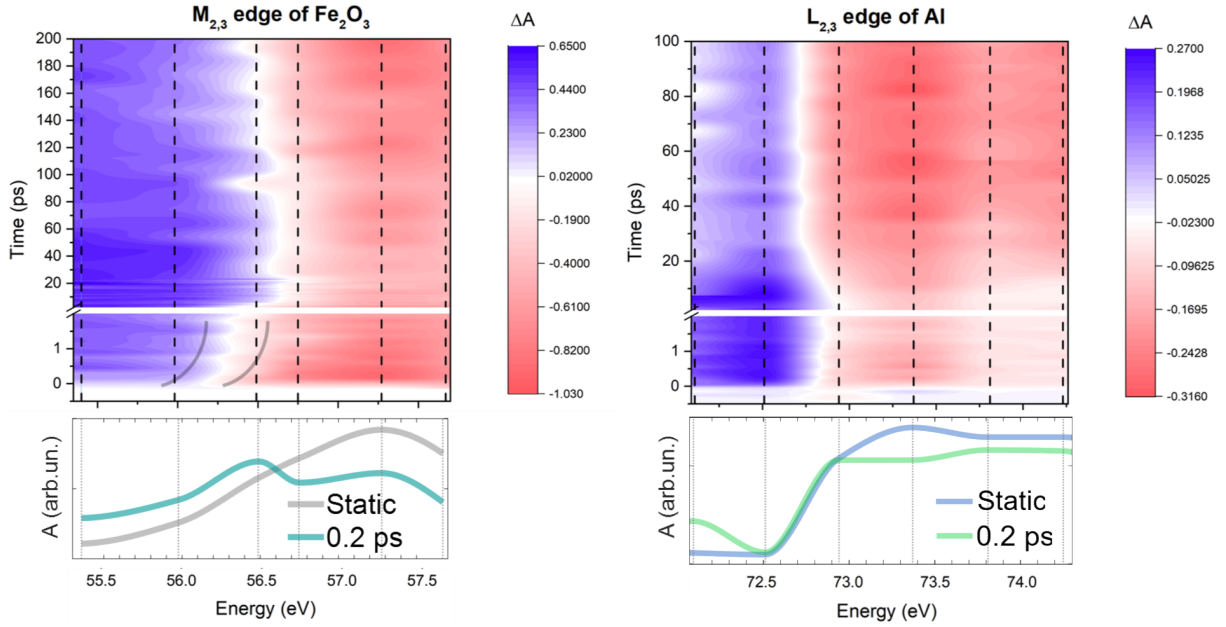

Figure 2.3: TA traces of the hematite/aluminium sample across the Fe $M_{2,3}$ (left panel) and Al $L_{2,3}$ (right panel) absorption edges. The dashed lines are the pump-probe dynamics measured in the experiment interpolated over a uniform time mesh in order to plot them together. The 2D-maps are obtained by interpolation of the time traces over the photon energies measured in the experiment and serves the purpose of providing an overall picture of the results of the dynamic behaviour of the absorption edges. The panels below the 2D-maps show respectively the static absorption spectra of Fe $M_{2,3}$ and Al $L_{2,3}$ and the transient absorption spectra at 0.2 ps.

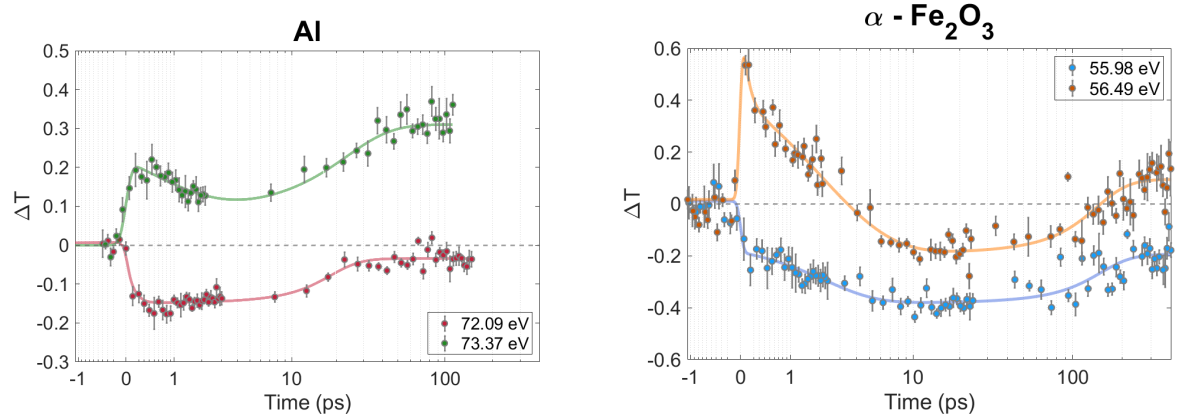

(a) (b)

Figure 2.4: Pump-probe dynamics are shown for two different energies (above an below the isosbetic point of the absorption edge) for both Al $L_{2,3}$ (left panel) and Fe $M_{2,3}$ (right panel).

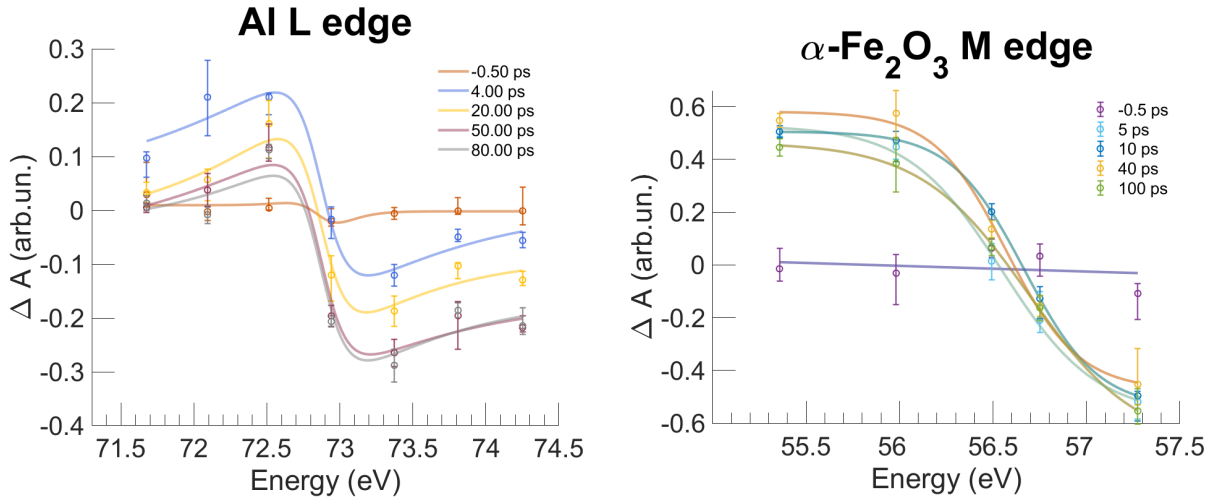

(a) (b)

Figure 2.5: Transient absorption spectra at some representative delays for Al $L_{2,3}$ edge (left panel) and Fe $M_{2,3}$ edge (right panel).

2.3.2 Discussion

Fits of the pump-probe dynamics

The time constants for the fast dynamic, τ_1, derived from the fits are a few picoseconds for both α-Fe_2O_3 and Al. For Al, the value of τ_1 is reasonable to describe the hot electron equilibration with the lattice via electron-phonon collisions. Al behave like an ideal free-electron gas and it could be described quite accurately by the two temperature model (TTM) [97, 98]. The electronic subsystem thermalization in Al is predicted to be 11 fs [97], so it is shorter than the SLU pulse duration, while the thermalization between the hot electrons and the lattice is predicted to occur within 2 ps [99]. In hematite, excited carriers interact with the lattice by scattering off electrons with optical phonons, *i.e* quantized vibrational modes of the crystal lattice, leading to small polaron formation and charge carrier localization [100]. A polaron refers to an electron or hole in a solid that distorts the surrounding lattice and becomes "self-trapped" by this distortion. This lattice distortion creates a potential well that localizes the carrier. Small polarons, specifically, have a spatial extent smaller than the lattice parameter. The self-trapping occurs because the carrier interacts strongly with optical phonons [101].

As it will be evidenced in the data processing section, the dynamic at 56.49 eV requiered a second exponemtial decay ($\tau_1^* = 0.1ps \pm 0.6$) to fit the data (see eq. 2.12). The presence of this additional term is justified by the fact that this specific photon energy is close to the spectral region where the feature associated to the process of small polaron formation is observed (namely, a blue shift of the invariant absorption point, which is highlighted in Fig. 2.3 and better described later in the text). The polaron is interpreted as an additional decay because its formation is associated to the disappearance of hot electrons from the conduction band. In Fig. 2.6 the calculations for the transient absorption of α-Fe_2O_3 predicted using the polaron model and the polaron+state filling model are reported. From the figure, it is reasonable to think that the dyanmics at 56.49 eV and 56.74 eV should be the most sensitive to the polaron formation process, since they are in the region where the ΔA is larger. The issue with the dynamic at 56.74 eV is that is not as clean as the one at 56.49 eV (The errorbars for the first ps of the pump-probe are very large and the ΔT values are

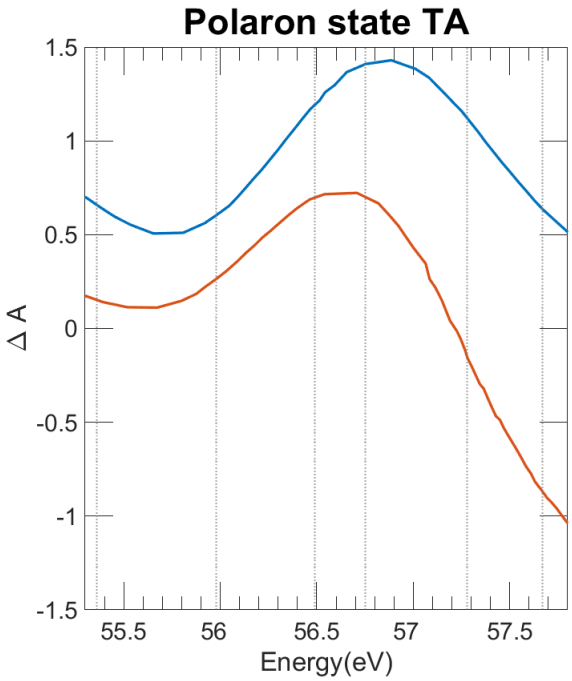

Figure 2.6: Calculations for the polaron transient absorption with the polaron (blue line) and the polaron+filling state model (orange line). The data were taken directly from Ref. [102] and adapted. The photon energies which were investigated in the experiment are represented by the dashed lines.

scattered), therefore the fit is not as realiable as the one at 56,49 eV.

The time constant for the slower dynamic, τ_2, is tens of picoseconds for aluminium and tens to hundreds of picoseconds for hematite. Several fs laser ablation studies have been performed on aluminium at different fluences [99, 103–105]. High fluences (> 0.05 J/cm^2) have demonstrated ultrafast isochoric heating in Al, which leads to collapse of the overheated material and generation of GPa-level compression pressures in the film's center. Under these conditions, the film expands within tens of picoseconds after laser pumping, forming voids and nanoparticles.

The τ_2 time constants reported in Table 2.1 and the uniform transmission increase at longer delays agree well with this ultrafast isochoric heating mechanism. For Al, the absolute transmission change could reflect an $\sim 8\%$ reduction of atoms in the probed volume. Although we did not find similar fs laser ablation studies on hematite, our similar pump-probe traces suggest an isochoric heating mechanism also occurs in hematite at high fluences, just with different kinetic constants. A similar estimation for Fe atoms in the probed volume gave an $\sim 5\%$ decrease. However, absorption cross-section changes likely also depend on other phenomena like phase transformations and refractive index changes. The significantly higher kinetic constants in the case of hematite can be explained in terms of the mass difference between Fe and Al.

A crucial aspect fot the investigation is understanding whether the requirements for starting the termite redox process were met during the experiment. Studies on the thermite reaction [88, 90, 91] have identified aluminum melting as a key step for initiating the redox reaction between aluminum and iron oxide. In simulations by Tang et al. [99], a 200 fs laser pulse with ~ 0.06 J/cm^2 fluence causes thermal melting via lattice collapse within 2 ps in a 100 nm aluminum film, raising the temperature at the laser-exposed surface to $\sim$3000 K. In our experiment, the ~ 0.9 J/cm^2 laser

fluence likely raised the lattice temperature at the hematite-facing side beyond 3000 K, satisfying the aluminum melting condition to trigger the redox process. Furthermore, the lattice collapse, layer expansion/disaggregation under compressive pressure, and nanoparticle formation appear to promote mixing and maximize contact area between the materials at the interface.

Fe $M_{2,3}$ absorption edge transient absorption

In the study by Carneiro *et al.* [94], it was demonstrated that a specific spectroscopic feature in the transient absorption (TA) spectrum is the fingerprint of small polaron formation. Specifically, the shift in the zero-crossing within the first hundreds of fs in the spectral region between 56 and 58 eV indicates polaron formation. Small polaron formation in α-Fe_2O_3 follows a two-step process:

(i) The first step is optical excitation, which has charge transfer character. This involves displacement of an electron from the O 2p orbitals to the Fe 3d orbitals, consequently varying the iron oxidation state from +3 to +2.

(ii) The second step is interaction of the carriers with optical phonons, causing local lattice distortion. This induces self-trapping.

Carneiro and collaborators proposed a kinetic model where polarons form through bimolecular recombination of hot electrons and optical phonons. Polarons appear within 100 fs, and their population continues growing for 2-3 ps as the hot electron and phonon populations are consumed.

Comparing our TA measurement at Fe $M_{2,3}$ edge with the study of Carneiro *et al.*, we have observed the same feature, regardless the fact that we employed a 785 nm pump, which is well below the α-Fe_2O_3 bandgap ($\simeq$ 560 nm), while they were using an optical pump above the bandgap of α-Fe_2O_3. The left panel of Fig. 2.3 shows a detail of the transient absorption spectrum of hematite (on aluminium) at the Fe $M_{2,3}$ edge in the first picoseconds of the pump-probe measurement. The shift of the zero crossing point[94] is highlighted by the gray lines. Such observation poses a question on the nature of the excitation mechanism. In the scenario of single photon absorption (SPA), the excitation would occur at 785 nm. On one side, the absorption cross-section would be very low, but on the other side, the pump fluence would be high enough to generate an observable excitation and the polaron formation would be more efficient, according to the findings of Carneiro *et al.* Conversely, in the scenario of a two photon absorption (TPA), the excitation would occur at 392.5 nm, a wavelength where the absorption cross-section is much higher than at 785nm.

This issue was addressed by Okazaki *et al.* [106], who studied the excitation mechanism of a α-Fe_2O_3 photoanode in contact with a gold nanorod using transient absorption (TA) spectroscopy. They demonstrated that two-photon absorption (TPA) needs to be considered to explain the dynamics of hematite TA spectra when using an 800 nm excitation wavelength. Moreover, good efficiencies for nonlinear optical processes have been observed in the NIR region at 1064 and 1340 nm [107], further indicating that TPA likely occurs in hematite at longer wavelengths compared to the visible bandgap. Since TPA in hematite was observed at 800 nm with a fluence of 1.0 mJ/cm^2, TPA is likely the dominant excitation mechanism in our experiment as well.

Comparison α-Fe_2O_3 on Al and α-Fe_2O_3 on Pary

In Fig. 2.7, transient soft-X-ray absorption spectra at the Fe $M_{2,3}$ edge are reported for the (a) α-Fe_2O_3/Al sample and (b) α-Fe_2O_3/Parylene sample. The spectra are fitted to the transient absorption values from the single wavelength pump-probe experiments across the Fe $M_{2,3}$ edge for two selected delays.

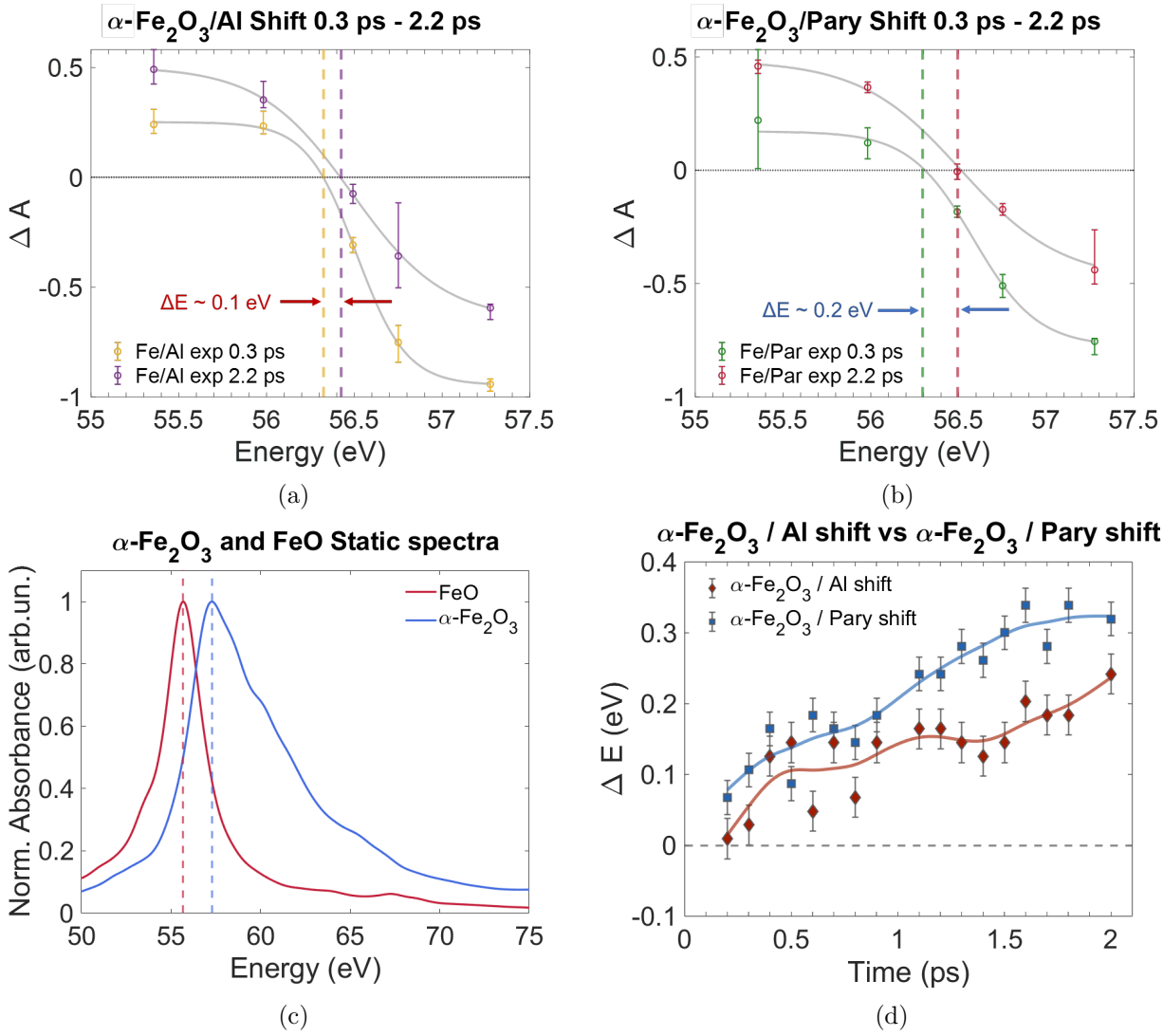

Figure 2.7: Spectra from the TA trace of the (a) α-Fe_2O_3/Al sample and of the (b) α-Fe_2O_3/parylene sample at the Fe $M_{2,3}$ absorption edge. Two delays were selected (0.3 and 2.2 ps) to show the shift of the zero-crossing. (c) Simulation of the static absorption spectra for the Fe $M_{2,3}$ edge for FeO and α-Fe_2O_3. (d) Evolution of the shift of the zero crossing point with respect to the crossing at t = 0.1 ps for the α-Fe_2O_3/Al sample (red) and for the α-Fe_2O_3/parylene sample (blue). The errors are calculated as the root means square of the residuals with respect to the fit of the two distributions.

The spectral behavior differences over time are highlighted in Fig. 2.7a and 2.7b using dashed vertical lines, which visualize the shift in the zero-crossing point with pump-probe delay.

Comparing our spectra of hematite deposited on Al and parylene, we observed a noticeable difference in the blue shift of the zero-crossing point. We quantified this shift to be ∼0.1 eV for α-Fe_2O_3 on Al and ∼0.2 eV for α-Fe_2O_3 on parylene from 0.3 ps to 2.2 ps. To confirm this observation, we computed the shift for several delays, taking 52.2 eV as the reference zero-crossing value at 0.1 ps. We monitored the shift behavior for both the α-Fe_2O_3/Al and α-Fe_2O_3/Pary samples. The trend observed when comparing Fig. 2.7a and 2.7b is consistent across several delays, as shown in Fig. 2.7d. The α-Fe_2O_3/Al sample exhibits a smaller blue shift. This smaller blue shift for the α-Fe_2O_3/Al sample could originate from charge injection from Al to α-Fe_2O_3. The electrons injected into α-Fe_2O_3 are also likely localized as small polarons, but the mechanism may differ since the overall charge balance of the material is altered. This interpretation is supported by the observation of α-Fe_2O_3 reduction by a metal in the aforementioned study by Okazaki *et al.* [106]. Furthermore, it is reasonable to think that this phenomenon would occur under the present experimental conditions, since we have demonstrated that we are fulfilling the requirements to initiate the thermite reaction, and reduction of hematite is reported as the first step of the process [88].

Additionally, to support our hypothesis, a red shift of the transient signal was predicted from calculations on hematite by Klein *et al.* [102] when including excited carriers in modeling the polaron state. Finally, a red shift of the Fe $M_{2,3}$ absorption edge is predicted when Fe transitions from the +3 to the +2 oxidation state. This can be observed in Figure 2.7c, which presents the results of the static absorption simulation for FeO and α-Fe_2O_3. Our findings support the notion that electron transfer occurs between aluminum and hematite upon excitation of the α-Fe_2O_3/Al sample using a high-power 785 nm pulse. We can exclude the occurance of highly non-linear electronic effects such as tunneling ionization caused by the pump pulse, as these effects become significant only at peak powers exceeding 10^{15} W/cm^2 [108]. In our experiment, the pump peak power was approximately 10^{13} W/cm^2, therefore multiphoton and avalanche ionization phenomena cannot be ruled out. Nevertheless, such effects would be the same for both hematite samples, whereas the observed red shift is dependent on the substrate. On longer time scales (tens to hundreds of picoseconds), we have not observed any increase in the Fe $M_{2,3}$ shift between the two samples, α-Fe_2O_3/Al and α-Fe_2O_3/Parylene. Therefore, we deduced that either i) the redox reaction is only partially occurring (reduction of α-Fe_2O_3 by Al) within the investigated time interval, or ii) the reaction may be localized near the interface, limited by mass transport. According to the study by Shimojo et al. [109], the breaking of Fe-O bonds and the subsequent formation of Al-O bonds at the interface would occur within a few picoseconds (< 5 ps). Hence, the latter interpretation (reaction occurring only near the interface) is plausible, and the absence of spectroscopic signatures may be attributed to insufficient contrast to detect a significant difference in the presence of aluminum.

Al $L_{2,3}$ absorption edge transient absorption

Regarding the Al $L_{2,3}$ absorption edge, no significant shift was observed in the first picoseconds. This could be attributed to the following reasons:

(i) The aluminum layer is much thicker than the α-Fe_2O_3 layer, so the electron transfer and the eventual formation of Al-O bonds (as proposed by Shimojo et al. [109]) at the interface only affect a small fraction of the Al atoms within the probed volume of the FEL beam. As a result, the effect is below the detectability threshold of the experimental setup.

(ii) Isochoric heating leads to hydrodynamic expansion, causing complete ablation of the sample within nanoseconds. On this time scale, species migrate and interdiffuse between the two materials to some extent due to the rapid temperature increase and resulting strain, leading to melting or disruption of the solids [99]. The expansion and transition to the gas phase result in a density drop within the sample volume on the tens of picoseconds timescale, thereby reducing the TA (transient absorption) signal.

(iii) The pressure in the experimental chamber was 10^{-6} mbar, which may have caused gaseous species to be removed from the reaction system, hampering the progress of the reaction.

(iv) The observed time window with the pump-probe is on the order of hundreds of picoseconds, which may not be sufficient to achieve a signal level high enough to detect the ongoing reaction.

2.3.3 Conclusions

In this study, we have successfully utilized tr-XAS to monitor the progression of a chemical reaction in multiple samples. Our findings demonstrate that this technique is highly sensitive to changes in electronic structure, making it a valuable tool for tracking the evolution of chemical processes. Specifically, we were able to capture the dynamics of electron-phonon coupling immediately following photothermal excitation with a 785 nm laser pump, as well as the structural dynamics occurring at longer delays after a rapid increase in lattice temperature.

Through EUV TA maps across the Fe $M_{2,3}$ edge of α-Fe_2O_3, we observed a blue-shift in the zero crossing, a characteristic feature associated with the formation of small polarons in hematite. This indicates two-photon absorption as the dominant photoexcitation mechanism. Notably, we observed differences in the magnitude of this blue-shift when comparing hematite samples deposited on aluminum and parylene substrates. Supported by theoretical calculations, we have provided an interpretation for these substrate-dependent variations in the transient spectra, attributing them to an electron transfer between aluminum and hematite.

However, despite meeting all the necessary requirements to trigger the chemical reaction, we did not observe clear evidence of its progression beyond the electron transfer from aluminum to hematite. This may be due to a lack of contrast in the TA signal, as the reaction predominantly occurs at the interface. The decrease in density within the volume probed by the FEL (free-electron laser) and the removal of gaseous species significantly decrease the probability of reaching the self-sustaining regime. Additionally, the time delays we examined ranged up to hundreds of picoseconds, which may not have been sufficient to capture the full progression of the reaction.

2.3.4 Outlooks

A crucial aspect to be deeply inspected should be the fluence of the laser pump. Indeed, the laser pump fluence should be scanned to establish the optimal intensity that allows to heat the sample to a temperature which is high enough to trigger the redox process without causing hydrodynamic expansion. Furthermore, the samples could be modified to avoid the problem of withdrawal of the gaseous species by adding additional layers, transparent to the laser and as much as possible to the FEL, that would act as a confinement for the gaseous species produced by the laser pump and by the heat released during the first stages, preventing them to be withdrawn from the reaction site because of the low pressure present in the experimental chamber.

The reaction probably takes place in the nanoseconds to microseconds timescale, hence to observe its evolution a pump-probe setup with a microseconds resolution would be desirable. To this regard, XFEL would be a suitable source, since it produces pulse trains in which the separation

between the individual pulses are in the order of microseconds. XFEL would allows for probing K and L edges of aluminium and iron respectively in the hard X-rays regime, removing the constrain to work in vacuum which is unavoidable with EUV. This would facilitate the proceeding of the reaction, since a consistent part of the redox reaction has been proved to occur in the gas phase. Another option would be that of using hard X-Rays to probe the process at deeper core levels, which, on one hand, would not require working in vacuum, and, on the other hand, would offer the benefit of achieving a significantly higher penetration depth. This would allow to work with more complex sample structure, *e.g.* multilayers, which,in turn, would maximize the number of interfaces in the probed volume giving more contrast to observe changes associated with the redox reaction.

2.3.5 Materials and methods

Samples

The samples investigated in this experiment were large-area, customized self-standing nanolayered thin filters, approximately 20 mm in diameter. The samples were provided by Luxel Corporation:

- α-Fe_2O_3 (20 nm) deposited on Al (100 nm): this was the master sample, dedicated to the actual study of the thermite reaction and it was employed in both the sets of measurements, the one performed at the Fe $M_{2,3}$ edge and the one at the Al $L_{2,3}$ edge;
- α-Fe_2O_3 (20 nm) deposited on Parylene-C (100 nm): this sample was dedicated for investigating the dynamics of bare α-Fe_2O_3 at the Fe $M_{2,3}$ edge. The Parylene substrate was necessary for depositing the thin layer of α-Fe_2O_3 and for supporting it. However, Parylene may be considered inert and it should not engage in chemical processes with α-Fe_2O_3;
- Al (100 nm) to serve as a reference for the dynamics of Al accross the $L_{2,3}$ edge.

Pump-probe setup

The experiment was performed at the EIS-TIMEX end station. The laser pump employed for the measurements is a portion of the 785 nm fundamental emission of the Ti:Sapphire laser, delivered to the experimental hall from the femtosecond laser facility of FERMI [37]. The design developed at FERMI (see section 1.5.2 on pag. 14 for more details) for pump-probe experiments exploiting the SLU provides a jitter of just few femtoseconds [38]. Hence, the aforementioned factors offer an experimental environment which is robust and well-suited for the present investigation. T he pump pulse duration was approximately 80 fs FWHM, with a spot size on the sample of 34×34 μm^2 FWHM. The laser intensity was set to 25 μJ to achieve a fluence of $\sim$0.9 J·cm^{-2} on the sample. This pump fluence induces irreversible damage (ablation) at each shot. Therefore, the measurement proceeds in raster scan, single-shot mode - moving to a fresh region of the sample after each pump shot. This approach is crucial for investigating an irreversible process like the thermite reaction. The motion of the sample holder during the raster scan measurements is automated, but the sample plane is constantly adjusted manually to maintain optimal focus for every single pump-probe shot. The radiation of the FEL was used to probe the Fe $M_{2,3}$ edge in the range of photon energy from 54 to 58 eV and for probing the Al $L_{2,3}$ edge in the range from 73 to 76 eV. The FEL pulse d uration was 60 fs FWHM while the intensity was 3 μJ. The intensity was estimated by a calibrated ionization chamber located along the beam transport and filled with N_2. Spot size of the FEL was 16×16 μm^2 FWHM and the fluence at the sample was $\sim$60 μJ·cm^{-2}. In this experimental conditions, we did not observed any noticeable damage caused by the probe beam. The emission

of FERMI is very narrow compared with those of SASE FELs, indeed the spectral broadening factor, i.e. $\Delta\lambda/\lambda$, is of the order of 10^{-3} or 10^{-4}, therefore no monochromators are employed along the beam transport. The spectrum of the FEL along the beam transport is monitored by the EUV spectrometer PRESTO (see section 1.5.3 on pag. 16). The detector employed for this experiment is a second EUV/soft X-Rays spectrometer: WEST (see section 1.6.4 on pag. 26). WEST and PRESTO spectrometers have a resolving power respectively of ~ 7000 and ~ 25000, which is adequate for monitoring the FEL peaks profile. The combination of two spectrometers, one upstream (I_{up}) and one downstream (I_{down}), allows for drawing a calibration curve for I_{down} as a function of I_{up} without the sample, providing a measure of the transmission efficiency of the beamline for each photon energy employed in the experiment, which is then used during the data processing to isolate the variation of intensity caused by the sample.

Static Fe $M_{2,3}$ edge calculations on FeO and α-Fe_2O_3

The calculations performed for supporting the experimental observations were performed by our collaborator at Caltech, Wonseok Lee, who is a PhD candidate in the group of prof. Scott K. Cushing. The OCEAN code was used to simulate static Fe $M_{2,3}$ edge of two iron oxides with different Fe oxidation states (Fe^{2+} for FeO and Fe^{3+} for α-Fe_2O_3) [110, 111]. DFT+U calculations were performed with the Quantum ESPRESSO package using pseudopotentials with the Perdew-Burke-Ernzerhof generalized gradient approximation exchange-correlation functionals [112, 113]. A cutoff energy of 240 Ryd was used for the plane-wave basis set truncation in the DFT calculation. The self-consistent field calculation was done on a 6×6×6 k-point grid while the screening calculation was done on a 2×2×2 k-point grid. The number of bands in the screening calculation is consistent between the different structures and the same energy range of unoccupied bands (100 eV) was used for screening calculations for both iron oxides. Lorentzian broadening of 0.8 eV was set to match experimental data. For relative energy alignment, the energy axis of the simulated α-Fe_2O_3 spectrum was first matched to the experimental α-Fe_2O_3 spectrum and then the simulated FeO spectrum was aligned using the relative energy shift from Fe^{3+} to Fe^{2+} obtained from the OCEAN calculation.

Raw data processing

As the first step in the data analysis, the beamline transmission is measured and the two spectrometers, PRESTO (upstream) and WEST (downstream), are calibrated for each photon energy used in the experiment. This calibration is performed without the sample before measuring at each photon energy. The signal for both spectrometers is obtained by reading the output current of the CCD sensor in full vertical binning mode. The signal is then extracted by integrating over the spectral region of interest. To account for background noise, the integral over the extracted baseline is subtracted from the total integral.

A correlation function between PRESTO and WEST counts is established to determine the beamline transmission in the working configuration without the sample. The correlation function expresses the WEST counts as a linear function fitted to the PRESTO counts (see Fig. 2.9). The measured FEL shots are binned into 500 shots intervals of PRESTO counts. For each bin, the average of the WEST counts is computed along with its standard deviation as the error. The fit is then performed on the binned values, weighting each point by the reciprocal of the squared error. The function employed for the fit is a simple line $f(x) = p_1 \cdot x + p_2$, with $p_1 = 1.86 \pm 0.045$ and $p_2 = 713 \pm 142$.

In the raster scan pump-probe measurements, the transmission of the unperturbed sample, I_{pre},

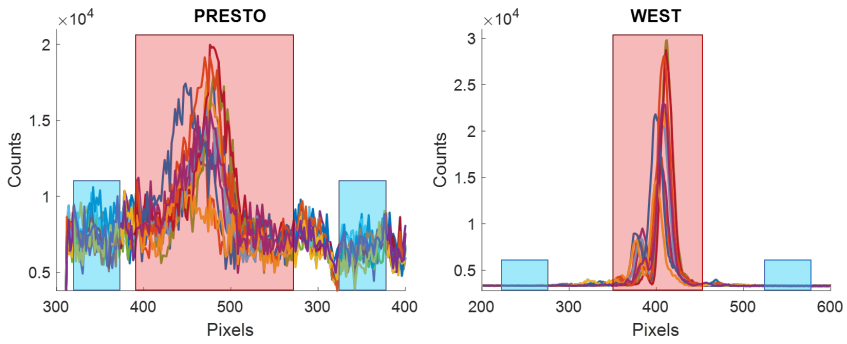

Figure 2.8: Spectra of 10 shots measured with PRESTO (on the left panel) and with WEST (on the right panel). The blue rectangles highlight the region whose area underneath was taken as the background, while the red rectangles highlight the region whose area underneath was taken to calculate the signal by subtracting the background.

is measured 5 times before the pump-probe shot, I_{pp}. Then, 2 measurements of the crater, I_{post}, generated by the pump beam are taken as a sanity check. This procedure is repeated 5 times for each pump-probe delay. Hence, for every delay at least 40 FEL pulses are needed:

- 25 preshot measurements;
- 5 pump-probe shots;
- 10 postshots measurements.

The data is then processed to obtain averaged values and errors for I_{pre}, I_{pp}, and I_{post} at each delay. The transient transmission is calculated as:

$$\Delta T = \frac{I_{pp} - I_{pre}}{I_{pre}} \tag{2.2}$$

The temporal sampling was selected to probe both the ultrafast electron-phonon coupling dynamics near time zero in steps of 100 fs, as well as the slower lattice dynamics at larger delays in steps of 10 ps. Intermediate steps of 1 ps were taken in the transitional region between these two temporal regimes. The pump-probe shots are filtered using the quantile approach. The set of pump-probe transmission values are used to generate 10 evenly spaced quantile values. Shots with intensities above the 90% quantile or below the 10% quantile are discarded. This removes shots whose intensity significantly differs from the median. Accordingly, the associated preshots and postshots of the removed pump-probe shots are discarded as well. For the filtered shots, the transmission values of the preshots, pump-probe, and postshots are plotted against the delays to visualize the measurement at the monitored photon energy.

The overall trend can be summarized as:

- The preshots and pump-probe shots have significantly lower intensity than the postshots. This is expected since the preshots and pump-probe shots interact with the sample, while the postshots pass through the chamber unaffected after the pump ablates the sample. Thus, the postshot transmission should always be close to 1.
- The pump-probe shot intensities cover a wider range compared to the preshots.

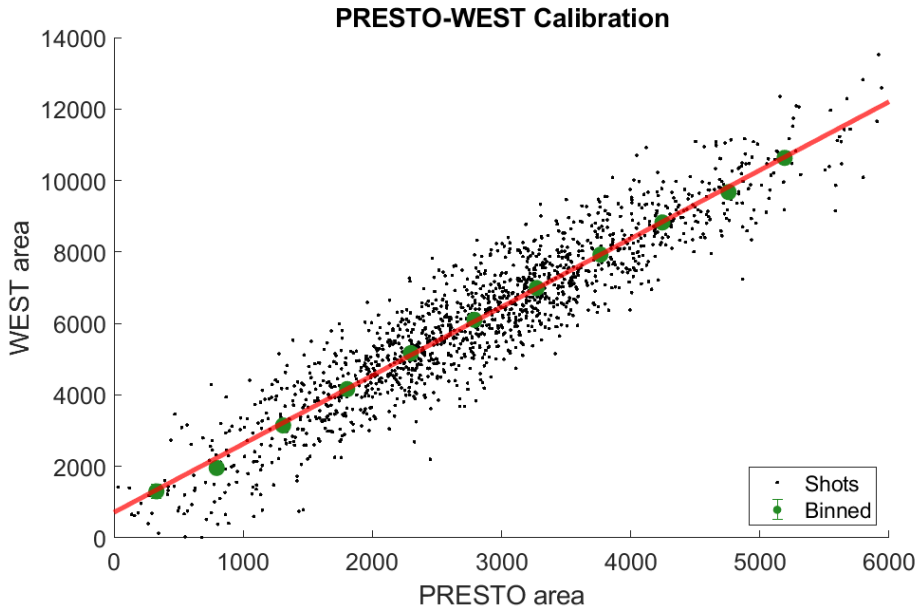

Figure 2.9: Calibration function between the two spectrometers PRESTO and WEST. The black dots are the shots measured. The green dots with the errorbars are the binned values, while the red line is the linear fit. The errorbars are not visible in the figure because they are really small compared to the size of the green dots.

The intensity of the WEST spectrometer (I1) has been plotted against the intensity of the PRESTO spectrometer (I0) to check their correlation for the preshots, the pump-probe and the postshots (bottom panels of Fig.2.10). After the initial filtering, we conducted a binning procedure to derive a single transmission value with an associated confidence interval for each measured delay. This binning process is applied separately to the preshots, pump-probe, and postshots. It involves calculating the average of the transmission values T_j^{bin} and determining the error σ_{T_j}, as expressed in the following equation:

$$T_j^{bin} = \frac{1}{n_j}\sum_{i=1}^{n_j} T_i^j \qquad\qquad \sigma_{T_j} = \sqrt{\frac{1}{n_j - 1}\sum_{i=1}^{n_j}(T_i^j - \bar{T}^j)^2} \tag{2.3}$$

where the index j represent preshots, pump-probe or postshots and n is the number of shots within these groups for a single delay.

The normalized variation of transmission of the pump-probe measurements is calculated as follows:

$$\Delta T_{norm} = \frac{\Delta T}{T_{pre}} = \frac{T_{pp} - T_{pre}}{T_{pre}} \tag{2.4}$$

and the propagation of the errors is calculated accordingly[2]:

[2]The variables T_{pre} and T_{pp}, as well as their standard deviations $\sigma_{T_{pp}}$ and $\sigma_{T_{pre}}$, are considered couples of uncorrelated variables. Therefore, the double products are neglected and only the square terms are considered in the error propagation.

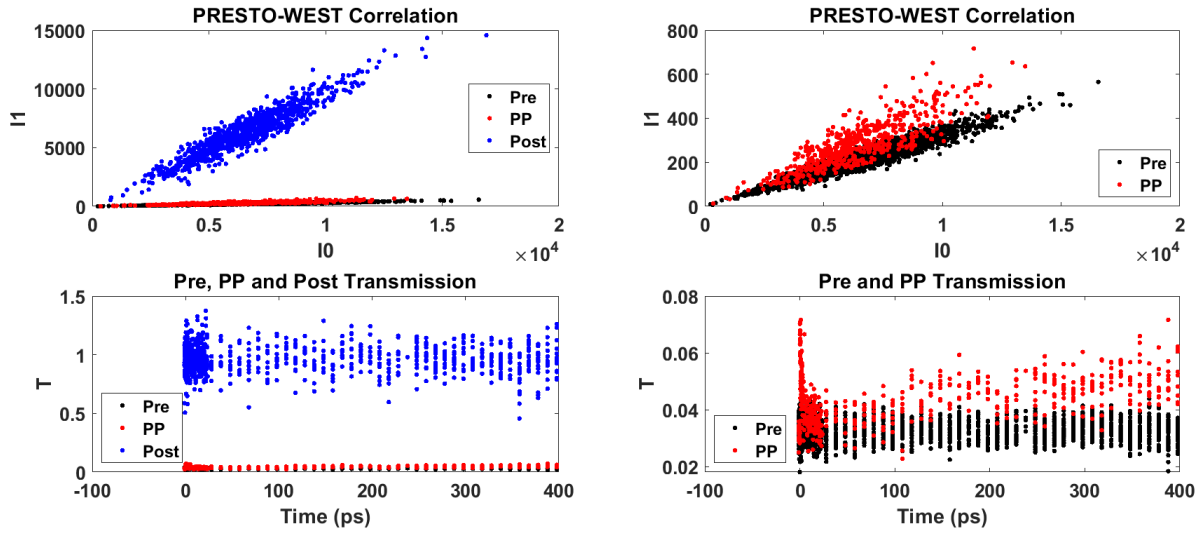

(a) (b)

Figure 2.10: Unprocessed transmission of the filtered measurements (top panels) and correlation between PRESTO (upstream) and WEST (dowstream) spectrometers (bottom panels) for (a) preshots, pump-probe and postshots and (b) preshots and pump-probe.

$$\begin{aligned}\sigma_{\Delta T} &= \sqrt{\left(\frac{1}{T_{pre}}\cdot\sigma_{T_{pp}}\right)^2+\left(\frac{1}{T_{pre}}\cdot\sigma_{T_{pre}}\right)^2+\frac{2}{T_{pre}}\cdot\sigma_{T_{pp}T_{pre}}+\left[\frac{T_{pp}-T_{pre}}{T_{pre}^2}\cdot\sigma_{T_{pre}}\right]^2}\\ &\approx \sqrt{\left(\frac{1}{T_{pre}}\cdot\sigma_{T_{pp}}\right)^2+\left(\frac{1}{T_{pre}}\cdot\sigma_{T_{pre}}\right)^2+\left(\frac{T_{pp}}{T_{pre}^2}\cdot\sigma_{T_{pre}}\right)^2-\left(\frac{1}{T_{pre}}\cdot\sigma_{T_{pre}}\right)^2}\\ &\approx \sqrt{\left(\frac{1}{T_{pre}}\cdot\sigma_{T_{pp}}\right)^2+\left(\frac{T_{pp}}{T_{pre}^2}\cdot\sigma_{T_{pre}}\right)^2}\end{aligned} \tag{2.5}$$

The normalized transmission and its associated errors (obtained respectively from eq.2.4 and 2.5) are plotted against the pump-probe delays to obtain the refined time-dependent trace reported in Fig. 2.11a.

The transmission is then manipulated in order to obtain the time-dependent trace in terms of the variation of absorbance (ΔA), calculated as follows:

$$\Delta A = A_{pp} - A_{pre} = log(1/T_{pp}) - log(1/T_{pre}) = log(T_{pre}) - log(T_{pp}) \tag{2.6}$$

The interval of confidence of the absorbance values is no longer symmetric with respect to the values themselves because of the logarithm. Hence, the interval of confidence in the absorption scale is computed by taking the logarithm of the upper and lower bounds of the interval of confidence in the transmission scale, as illustrated in the following equation:

$$A_{lower} = -log(T_{pp} - 0.5\cdot\sigma_{T_{pp}}) \qquad A_{upper} = -log(T_{pp} + 0.5\cdot\sigma_{T_{pp}}) \tag{2.7}$$

The absorbance values and their associated intervals of confidence are employed to generate the transient absorption trace reported in Fig. 2.11b.

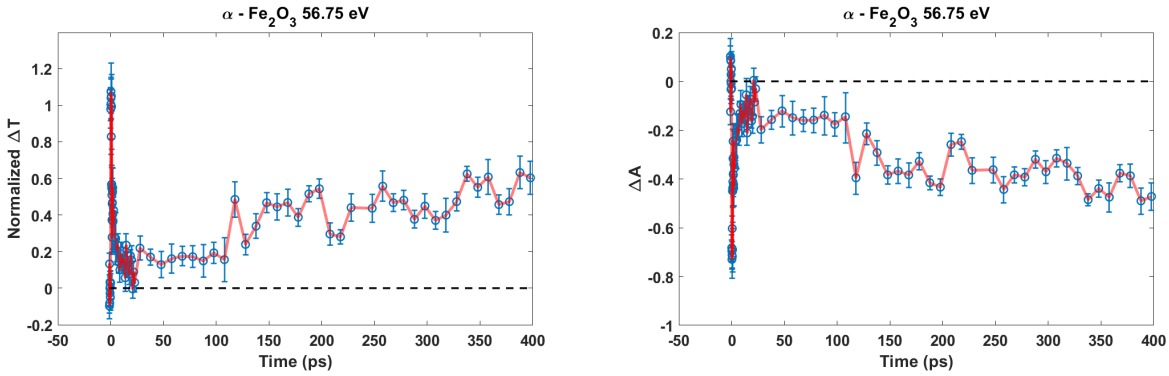

(a) (b)

Figure 2.11: Processed transmission (a) and transient absorption (b) for the pump-probe time-dependent traces.

Neglecting the jitter between the pump and the probe, which at FERMI is just few femtoseconds, the temporal resolution for the pump-probe signal around t_0 is limited by the convolution between the duration of the pump pulse ($\sigma^t_{\text{pump}} \sim 80$ fs) and the probe pulse ($\sigma^t_{\text{probe}} \sim 60$ fs):

$$\Delta t_{lim} = \sqrt{[\sigma^t_{\text{pump}}]^2 + [\sigma^t_{\text{probe}}]^2} = \sqrt{80^2 + 60^2} \simeq 100 \text{ fs} \tag{2.8}$$

The raise at t0 was fitted for the traces of Al and α-Fe_2O_3 reported in Fig. 2.12 using an error function:

$$f_r = a \cdot \left[1 + erf\left(\frac{t}{\sigma \cdot \sqrt{2}}\right)\right] \qquad \text{where} \quad erf(x) = \frac{1}{\sqrt{2\pi}} \cdot \int_{x_1}^{x_2} e^{-x^2} dx \tag{2.9}$$

The values of σ resulting from the fit were respectively 44 ± 12 fs for Al and 27 ± 2 fs for Fe_2O_3 The rise time FWHM was calculated 65 fs for α-Fe_2O_3 and 102 fs for Al. In this measurements the focus was on longer dynamics, so the temporal mesh in the proximity of time zero was 0.1 ps. As a consequence, the number of points in this pump-probe delay region does not allow to accurately determine the raise time. Nonetheless, the estimate provided with the fit of eq. 2.9 is compatible with the convolution of the pump and probe pulses.

The choice for the function used to fit the overall pump probe traces was made with the goal of fitting two processes that occur with different time scales:

- fast dynamic: the equilibration of hot electrons with the lattice via scattering off with optical phonons, which occurs in hundreds of femtoseconds to the first few picoseconds;
- slow dynamic: the dynamics of the lattice which is stressed by the ultrafast rising of the temperature, which occurs in tens to hundreds of picoseconds.

The equation adopted for the fit of the dynamics at energies above the inflection point of the absorption edges was the following:

$$f = \theta(t) \cdot \underbrace{\frac{1}{2}\left[1 + erf\left(\frac{t}{\sigma \cdot \sqrt{2}}\right)\right]}_{\text{time resolution}} \cdot \underbrace{\left[A_1 e^{-\frac{t}{\tau_1}}\right]}_{\text{fast dynamic}} + \underbrace{\frac{A_2}{1 + e^{-\frac{1}{\tau_2}(t-z)}}}_{\text{slow dynamic}} \tag{2.10}$$

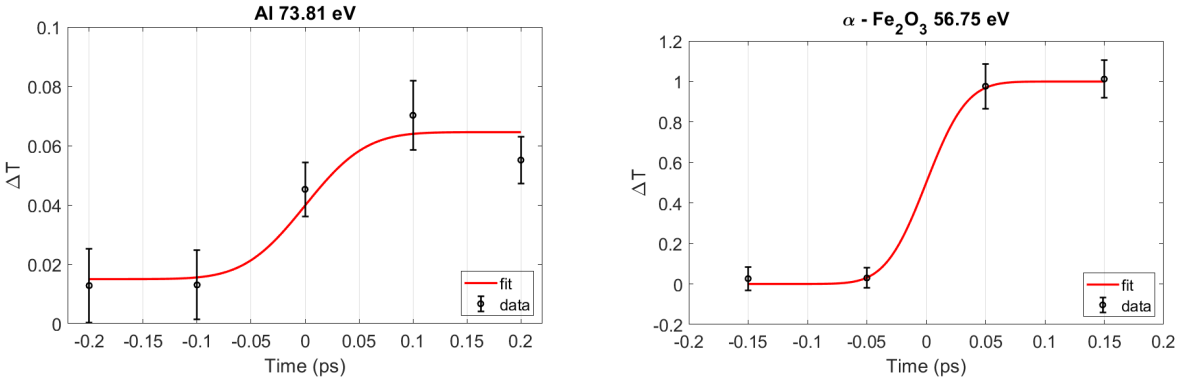

(a) (b)

Figure 2.12: Details of the rise dynamics of Al (a) and Fe (b) around delay zero between laser pump and FEL probe.

The equation employed to fit the dynamics at energies below the inflection point of the absorption edges was slightly different:

$$f = \theta(t) \cdot \underbrace{\frac{1}{2}\left[1 + erf\left(\frac{t}{\sigma \cdot \sqrt{2}}\right)\right]}_{\text{time resolution}} \cdot \underbrace{\left[\frac{A_1}{1 + e^{-\frac{t}{\tau_1}}}\right]}_{\text{fast dynamic}} + \underbrace{\frac{A_2}{1 + e^{\frac{1}{\tau_2}(t-z)}}}_{\text{slow dynamic}} \tag{2.11}$$

In equations 2.10 and 2.11, t is the independent variable corresponding to the delay between the pump and probe beams. θ is the heaviside function, σ is the parameter associated with the time resolution from eq. 2.9. A_1 and A_2 are pre-exponential factors, τ_1 and τ_2 are the kinetic constants for the fast and slow dynamics, respectively, and z represents the time when the slow lattice dynamic becomes the dominant contribution.

The only difference between equations 2.10 and 2.11 is the term describing the fast dynamic. In the first case, an exponential was chosen, agreeing with other transient absorption studies in literature, but in the second case (i.e. energies below the absorption edge), we used a logistic function for fitting. An exponential with a negative pre-exponential did not work for fitting the dynamics below the absorption edge, likely because the transmission trend is discordant between pump-probe traces above and below the absorption edge for the fast dynamic, while it is concordant for the slow dynamic. Regardless, the fits yielded similar kinetic constants.

Interestingly, for the dynamic measured at 56.49 eV, a different function was used to fit the first decay after t_0, featuring an additional exponential decay term for the fast dynamic (indicated in the following equation with the apex $*$):

$$f = \theta(t) \cdot \underbrace{\frac{1}{2}\left[1 + erf\left(\frac{t}{\sigma \cdot \sqrt{2}}\right)\right]}_{\text{time resolution}} \cdot \underbrace{\left[A_1 e^{-\frac{t}{\tau_1}} + A_1^* e^{-\frac{t}{\tau_1^*}}\right]}_{\text{fast dynamic}} + \underbrace{\frac{A_2}{1 + e^{-\frac{1}{\tau_2}(t-z)}}}_{\text{slow dynamic}} \tag{2.12}$$

The fitting of the transient absorption spectra was performed using a parametrized sigmoid function (s(x)), which provided the flexibility to adapt to the different shapes of the spectra over the delays investigated. The function adopted is reported below:

$$s(x; a_0, b_0, x_0, y_0) = \frac{a_0}{1 + e^{-b_0(x-x_0)}} + y_0 \tag{2.13}$$

where a_0, b_0, x_0, y_0 are the parameters. This function has been employed in a non-linear least square fitting procedure in order to fit the transient spectra of the individual delays by finding the optimal set of the parameters of the sigmoid function. The weight of each experimental point in the fit has been set as the reciprocal of the associated error on the absorbance. Being the confidence interval of the absorption asymmetric, the error has been considered as the the total uncertainty. For the fitting of the Al Al $L_{2,3}$ edge transient absorption spectra (left panel of Fig. **??**ta), the model have been generalized and the difference between two parametrized sigmoid functions was employed, where the second one was fixed and was the taken as the fitted sigmoid for the static absorption at negative delays. In this way only the parameters of the first sigmoid where optimized during the fitting procedure.

Chapter 3

Non-collinear EUV based techniques

3.1 Noncollinear, inelastic four wave mixing

3.1.1 Introduction

The availability of intense and coherent light sources as lasers has paved the way for the development of non-linear optics techniques (NLO). NLO phenomena are usually observed in presence of intense radiation fields, since the terms higher than the first order in the expansion of eq. 1.32 have a small magnitude. In this condition, multiple photons could simultaneously interact with a material, driving the generation of an output radiation field, *i.e.* the signal. In the visible and IR portions of the electromagnetic spectrum, non-linear methods have been extensively exploited to investigate dynamics and correlations which would have been otherwise unapproachable. Additionally, the use of more than one radiation field to investigate the sample allows for the so called non collinear experimental schemes. Essentially, several beams are guided onto the sample, each having its own direction, resulting in the production of a signal in a direction that would be different from those of the input beams because of the law of conservation of energy and momentum. Therefore, on the one hand, the realization of setups for non-collinear experiments usually entails a higher level of technical challenges with respect to collinear counterparts, but on the other hand, it rewards the additional effort associated with the more complex geometry of the experimental scheme with a significant enhancement of the signal to noise ratio thanks to the emission of the signal in a background-free direction, allowing to detect even a small quantity of output photons. Nonetheless, NLO techniques exploiting optical fields are not suitable for studying properties of structures and excitation dynamics below the hundreds of nm scale, because the accessible length scale is intrinsically limited by the relatively large wavevector (k) and small photon energy (E) associated with optical photons.

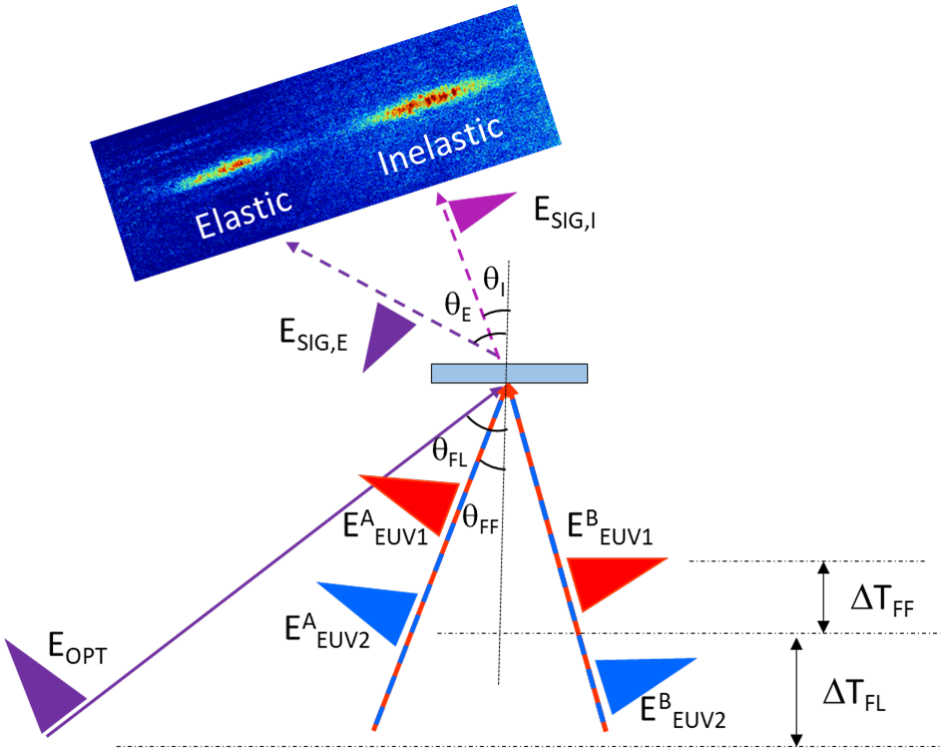

Figure 3.1: Illustration of the experimental setup. Two couples of FEL pulses with energies E_{EUV1} and E_{EUV2} are overlapped at the sample with an angle $2\theta_{FF} = 5.4°$. The labels A and B refers to the different pumps while 1 and 2 are meant to sort the arrival order of the two different colors of the FEL emission. The optical probe beam with $E_{opt} = 3.2$ eV impinge on the FEL crossing point with an angle $2\theta_{FL} = 45°$. The pulses E^A_{EUV1} and E^B_{EUV2} are respectively the 'pre-pulse' and the 'post-pulse', because they are not relevant for the experiment but they could not be filtered out with the mini-TIMER setup. The output of the experiment consist of two signals: elastic ($E_{SIG,E}$) and inelastic ($E_{SIG,I}$). A high bandpass filter was placed in front of the camera but it not represented in the figure. Imaged reproduced from [49].

As predicted by several theoretical works [114, 115], the use of EUV or X-Rays beams in NLO experiments would grant the possibility of overcoming the aforementioned limitations by performing groundbreaking experiments, accessing properties at the tens of nm scale or even at the molecular scale with the additional benefit of the chemical selectivity which stems from the atom specific transitions. Indeed, the development of HHG and FEL light sources have made EUV and X-Rays intense ultrashort pulses available, which, in turn, have led to the successful conduction of a series of milestone studies of NLO in these unexplored ranges of wavelengths [76, 116–120]. Particularly significant for its affinity with the technique presented in this section, is the pioneering work by Rottke *et al.* [121], where two optical pulses and an EUV pulse resonant with the lithium K edge ($\approx$ 62 eV) are used to irradiate the sample in a reflective collinear geometry in order to study electron and hole colocalization. The relevance of this investigation is given by the fact that it has proven the rise of an inelastic signal in a four wave mixing experiment, *i.e.* a signal with a photon energy that differs from both the one of the optical photons and the one of the EUV photon: $E_{sign} = E_{EUV} \pm 2E_{optical}$. The yield of generation of sum-frequency and difference-frequency FWM signals as a function of the EUV photon energy is exploited to assess the degree of charge localization of the so generated core-hole exciton.

The experiment presented in this section was performed using the mini-TIMER setup [122], a compact setup hosted in the DiProI end-station [123] at FERMI. The setup is based on three carbon-coated mirrors installed on top of four fully encoded piezoelectric actuators that allow their along-beam translation and horizontal positioning. The focusing is obtained with the Kirkpatrick-Baez active mirrors system of the beamline [124]. The standard configuration of such setup generates a TG with $L_{TG} \sim 280$ nm using the fully reflective approach described above. The TG is probed with an optical pulse at 400 nm, impinging on the sample with an angle of 45°. On the one hand, the optical probe limits the period of the TGs that could be investigated to $L_{TG} > \lambda_{probe}/2$, but on the other hand it is sensitive to intraband transition channels [125], and are also sensitive to changes in the valence band structure and to electronic populations transiently generated in the conduction band. In the experiment discussed in this section, two FEL pulses (with photon energy and momenta respectively E_{EUVi} and k_i, with $i = 1, 2$) and an optical pulse (with $E_{opt} = 3.2$ eV and k_3) are combined at the sample to generate an inelastic FWM signal characterized by an energy $E_I = E_{opt} + \Delta E$, where $\Delta E = E_{EUV2} - E_{EUV1}$ and an associated momentum k whose direction is determined by the vector sum $k_1 - k_2 + k_3$, according with the law of conservation of energy and momentum. The mechanism of excitation could be intuitively thought of as a spatial excitation grating that translates during the time interval spanned by the EUV illumination with a velocity and a direction respectively:

$$\underbrace{v = \frac{\Delta E}{\hbar|\vec{k}|}}_{\text{velocity of the grating}} \qquad \underbrace{\vec{k} = \vec{k}_2 - \vec{k}_1}_{\text{direction of the grating}} \tag{3.1}$$

With respect to the work of Rottke *et al.*, the setup used in this experiment (sketched in Fig. 3.1a) is designed for adopting a non-collinear approach, granting few significant benefits:

(i) As stated above, a substantial improvement of the signal-to-noise (S/N) ratio compared to an equivalent collinear setup. This has allowed the observation of FWM signals even outside the condition of resonance with core-hole transitions, a situation where the intensity of such signals is expected to be smaller by ~ 2 orders of magnitude.

(ii) The possibility of varying both the delay between the two EUV pulses and the delay between them and the optical pulse for monitoring the dependence of the non-linear response of the sample on these degrees of freedom;

(iii) The opportunity of exploring the momentum space of the excitation grating ($k_T G$) by modifying the angle between the two EUV pulses ($2\theta_{FF}$ in Fig. 3.1a) while keeping the two EUV photon energies constant. Tuning the FEL emission to a photon energy resonant with a core-hole transition and scanning the k of the excitation grating could access spatial information on the location of such core-holes [114, 126, 127].

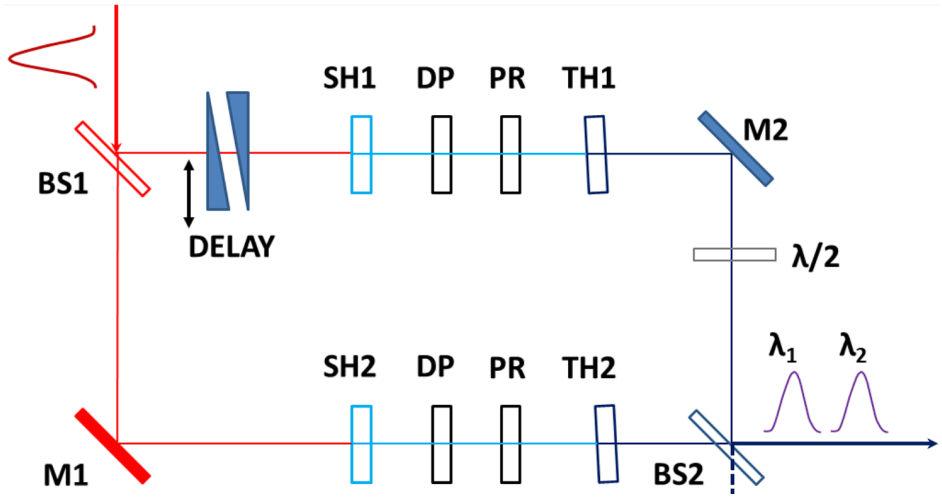

Figure 3.2: The optical configuration for the twin-pulse generation scheme of the UV seed laser system employed in the experiment involves several components. Each third harmonic generation (THG) line comprises a type 1 second harmonic generation (SHG) BBO crystal, a birefringent delay plate, a polarization rotator that specifically rotates the polarization of the second harmonic light by 90 °, and a type 1 THG BBO crystal mounted on a rotation stage. By incorporating a pair of 4 ° fused silica wedges, the upper arm of the setup can achieve a delay ranging up to 2.5 picoseconds. Image reproduced from [26].

3.1.2 Materials and methods

A sketch of the experimental setup at the DiProI end-station is shown in Fig. 3.1a. The mini-TIMER setup is devised for performing non-collinear EUV TG experiments with an optical probe. In this particular measurement, the potential of the FERMI seeded FEL was exploited to generate two FEL pulses through the twin-seeded configuration [26], which uses two UV seed pulses slightly separated in terms of wavelength to seed the same electron bunch. The two seed pulses are obtained by splitting the fundamental of the Ti:Sapphire laser of the femtosecond laser facility (see section 1.5.2) into two parallel third harmonic generation arms (see Fig. 3.1b). A pair of 4° fused silica wedges positioned in one of the two branches permits to control the delay between the two seed pulses and, in turn, the delay between the two generated FEL pulses up to 2.5 ps in steps of 50 fs. Panel a of Fig. 3.3 illustrates the configuration of the machine for the generation of twin-seed FEL radiation. In the present experiment, the two EUV pulses where set to $E_{EUV1} = 47.7$ eV and $E_{EUV2} = 47.88$, with the possibility of varying E_{EUV2} from 47.7 to 48.2 eV. The time duration of the pulses was estimated to be 50 fs FWHM and the separation between the two pulses to be 150 fs. An exemplary averaged spectrum and the stability and the intensity ratio of the twin FEL pulses is reported in Fig. 3.4. The fluence at the sample was calculated to be 40 mJ/cm^2. Each of the two pulses is splitted in two branches (A and B) by the mini-TIMER setup and rejoined at the sample with an angle $2\theta_{FF} = 5.4°$ between them. The optical probe was directed on the sample with an angle $\theta_{FL} = 45°$ with a photon energy $E_{opt} = 3.16$ eV, a fluence of 3 µJ and a pulse duration estimated to be ≈ 100 fs. The sample was a diamond crystal, which is characterized by radiation resistance and high cross-section of the non-linear response [128–130]. The detector employed for the experiment was a position-sensitive camera (PI-MTE) which was positioned off-beam, since the non-collinear geometry produces signals in directions that differs from the one of the transmitted radiation. The camera was placed in such a way to detect both the inelastic signal at θ_I with

$E_{SIG,I} = E_{opt} + \Delta E$, with $\Delta E = 180meV$, and the elastic signal at θ_E with $E_{SIG,E} = E_{opt}$.

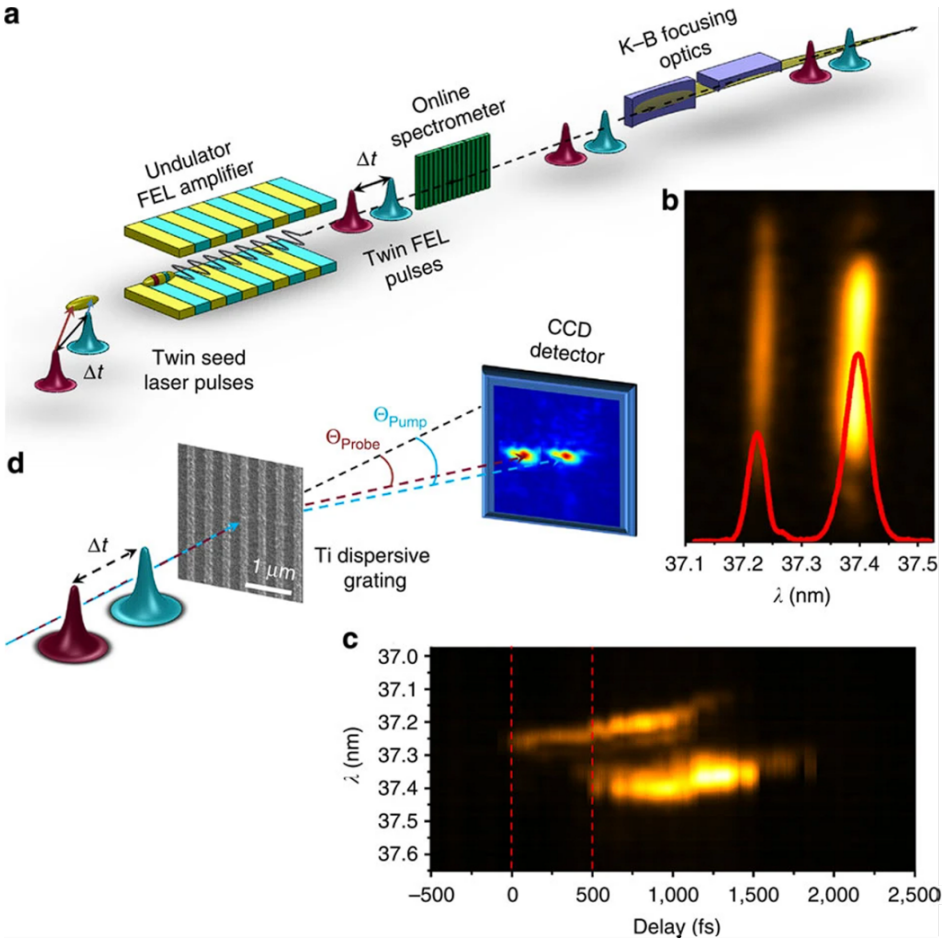

Figure 3.3: (a) From the left, the twin-seed pulses separated both in photon energy and in time, as shown in Fig. 3.1b, interact with the electron bunch. Inside the undulators, the two seed pulses acts independently over two distinct portions of the electron bunch. The properties of the resulting FEL pulses, *e.g.* wavelength and relative delay, are strictly related to the parameters of the two seeds. The spectra of the two FEL pulses are monitored online with the PRESTO spectrometer. (b) Example of a twin-seed FEL spectrum. (c) Delay scan of the two seed pulses with respect to the electron bunch. The time separation of the two FEL pulses is highlighted by the two dashed lines and it remains constant over the delay scan of the electron bunch, proving that the time separation of the two FEL pulses is determined by the delay of the two seed pulses. (d) Layout of a demonstrative experiment performed at the DiProI end station which shows that the two FEL pulses have distinct wavelengths. The FEL pulses were focused with the Kirkpatrick-Beaz optics on a nm titanium grating and diffracted on the horizontal plane on a CCD camera. Image adapted from [26]

The spatial separation of the beams on the sensor of the camera reflects the dependence of the diffraction angle on the energy of the emerging signal, acting as spectral characterization. To

improve the S/N, a high bandpass filter was placed in front of the camera, in order to filter residual leaking of light in the experimental chamber and diffuse light at E_{opt}. Furthermore, such filter cuts 99 % of the intensity at $E_{SIG,E}$, while it cuts only $\approx$ 50 % at $E_{SIG,I}$, balancing the intensities of the two different kinds of signal (the elastic contribution has a cross section of $\approx 10^2$ larger than the inelastic one). The presented experimental configuration gives the possibility of scanning the delay between the two EUV pulses thanks to the setup of the twin seed pulses illustrated in Fig. 3.1b, although this option is technically challenging and time-consuming. Normally, the preferential option is that of scanning the delay between the optical laser and the EUV pulses, which is controlled with a delay line along the beam transport of the SLU that permits to modify the arrival time of the latter with respect to the FEL.

The bigger limitation of the setup is the impossibility to prevent the 'pre-pulse' and the 'post-pulse' from reaching the sample (see Fig. 3.1a). The former (E^A_{EUV1}) drives the sample out of its equilibrium, preventing the possibility of investigating ground state phenomena. The latter (E^B_{EUV2}) would interfere with the coherences generated by E^A_{EUV2} and E^B_{EUV1} and inevitable complicate the dynamics observed. The delay ΔT_{FF} refers to the difference in the arrival time on the sample of the two pulses E^A_{EUV2} and E^B_{EUV1}.

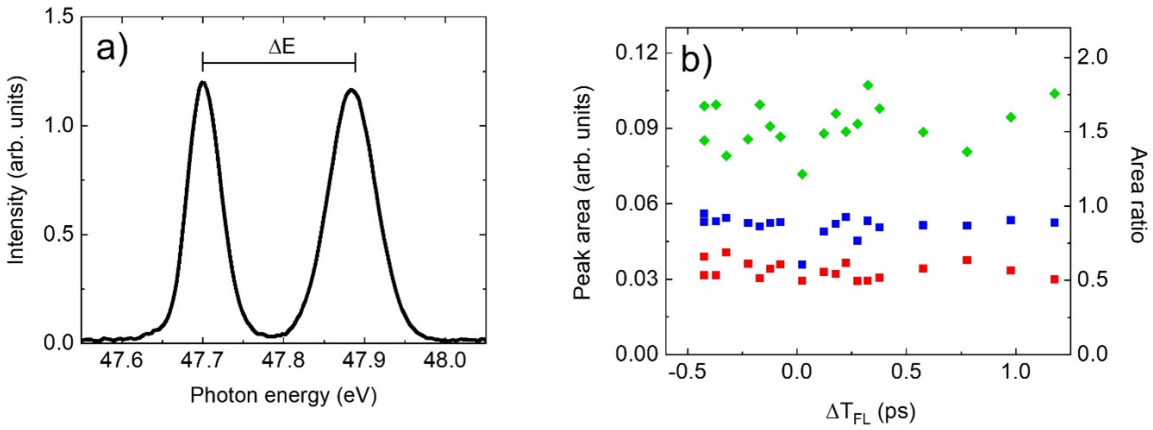

Figure 3.4: (a) FEL spectrum averaged over a time delay scan. (b) peak area of the two FEL pulses (red and blue squares are used for the two individual peaks) on the left vertical axis and ratio of the peak areas (EUV2/EUV1, green squares) on the right vertical axis during a delay scan. Each point is obtained as the average over 3000 FEL shots. Image reproduced from [49].

3.1.3 Results and discussion

The first noteworthy result of this investigation is the simultaneous observation of the elastic and the inelastic signals. Both the elastic and inelastic signal could be adequately described by a gaussian with $\sigma = 40 \pm 5$ fs (see Fig. 3.5 a), which may be ascribed to the FEL-FEL cross-correlation, calculated to be $\geq$ 30 fs.[1] Scans of ΔT_{FF} allows to perform a two-photon echo scan, *i.e.* a non-linear excitation process in which a first photon perturb the sample generating a coherence and a second photon acts on the coherence evolving in the sample, which has the capability of probing the ultrafast dynamics of coherent excitation processes of materials and their dephasing [131]. Nevertheless, here the only observable process would be photoionization, which is faster

[1]The cross-correlation is calculated on the base of the estimated FEL pulse duration, but the actual pulse duration could actually be longer.

than duration of the FEL pulses and therefore inaccessible with the employed setup. Concerning the FEL-SLU delay scans (ΔT_{FL}, see Fig. 3.5 b), the two signals display different dynamics one another. While the inelastic signal is well-represented by a simple gaussian with a $\sigma = 104 \pm 5$ fs, the elastic signal is fitted with an exponentially modified gaussian, whose components have been identified as a gussian, which is the same as the one used to interpret the inelastic signal, and an exponential decay characterized by a time constant of 130 ± 10 fs. The purple gaussian in Fig. 3.5 b is a representation of the FEL-FEL cross-correlation. The gaussian with $\sigma = 104 \pm 5$ fs employed in both the fits of the elastic and in inelastic signals could be associated with the FEL-SLU correlation, which is consistently larger than the FEL-FEL correlation due to the longer pulse duration of the optical pulse and to the large wavefront tilt determined by the large angle of incidence on the sample. The additional decay term observed in the elastic signal could be associate with the electron-lattice relaxation, which is coherent with the results reported in the literature for carbon indicating a timescale on the order of hundreds of fs [66, 132]. In both panels of Fig. 3.5 the intensities of the signals have been normalized by the sum of the squared values of the total FEL intensity[2] in order for the fluctuations of the FEL to be accounted for. A further normalization between the intensity of the elastic signal and the intensity of the inelastic signal have been performed for facilitating the comparison of the dynamics.

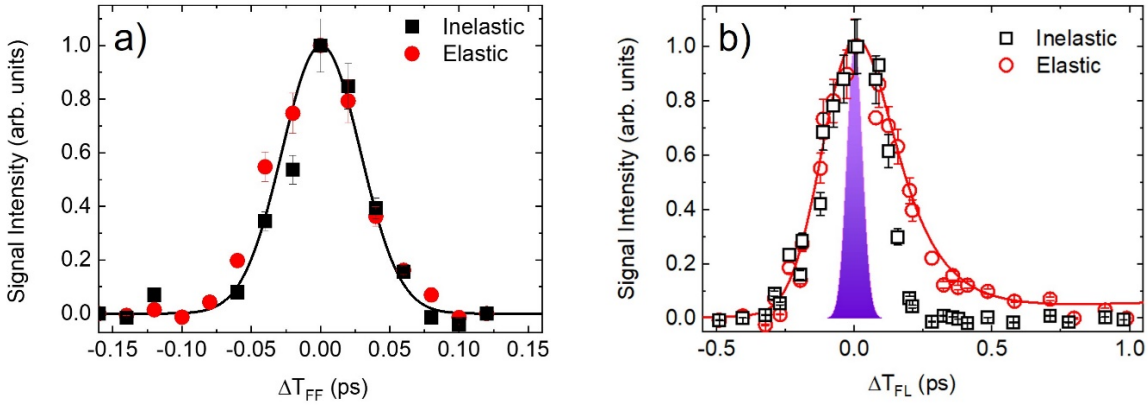

Figure 3.5: (a) Intensity of the two types of signals as a function of the delay between the two FEL pulses. The gaussian shape of both the FWM signals resemble the cross-correlation of the FEL pulses, represented by the solid black line. (b) Dynamics of the inelastic and elastic signals (respectively the open black squares and the red open dots) produced by scanning the FEL-SLU delay. The inelastic signal appears symmetric around t0 and gaussian in shape, reasonably resembling the FEL-SLU cross-correlation. Conversely, the elastic signal displays a different behaviour. Although being identical to the one of the inelastic signal at $\Delta T_{FL} < 0$, it differs at positive delays. Indeed, it is reproduced by an exponentially modified gaussian, where the gaussian contribution is identical to the inelastic signal, while the additional contribution is given by an exponential decay. The FEL-FEL cross-correlation (solid black line in panel a) is as well represented in panel b by a purple gaussian. For both panel a and b the intensities of the two signals have been normalized for the sake of comparison. Image reproduced from [49].

The intensity of the inelastic FWM signal has a quadratic dependence on the FEL fluence (see

[2]Normalization by the square of the total FEL intensity rather than the product of the two individual intensities is justified by the fact that the trend of such intensities is constant (see Fig. 3.4).

Fig.3.6), as expected for a second-order non-linear excitation (photon echo). The intensity of the elastic FWM signal has as well a quadratic dependence on the FEL fluence, because it is another type of second-order non-linear excitation (TG).

The simultaneous detection of the inelastic and elastic FWM signals allows for the direct comparison of their intensities, providing access to the third order susceptibilities[3] , which have been estimated to be $\chi_I^{(3)} = 1.4 \times 10^{-25} \mathrm{m^2 V^{-2}}$ and $\chi_E^{(3)} = 1.5 \times 10^{-23} \mathrm{m^2 V^{-2}}$

The unexpected observation of the elastic signal has been attributed to the spectral contamination of the twin seeded pulses: the two pulses with energy $\mathrm{E_{EUV1}}$ contains some spectral components at energy $\mathrm{E_{EUV2}}$ and viceversa.

The selected ΔE between the FEL pulses (180 meV) should coherently excite an optical phonon in diamond with energy 165 meV [133, 134]. Such excitation would lead to a decay of the inelastic FWM signal in the ps timescale via a coherent Raman scattering mechanism [135, 136], which was not observed in the experiment reported here. This is most likely due to the presence of the pre-pulse that perturbs the ground state of the system and to the effect of the post-pulse which disrupts any coherent excitation induced in the system within $\approx$ 150 fs, preventing the possibility of investigating the relaxation dynamics of such excitation.

3.1.4 Conclusions

This experiment proves the feasibility of generating an inelastic FWM signal using two EUV pulses. The setup employed here did not enable to perform a coherent Raman scattering investigation because of the presence of the pre-pulse and the post-pulse. Nevertheless, the technique of coherent Raman scattering in the EUV regime could be implemented at FERMI at the TIMER beamline, which allows to access smaller TG periodicities. The use of EUV for coherent Raman scattering entails not only the intrinsic chemical selectivity of core-hole excitations, but also the capability of generating and probing electronic coherences over different atoms, which in the context of investigation of chemical reactions traslates in the possibility of tracing charge transfer between different elemental sites and their kinetics in the process of bond-breking/formation.

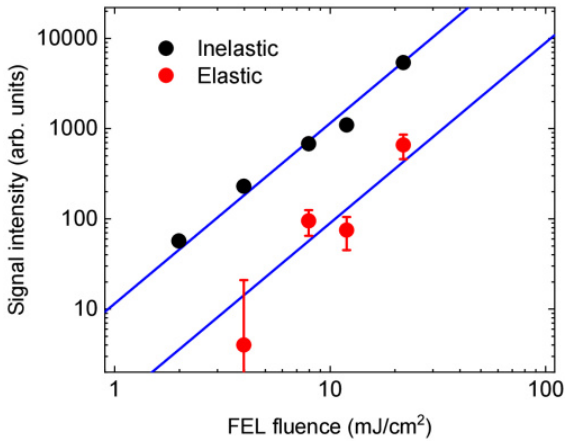

Figure 3.6: Dependence of the intensity of the inelastic (black circles) and elastic (red circles) FWM signal on the FEL fluence at $\Delta T_{FF} = 0 \mathrm{and} \Delta T_{FL} = 0$. The blue line are quadratic fits to the data. Image reproduced from [49].

[3]The estimate of the $\chi_E^{(3)}$ is based on the assumption that the elastic FWM signal intensity is linearly dependent on the spectral overlap.

3.2 Structured illumination

3.2.1 Introduction

In the second half of the 19$^{\text{th}}$ century, the german physicist Ernst Abbe formulated a fundamental theory for the process of image formation in optical microscopes, discovering the limit for the resolution of such devices, which is known as the Abbe relation:

$$d = \frac{\lambda}{2nsin\theta} \tag{3.2}$$

where d is the lower bound for the dimensions of the features that can be resolved, λ is the wavelength of the light used to illuminate the sample, n is the refractive index of the medium between the sample and the objective of the microscope and θ is the largest semi-angle collectable by the imaging optics. In Abbe equation, the wavelength is the only parameter that could be largely varied, hence moving toward shorter wavelengths has been the main strategy adopted to decrease d as much as possible, *i.e.* improving the resolution of the microscope. Indeed, several techniques have been developed exploiting the bright X-Ray radiation produced by synchrotron and FELs, attaining a resolution of $\approx$ 20 nm [137]. Nevertheless, the enhancement of the resolution in this case is hampered by the quality of manufacturing of X-Rays optics rather than the wavelength of the light, which for X-Rays is $<$ 1nm.

To overcome this limitation, different approaches have been elaborated, which rely on free-electrons for illuminating the sample [138, 139] or on proximity forces to probe the sample surface [140]. Although these techniques have proved to be robust and have led to successful experiments [141, 142], they encompass some technical hurdles. Atomic force microscopes provide a very good resolution across the longitudinal axis, but they lack resolution in the transversal plane because of the size of the tip and they can probe only the surface of the sample. Electron microscopes could reach a resolution below 2 Å[143], however they require ultra-high vacuum to maximize the electrons mean-free-path and a thickness of the sample inferior than micrometres.

Reducing the wavelength is not the only strategy to improve the resolution. The work of G. Toraldo di Francia has introduced the concept of super-resolution, devising a system for prevailing Abbe's limit using still visible light [144] and setting the stage for the flourishing of super-resolved techniques that have revolutionized the field of microscopy [145–147].

Among these techniques, is structured illumination microscopy (SIM), that is employed in the experiment discussed in this section. The peculiarity of the technique consist in the use of a beam with a spatial periodic structure that can be expressed in terms of a spatial frequency k_i. If such frequency is close enough to a characteristic spatial frequency of the illuminated sample (k_s), the flourescence will occur in a spatially modulated pattern with spatial frequency k_s - k_i. The pattern of the fluorescence is called moiré fringes and it has a real-space periodicity $\mathrm{L}_M \sim 2\pi$ (k_s - k_i)$^{-1}$ that is usually accessible to the imaging system, because L_M is larger than the individual L_s and L_i, which, conversely could not be imaged by the same imaging system. Therefore, the potential of this technique is that of resolving features with a size below the aforementioned Abbe's limit d through the generation of an interference pattern whose pitch is larger than d [148–150].

Cutting-edge microscopes that utilize visible light have the capability to access the complete spatial information permitted by the Abbe limit. Consequently, employing visible radiation to create structured illumination enables an extension of the spatial resolution by an amount equivalent to k_i. This is illustrated in Fig. 3.7, wherein the unfilled circle represents the range accessible through standard (Abbe-limited) microscopy, while the yellow circles are shifted by k_i. Through the acquisition of multiple images featuring varying orientations and phases of the illuminating

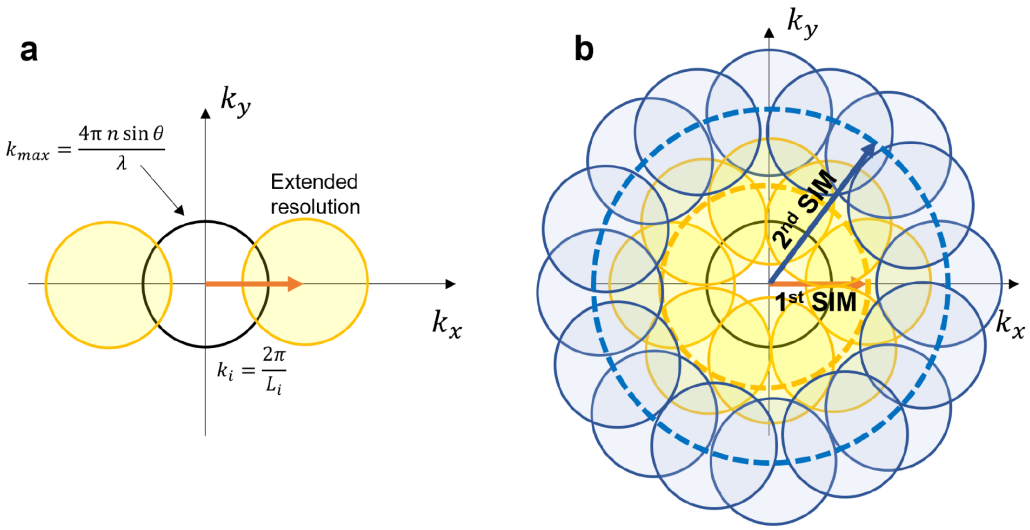

Figure 3.7: (a) Representation of conventional SIM in the Fourier plane corresponding to the sample surface identified by the xy plane in the real space. The black circle depicts the maximum spatial frequency resolvable with an optical microscope, *i.e.* the minimum dimension of a feature that can be observed. The yellow circles represent the spatial frequencies accessible with a structured illumination with a characteristic spatial frequency of k_i, with $k_i \sim k_{max}$ when visible light is employed. (b) The use of EUV radiation in SIM allows to significantly increase the resolution ($k_i^{EUV} > k_i^{Vis}$) as well as to perform a scan of the $k_x k_y$ plane to obtain a comprehensive 2D reconstruction of the investigated feature. Image reproduced from [152].

patterns, standard SIM enables the retrieval of sample structures with a resolution that surpasses the Abbe limit by approximately twofold [151].

A study that laid the foundations for extending SIM in the X-rays regime was firstly performed by Günther et al. [153], where they performed transmission SIM relying on the Talbot-carpet effect [154] and using 35 keV synchrotron radiation from PETRA III at DESY. In the investigation presented here, we employed the ultrashort EUV pulses produced by the FERMI FEL to examine the plausibility of implementing SIM using such kind of pulses, expanding the potential of this technique not just beyond visible light, but as well exploring the time domain. EUV radiation was shined onto a scintillator crystal, *i.e.* a 20µm thick flake of Cerium-doped Yttrium Aluminum Garnet (YAG) crystal, which is a well-known scintillator, that emits via fluorescence at around 550 nm when irradiated with EUV light. The setup that can perform the experiment without the momentum constraints usually associated with standard SIM microscopy is the TIMER beamline, which routinely produce a patterned illumination spot via the superposition of two EUV beam with a periodicity L_s of tens of nm, with the possibility of finely tuning k_i down to the nm^{-1} range, preserving the overlap in the $k_x k_y$ plane (see Fig. 3.7 b). A sub 100 nm pitch of the illuminating spot is the first requirement to further push the limit of SIM beyond Abbe's limit, While the other ingredient is a spatial frequency in the sample L_i such that $L_s \sim L_i$.

The goal of this work is that of proving that SIM could be performed with EUV radiation ultrashort pulses at the TIMER beamline, *i.e.* observing the presence of moiré fringes in the visible. Although, the full reconstruction of the image and actual time resolved measurements will be the object of future experiments.

3.2.2 Methods

In this experiment the TIMER setup (see Sec. 1.6.5) was equipped with an additional fluorescence microscope with a nominal resolution $d = 0.37\mu$m (Zeiss Epiplan 50x, NA = 0.7, infinity corrected, located in the vacuum chamber). The microscope has the capability to transfer images of the scintillator fluorescence from a single shot EUV pulse. The objective used to collect the fluorescence was mounted on a 5 axis mamipulator, that allowed to change its distance from the sample as well as the vertical and horizontal translations in the transversal plane and the two rotations around these axis. Outside the vacuum chamber, a lens was positioned to focus the emitted photons on the detector, a ORCA sCMOS camera from Hamamatsu. A sketch of the setup is depicted in Fig. 3.8. The illuminating patterned was generated with the TIMER standard configuration with a semi-angle between the beams $\theta = 9.1°$. The FEL wavelength was varied in order to change the pitch of the patterned spot according to the fundamental TG equation 1.6.3.

The static sinusoidal pattern imprinted on the sample was obtained by photo damaging at $\lambda = 83.2$ nm with an FEL fluence of $\approx 1 mJcm^{-2}$ to get a periodicity $L_s = 263$ nm. The structured illumination was performed with the same geometry ($\theta = 9.1°$), at $\lambda = 86.6$ nm with a lower fluence $\approx 0.08 mJcm^{-2}$, generating a grating with pitch $L_s = 273$ nm.

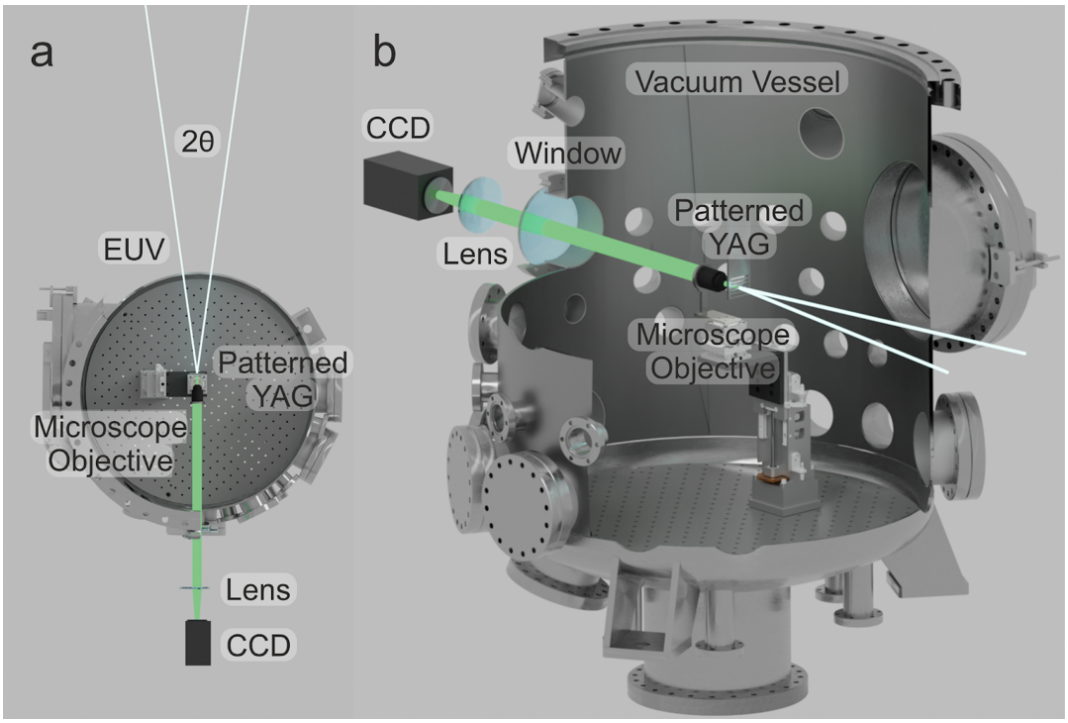

Figure 3.8: (a) Top view of the experimental chamber. The white lines sketch the two EUV beams crossing onto the patterned YAG screen with a semi-angle $\theta = 9°$. The thick green line represent the fluorescence light ($\lambda_{max} = 550$ nm), which is collected by the oblective and directed outside the vacuum chamber to a lens, which in turn focus it on the CCD camera. (b) Side view of the experimental setup. Image reproduced from [152].

3.2.3 Results

Moiré patterns can display different degrees of complexity. The simplest scenario is that of sinusoidally modulated fringes and in this experiment we forced such kind of pattern on the scintillator

crystal by "printing" a grating with intense FEL pulses; the geometry of the TIMER beamline with two EUV pump branches for TG experiments was exploited to locally damage the sample with a controlled spatial periodicity, *i.e.* L_s, by setting the intensity of the pulses above the damage threshold of the material [155–157]. The advantage of this approach is that by sacrificing a small part of the sample, several moiré patterns with different periodicity could be fabricated in situ thanks to fine wavelength tunability of FERMI. Such structure could then be illuminated with a low intensity structured beam with periodicity L_i that slightly differs from L_s. With the strategy described above, the pattern periodicity of the resulting fluorescence of the scintillator L_M will be in the µm range and, hence, directly observable with a visible microscope.

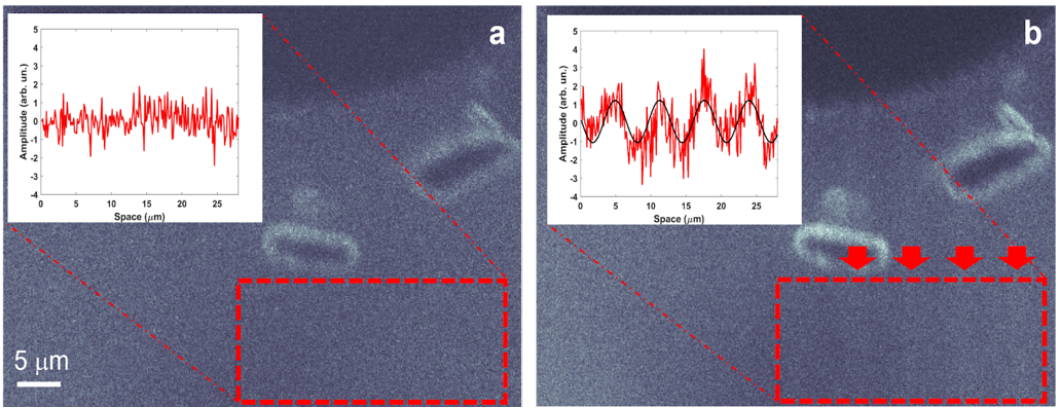

Figure 3.9: (a) Patterned YAG illuminated with a single homogeneous EUV beam (unstructured illumination). The inset depicts the vertical projection of the region enclosed within the red rectangle, following the removal of a background with a linear variation. (b) Same Patterned YAG illuminated with two overlapped EUV beams (structured illumination). The presence of the moiré fringes is evident in the projection in the inset, which has been fitted with a sinusoidal function. Image reproduced from [152].

We utilized a fluence of 1 mJ·cm^{-2} at a wavelength of 83.2 nm to create a spatial modulation of the fluorescence efficiency with a grating pitch L_s of 263 nm. The fluorescence emitted by the YAG crystal was captured using an objective lens with a theoretical resolution of d = 0.37 m.

The periodicity of the modulated fluorescence falls below the resolution limit of our microscope ($d = 0.37$µm), making it indistinguishable. In Fig. 3.9a, the detected image illustrates the structured sample, *i.e.* the photodamaged portion of the sample, illuminated from a single, uniform EUV beam. As expected, no modulation has been observed in this case ($L_s = 263$ nm $\ll d$). In Fig. 3.9b, the illumination is provided by a structured EUV beam, specifically an EUV TG with $L_i = 274$ nm, achieved by setting the wavelength to 86.6 nm. In this case a modulation of the fluorescence is induced by the structured illumination beam and a micrometric moiré pattern is observed with the microscope. Both images represent a single FEL shot, with the EUV flux at the sample position approximately 0.08 mJ·cm^{-2}.

Since both the modulation of the sample's fluorescence efficiency and the structured EUV beam follow sinusoidal patterns, the resulting moiré pattern is also expected to be sinusoidal. The predicted fringe spacing, denoted as LM, is estimated to be 6.6 μm, which comfortably falls within the resolution capabilities of our microscope ($L_M > d$). In Fig. 3.9, the red hatched areas highlight the presence of these fringes. To enhance visibility, red arrows in Fig. 3.9b indicate the fringe location.

The insets in Fig. 3.9 show the vertical projection of the areas enclosed by the red boxes, after

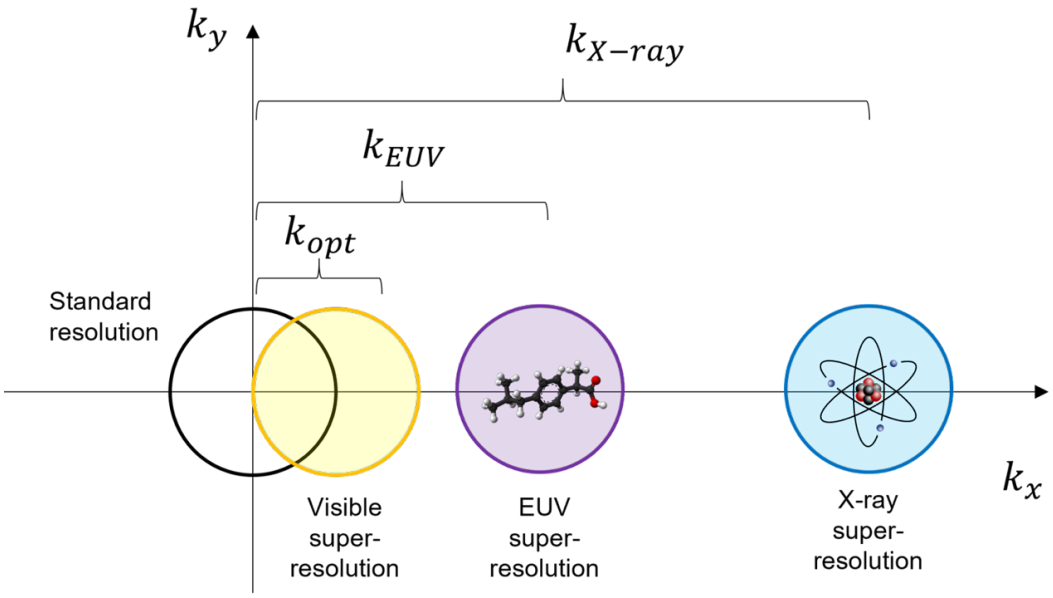

Figure 3.10: Illustration of the capabilities of SIM in terms of transferable spatial frequency. TIMER could in principle access spatial frequencies of the sample in the order of the dimensions of large molecules ($k_s \approx 0.1 - 1$ nm^{-1}), while X-ray interferometers could generate structured beams with ($k_i > 1$nm^{-1}), potentially allowing to imaging atoms. Image reproduced from [152].

subtracting a linearly varying background. The projection corresponding to Figure 2a exhibits a flat and noisy profile, with a peak-to-peak amplitude of approximately 2 counts per pixel. In contrast, in the inset of Fig. 3.9b (black line), an additional modulation of 2 counts per pixel with a spacing of 6.3 $\pm$ 0.1 μm, determined through a sinusoidal fit, becomes apparent. This measured spacing closely aligns with the expected spacing mentioned earlier, with any minor discrepancy likely attributable to a slight calibration error in the pixel-to-meter conversion.

A comprehensive SIM image reconstruction process requires the rotation of the sample with respect to the axis of the illuminating structured spot for sampling the reciprocal k_{xy} plane with the extended resolution circles. In such process, maintaining the overlap between consecutive circles centered at different (k_x,k_y) coordinates is key in order to gain additional information on and adjust the contrast of images with different spatial frequencies, similarly to the composition of a puzzle, where the single pieces need to be placed in the right spot to overlap and form a clear picture. This is because the overlap is employed to fit the parameters used for locating new details into the parent structure (improving lateral resolution) and obtaining a good quality image [149]. In this regard, the FERMI FEL is an optimal source, because its fine tunability of photon energy permit to scan different regions of the k_x axis, varying the position and the size of the resolution circles.

3.2.4 Conclusions

In the particular case of this study, the sample only possess a 1D structure, *i.e.* the printed grating, with a single associated spatial frequency k_s, therefore rotation is not needed. The current capabilities of the TIMER EUV TG setup could allow to perform SIM with a spatial resolution of 10s of nm, but it could be extended to a resolution of just few nm, that would open the possibility of observing large molecules (see Fig. 3.10). Moreover, thanks to ultrashort pulses produced by FERMI, TIMER has the potential of extending the technique in the time domain, which remains so

far unexplored. For future perspectives, the SIM could be pushed even further beyond, using X-Ray photons. Talbot effect with reflection gratings could generate patterned beam with periodicity down to few nm working with photon energies up to ≈ 5 keV [120]. The 1 nm barrier for the structured beam grating periodicity could be defied in principle by using Laue or Bragg interferometers[158], where the resulting pitch is determined by the temperature of the crystals and the diffraction order[159].

The use of X-Rays for imaging exploits X-ray fluorescence, which offers significant uptakes over the visible counterpart, namely:

- chemical selectivity, the emission has a final state which correspond to the filling of a core orbital;

- timescale of the emission process in the fs [160], which set the stage for time-resolved studies.

Therefore, thanks to bright and ultrafast sources such as FEL and HHG that are suitable for X-ray fluorescence applications [161], SIM could actually open the door to the possibility of imaging nanoscale ultrafast dynamics in real-time. Combined with the intrinsic chemical selectivity of X-ray fluorescence, this technique could be of paramount importance in several fields of application, *e.g.* medicine and cultural heritage [162, 163]. Particularly, nanoscale resolution/10s of fs resolution would be greatly beneficial for investigating local dynamics in disordered systems, where diffraction techniques can only probe average structures and related properties, *e.g.* batteries and catalytic surfaces/nanoparticles [164–167].

In summary, we utilized crossed extreme ultraviolet (EUV) pulses to create structured illumination patterns with a periodicity of a few hundred nanometers. By applying this approach, we observed intriguing moiré fringes in a structured sample that possessed a similar pattern but with slightly different periodicity. It's worth noting that our EUV structured illumination microscopy technique allowed us to improve spatial resolution two-fold compared with X-ray microscopy using a single beam from a synchrotron source [153]. Moreover, this breakthrough was accomplished using a pulsed EUV source for the first time.

Looking ahead, the next step in advancing this technique involves employing X-ray beams with even smaller periodicities in the single-digit nm range and beyond. This would enable us to explore not only the static structure but also the dynamic behavior of samples at the atomic level, opening up possibilities that were previously unimaginable.

3.3 Self-diffraction

3.3.1 Introduction

As explained in the previous section, the TIMER beamline is devised to perform non-collinear pump-probe experiments in the EUV regime. The technique presented in this section is inspired by the idea at the roots of coherent stimulated spectroscopies, *i.e.* exploiting the duration of a single coherent pulse to treat it as two photons with the same phase and eventually different arrival time, and by the geometry of non-collinear experiments, such as transient grating. In a nut shell, two EUV pulses with associated wave vectors $\vec{k}_1$ and $\vec{k}_2$ are spatially and temporally overlapped onto the sample. The excitation generated is the same of a conventional TG experiment, which could be visualized as the excitation of coherent wave packets associated with core-hole transitions and, at the same time, as a periodic spatial modulation of the complex refractive index of the sample. The period of such spatial excitation corresponds to the TG pitch. The main difference with respect to conventional TG experiments is the probing, which normally involves the diffraction of a third

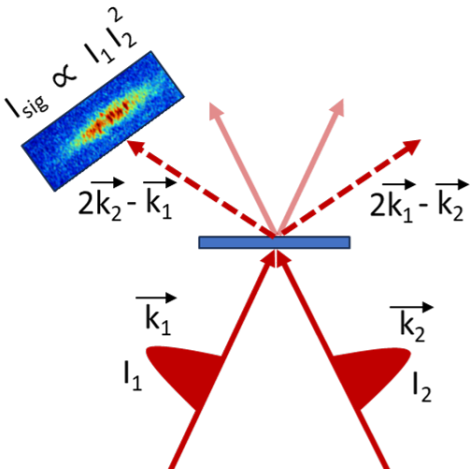

Figure 3.11: Sketch of a self-diffraction experiment.

time delayed beam. In contrast, self-diffraction experiments focus on observing the diffraction of the pump beams themselves as the signal of interest. As a result, a pair of twin signals is generated in the directions given by $2\vec{k}_1$ - $\vec{k}_2$ and $2\vec{k}_2$ - $\vec{k}_1$ (see Fig. 3.11). So in this case, the dynamics of the excitation grating formation within the pulse duration Δt are probed rather than its relaxation.

Furthermore, the capability of accessing information on the excitation pulse has led to the employement of self-diffraction as a diagnostic tool for ultrashort laser pulses. Monitoring the diffraction intensity as a function of the delay between two portions of the original beam[4] allows to determine the coherence time and pulse duration of the original pulse and to carry out so called "two pulse photon-echo" experiments [168–170]. The focus in these works is on the time variable, *i.e.* the delay between the two beams.

Another interesting example of self-diffraction experiments can be found in the work from Rappen et al. [171], where coherent dynamics of continuum states and their interplay with excitons at the direct gap of germanium (T= 1.8 K) is studied with atwo pulse photon-echo approach,*i.e.* a femtosecond four-wave mixing where the delay between the two pump pulses extends beyond the duration of the individual pulses. In the aforementioned work, the dependence of the diffracted signal has been analyzed in terms of both the delay between the generating pulse and the photon energy. This investigation can be regarded as the first step for extending self-diffraction towards core-level spectroscopy. The experiments presented here are focused only on the photon energy dependence of the self-diffraction signal. Phton energies were scanned in the EUV region accross a core-hole resonance of an element present in the sample. Time, in the sense of delay between "pump" and "probe", is not explicitly taken into consideration. Notwithstanding, the experimental configuration shown in Fig. 3.11 takes advantage of the finite length of the beams: the leading portions (heads) of the beams function as pumps, generating the grating, while the trailing portions (tails) are diffracted. In reality, this is an oversimplified picture, since the excitation and the probing processes concurrently occur over the whole duration of the pulses. Photon energies in proximity with resonant excitation allows to generate a FWM signal even at low EUV fluences, which ensures a small cross-section of two-photon absorption. Furthermore, the lifetime of the core-hole states generated by the EUV excitation are probably shorter than the EUV pulse duration,

[4]Within the family of FWM experiments, photon echos are characterized by a delay between the excitation pulses which is longer than the individual pulse duration. Conversely,in self-diffraction the delay between the excitation pulses is shorter than the pulse duration, therefore temporal overlap is granted.

making it reasonable to consider the individual excitation processes instantaneous in the presented experimental framework[5]. Therefore, the probability of probing atoms which possess a core-hole excitation triggered by another EUV photon is negligible compared to the probability of probing unperturbed atoms. In light of this consideration, the main effect of the EUV excitation probed in this experiment could be considered an increase in the average electronic temperature of the system. The outcome of a set of measurements at different photon energies is a core-hole spectrum of the system in a perturbed configuration that can be thought as the difference between the ground state and the material with a given amount of hot electrons. Furthermore, with respect to a linear static absorption spectrum, where a difference in transmission is measured, in the case of self-diffraction the contrast is enhanced because the diffracted signal beam is detected with a non-collinear geometry in a background-free direction.

3.3.2 Co self-diffraction

The first experiment conducted at FERMI with the self-diffraction technique was performed at the TIMER beamline on a Co sample in the photon energy range that encompasses the $M_{2,3}$ absorption edge ($\sim 55 - 70$ eV). The result of the measurement is related to the absorption spectrum, since it displays a peak in correspondence of the Co $M_{2,3}$ absorption edge (see Fig. 3.12 a). The intensity of the self-diffraction signal at 58.95 eV was recorded for several FEL fluences. The plot in Fig. 3.12 b illustrates the trend of the diffracted signal intensity with respect to the FEL fluence. The dashed red line represents the I_0^3 function ($\propto I_1 I_2^2$). The linearity of the experimental points with I_0^3 is a clear evidence of the cubic dependence of the signal intensity on the FEL fluence, as predicted for a FWM process.

Our collaborators from Caltech, Prof. Scott K. Cushing and the PhD candidate Wonseok Lee, have performed some theoretical simulations on for the interpretation of the experimental data (see Fig. **??** a). The calculations rely on the assumption that the electrons thermalize within the duration of the FEL pulses ($\sim 50fs$). Such assumption is probably not realistic (a work from Medvedev et al. reports a value of 400 fs for the electron subsystem thermalization in Al irradiated with EUV radiation [172]), but it is reasonable to think that most likely the larger portion of the electrons are thermalized and even if the process is not fully completed, it does not affect the calculations in a relevant way. Within this approximation, the electronic temperature was estimated to be ≈ 3700 K and the dielectric function has been calculated as a function of the photon energy using the Bethe-Salpeter equation on the base of the band structure, which in turn was calculated with DFT. The complex dielectric function is defined as:

$$\epsilon^* = \epsilon' + i\epsilon'' \tag{3.3}$$

and it is related to the complex refractive n^* index as follows:

$$\epsilon' + i\epsilon'' = (n^*)^2 \qquad \text{with} \qquad n^* = n + i\kappa \tag{3.4}$$

From the calculations, the self-diffraction signal results proportional to :

$$\Delta n^2 + \Delta\kappa^2 = (n_{3700K} - n_{0K})^2 + (\kappa_{3700K} - \kappa_{0K})^2 \tag{3.5}$$

[5]This will depend on the specific element probed and on the pulse duration. Considering the time duration of the FERMI pulses (≥ 50 fs) this assumption is likely reliable.

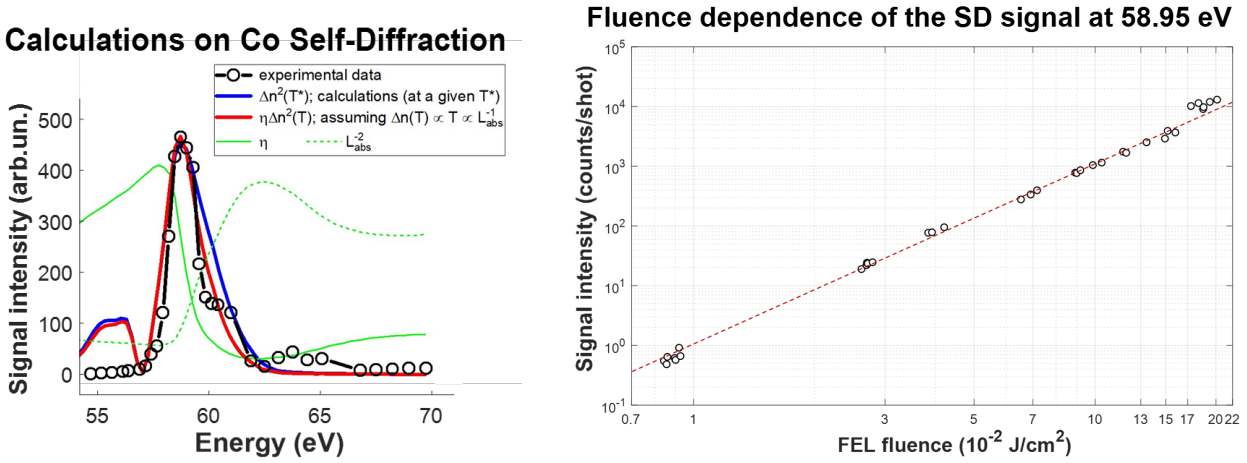

(a) (b)

Figure 3.12: (a) Calculations of the self-diffraction measurements on Co. The black dots represents the experimental data, the blu line is a calculation of the signal intensity as Δn^2 at a given temperature, the red line is a calculation of the signal intensity as $\eta\Delta n^2$, assuming that Δn is proportional to the electronic temperature and inversely proportional to the absorption length (L_{abs}). η is the diffraction efficiency introduced in section 1.6.3, which accounts for the dependence of the diffracted intensity on the absorption length. (b) The intensity of the self-diffraction signal is plotted versus the FEL fluence at 21 nm (58.95 eV). The dashed red line is $\propto I_0^3$. The linearity associated to the cubic dependence is evident, demonstrating the third-order non-linear nature of the signal, as expected for a FWM signal.

At elevated (electronic) temperatures, non-integer occupation numbers are possible according to the Fermi-Dirac statistics and finite temperature can be approximated by modifying the BSE Hamiltonian to include fractional occupation numbers. When modeling temperatures below the melting point, two initial effects can affect the EUV spectra: i) changes in Fermi blocking and ii) changes to the dielectric screening. Only the first effect has been considered in our case.

3.3.3 α-Fe_2O_3 self-diffraction

In a second experiment at the TIMER beamline, we have performed a self-diffraction measurement at the Fe $M_{2,3}$ edge of α-Fe_2O_3 ($\sim 56 - 60$ eV, see Fig.3.13). With this experiment we have demonstrated that this technique is general and that it is not limited to a specific kind of sample as long as the photon energy is resonant with a core-hole transition and that the cross-section of the FWM process is large enough to grant a diffraction efficiency beyond the limit of detectability of the setup. Unfortunately, the experiment was performed recently, so we did not have any calculations at the moment to interpret the experimental data. The signal intensity displayed in Fig. 3.13 was calculated as the difference between the self-diffraction intensity and the background, normalized by I_0^3.

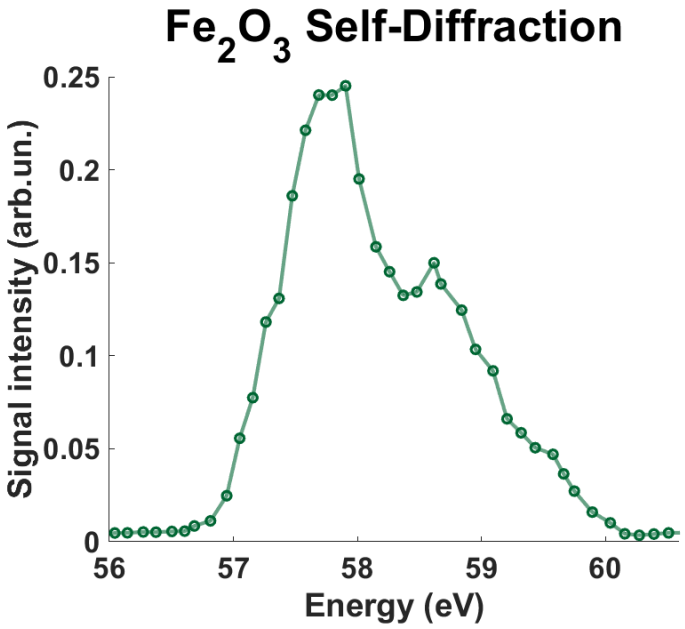

Figure 3.13: Results of the self-diffraction measurement on Fe_2O_3. The diffraction intensity is plotted for a photon energy scan across the $M_{2,3}$ absorption edge of Fe_2O_3.

3.3.4 Conclusion

Spectrally resolved self-diffraction has proven to be an efficient and reliable technique for performing background free core-hole spectroscopy. Although the understanding of the physics at the origin of this kind of signal is just in an initial stage, we have moved the first steps in the exploration of the potential of this FWM technique. The intrinsic chemical selectivity of core-hole transitions associated to the excitation with EUV radiation combined with i) the pulse duration at FERMI (< 100 fs), ii) the non-collinear geometry of the TIMER beamline and iii) the 3^{rd} order non-linear nature of the FWM processes, offers a unique experimental environment that would be ideal to investigate chemical phenomena thanks to the subpicosecond time resolution and the enhancement of the S/N ratio that comes from both the non-collinear geometry and the 3^{rd} order non-linearity. To this regard, a future application of this technique could be that of probing a reversible chemical process[6], *i.e.* self-diffraction could be used as a background-free probe in a pump-probe experiment to monitor chemical dynamics, where the S/N enhancement is a key factor for the success of the investigation, introducing the possibility of performing time-resolved investigations by changing the delay between the two pumps, as in the case of photon-echoes experiments.

[6] that recover in between pump-probe shots

Chapter 4

Conclusions

The focus of the presented thesis is that of exploiting the ultrashort EUV pulses produced by the FERMI FEL as a tool for investigating chemical reactions and chemical processes. The central project reported in chapter 2 is a study of the ultrafast dynamics occurring during the thermite reaction in the hundreds of femtoseconds to hundreds of picoseconds time scale. The redox reaction between α-Fe_2O_3 and Al is a solid-state heterogeneous process and to monitor its evolution the technique of transient EUV absorption spectroscopy has been selected. The robust transient absorption setup at the TIMEX beamline at FERMI is an excellent experimental environment for perfoming measurements using this technique, since it allows to combine a $\sim$ 100 ps time resolution with the intrinsic chemical selectivity of the core-hole transitions probed with EUV pulses. Moreover, the SLU pump, which is delivered into the experimental vacuum chamber, has the capability of depositing a high energy density on the sample, reaching fluences of the order of 0.9 J/cm^2 and enabling to generate conditions of high temperature and high pressure at the sample. The potential of the instrument has been fully exploited to monitor the evolution of the thermite reaction with tr-XAS, showing that the technique is suitable for pursuing such scientific challenge thanks to its sensitivity to variations of the oxidation state and chemical surroundings.

The sample was photothermally excited with the SLU pump at 785 nm and the consequent electron-phonon coupling dynamics were resolved with an heterogeneous time mesh using the pump-probe approach. The FEL radiation was employed as the probe and it was tuned at the Fe $M_{2,3}$ edge and at the Al $L_{2,3}$ edge in two sets of measurements to record single energies pump-probe traces. Transient absorption maps were generated from the pump-probe traces which allowed to observe a blue-shift zero crossing, a spectroscopic feature that is identified as the fingerprint of small-polaron formation in hematite and that suggest two-photon absorption as the dominant photo-excitation mechanism. Furthermore, we have observed a difference in the aforementioned blue-shift comparing α-Fe_2O_3 samples deposited on Al and on parylene. The interpretation of such substrate-dependent variations have been attributed to an electron transfer between Al and α-Fe_2O_3 with the support of theoretical calculations.

Although all the requirements necessary for triggering the reaction were fulfilled, clear evidence of the further proceeding of the process after the elctronectron transfer were not observed.This may be attributed to a lack of contrast in the TA signal, since the reaction occurs at the interface. Moreover, the decrease in density of the volume probed by the FEL and the loss of gaseous species due to the low pressure of the experimental chamber reduce tha probability of reaching the self-sustaining regime.

In the second part of the thesis, some innovative EUV-based techniques developed at the TIMER beamline are illustrated, which combine the intrinsic chemical selectivity of EUV pulses with the

noncollinear geometry of the setup. This enhances the S/N ratio, making these techniques suitable to be applied for investigating ultrafast chemical processes.

The first technique presented is a coherent Raman scattering experiment where upon excitation with two non-degerate EUV pulses, an inelastic FWM signal is generated by the scattering of an optical laser probe. Such technique offer the possibility of generating and probing electronic coherences over different atoms, which represent a unique tool for monitoring electron transfer processes in the context of bond breaking and bond formation in chemical reactions.

The second technique reported is structured illumination microscopy, where the TG setup was used to generate a periodic nanostructure on the sample and consequently to illuminate such pattern with a structured beam of slightly different periodicity. The approach consists in combining objects with different spatial frequencies, *i.e.* the structured illuminating beam and the nanostructured grating imprinted on the sample, in order to generate a moiré pattern with a consistently larger resulting spatial frequency. The interference pattern could be directly imaged with an optical microscope, as opposed to the nanostructure imprinted on the sample. Therefore, after processing the image, it is possible to access features that would not be resolvable by the microscope. The potential of this technique is that of paving the way to imaging ultrafast dynamics in real time with an unprecedented spatial resolution.

The last experiment presented involves spectrally resolved EUV self-diffraction, a fast and reliable technique to perform background-free core-hole spectroscopy with the use of two EUV pulses. The enhancement of the S/N ratio would make this technique an interesting chemically selective probe for reversible chemical processes.

Bibliography

1. HW Koch and JW Motz. Bremsstrahlung cross-section formulas and related data. *Reviews of modern physics*, 31(4):920, 1959.

2. Settimio Mobilio, Federico Boscherini, and Carlo Meneghini. *Synchrotron Radiation*. Springer, 2016.

3. Katharina C Cramer and Katharina C Cramer. History and science of research with synchrotron radiation. *A Political History of Big Science: The Other Europe*, pages 59–77, 2020.

4. David J Griffiths. *Introduction to electrodynamics*. American Association of Physics Teachers, 2005.

5. Arman Tursunov, Zdeněk Stuchlík, Martin Kološ, Naresh Dadhich, and Bobomurat Ahmedov. Supermassive black holes as possible sources of ultrahigh-energy cosmic rays. *The Astrophysical Journal*, 895(1):14, 2020.

6. AJ Dean, DJ Clark, JB Stephen, VA McBride, L Bassani, A Bazzano, AJ Bird, AB Hill, SE Shaw, and P Ubertini. Polarized gamma-ray emission from the crab. *Science*, 321(5893):1183–1185, 2008.

7. Ulrich Klein and Andrew Fletcher. *Galactic and intergalactic magnetic fields*. Springer, 2014.

8. FR Elder, AM Gurewitsch, RV Langmuir, and HC Pollock. Radiation from electrons in a synchrotron. *Physical Review*, 71(11):829, 1947.

9. R Bonifacio, F Casagrande, G Cerchioni, L de Salvo Souza, P Pierini, and N Piovella. Physics of the high-gain fel and superradiance. *La Rivista del Nuovo Cimento (1978-1999)*, 13:1–69, 1990.

10. James A Clarke. *The science and technology of undulators and wigglers*, volume 4. OUP Oxford, 2004.

11. Peter Schmüser, Martin Dohlus, Jörg Rossbach, and Christopher Behrens. *Free-electron lasers in the ultraviolet and X-ray regime*, volume 258. Springer, 2014.

12. J MJ Madey. Relationship between mean radiated energy, mean squared radiated energy and spontaneous power-spectrum in a power series expansion of the equations of motion in a free-electron laser. *Nuovo Cim., B;(Italy)*, 50(1), 1979.

13. AM Kondratenko and EL Saldin. Generating of coherent radiation by a relativistic electron beam in an ondulator. *Part. Accel.*, 10:207–216, 1980.

14. R Bonifacio, C Pellegrini, and LM Narducci. Collective instabilities and high-gain regime free electron laser. *AIP conference proceedings*, 118(1):236–259, 1984.

15. Paul Emma, R Akre, J Arthur, R Bionta, C Bostedt, J Bozek, A Brachmann, P Bucksbaum, Ryan Coffee, F-J Decker, et al. First lasing and operation of an ångstrom-wavelength free-electron laser. *nature photonics*, 4(9):641–647, 2010.

16. Bo Liu, Chao Feng, Duan Gu, Fei Gao, Haixiao Deng, Meng Zhang, Sen Sun, Si Chen, Wei Zhang, Wencheng Fang, et al. The sxfel upgrade: from test facility to user facility. *Applied Sciences*, 12(1):176, 2022.

17. M Altarelli. The european x-ray free-electron laser facility in hamburg. *Nuclear Instruments and Methods in Physics Research Section B: Beam Interactions with Materials and Atoms*, 269(24):2845–2849, 2011.

18. In Soo Ko, Heung-Sik Kang, Hoon Heo, Changbum Kim, Gyujin Kim, Chang-Ki Min, Haeryong Yang, Soung Youl Baek, Hyo-Jin Choi, Geonyeong Mun, et al. Construction and commissioning of pal-xfel facility. *Applied Sciences*, 7(5):479, 2017.

19. J Amann, W Berg, V Blank, F-J Decker, Y Ding, P Emma, Y Feng, J Frisch, D Fritz, J Hastings, et al. Demonstration of self-seeding in a hard-x-ray free-electron laser. *Nature photonics*, 6(10):693–698, 2012.

20. S Reiche et al. Overview of seeding methods for fels. *Proc. IPAC*, pages 2063–2067, 2013.

21. G Lambert, T Hara, D Garzella, T Tanikawa, M Labat, B Carre, H Kitamura, T Shintake, M Bougeard, S Inoue, et al. Injection of harmonics generated in gas in a free-electron laser providing intense and coherent extreme-ultraviolet light. *Nature physics*, 4(4):296–300, 2008.

22. Tadashi Togashi, Eiji J Takahashi, Katsumi Midorikawa, Makoto Aoyama, Koichi Yamakawa, Takahiro Sato, Atsushi Iwasaki, Shigeki Owada, Tomoya Okino, Kaoru Yamanouchi, et al. Extreme ultraviolet free electron laser seeded with high-order harmonic of ti: sapphire laser. *Optics Express*, 19(1):317–324, 2011.

23. DJ Dunning, BWJ McNeil, and NR Thompson. Short wavelength regenerative amplifier free electron lasers. *Nuclear Instruments and Methods in Physics Research Section A: Accelerators, Spectrometers, Detectors and Associated Equipment*, 593(1-2):116–119, 2008.

24. Li Hua Yu, L DiMauro, A Doyuran, WS Graves, ED Johnson, R Heese, S Krinsky, H Loos, JB Murphy, G Rakowsky, et al. First ultraviolet high-gain harmonic-generation free-electron laser. *Physical review letters*, 91(7):074801, 2003.

25. E Allaria, Roberto Appio, L Badano, WA Barletta, S Bassanese, SG Biedron, A Borga, E Busetto, D Castronovo, P Cinquegrana, et al. Highly coherent and stable pulses from the fermi seeded free-electron laser in the extreme ultraviolet. *Nature Photonics*, 6(10):699–704, 2012.

26. E Allaria, D Castronovo, P Cinquegrana, P Craievich, Massimo Dal Forno, MB Danailov, G D'Auria, A Demidovich, G De Ninno, S Di Mitri, et al. Two-stage seeded soft-x-ray free-electron laser. *Nature Photonics*, 7(11):913–918, 2013.

27. Gennady Stupakov. Using the beam-echo effect for generation of short-wavelength radiation. *Physical review letters*, 102(7):074801, 2009.

28. Dao Xiang and Gennady Stupakov. Echo-enabled harmonic generation free electron laser. *Physical Review Special Topics-Accelerators and Beams*, 12(3):030702, 2009.

29. D Xiang, E Colby, M Dunning, S Gilevich, C Hast, K Jobe, D McCormick, J Nelson, TO Raubenheimer, K Soong, et al. Demonstration of the echo-enabled harmonic generation technique for short-wavelength seeded free electron lasers. *Physical review letters*, 105(11):114801, 2010.

30. Primož Rebernik Ribič, Alessandro Abrami, Laura Badano, Maurizio Bossi, Hans-Heinrich Braun, Niky Bruchon, Flavio Capotondi, Davide Castronovo, Marco Cautero, Paolo Cinquegrana, et al. Coherent soft x-ray pulses from an echo-enabled harmonic generation free-electron laser. *Nature Photonics*, 13(8):555–561, 2019.

31. L-H Yu, M Babzien, I Ben-Zvi, LF DiMauro, A Doyuran, W Graves, E Johnson, S Krinsky, R Malone, I Pogorelsky, et al. High-gain harmonic-generation free-electron laser. *Science*, 289(5481):932–934, 2000.

32. Toru Hara. Fully coherent soft x-rays at fermi. *Nature Photonics*, 7(11):852–854, 2013.

33. Ilan Ben-Zvi, KM Yang, and LH Yu. The fresh-bunch technique in fels. *Nuclear Instruments and Methods in Physics Research Section A: Accelerators, Spectrometers, Detectors and Associated Equipment*, 318(1-3):726–729, 1992.

34. CJ Bocchetta et al. Conceptual design report for the fermi@ elettra project. *Sincrotrone trieste*, 2007.

35. P Cinquegrana, A Demidovich, G Kurdi, I Nikolov, P Sigalotti, P Susnjar, and MB Danailov. The seed laser system of the fermi free-electron laser: design, performance and near future upgrades. *High Power Laser Science and Engineering*, 9:e61, 2021.

36. Fabio Benatti, Stefano Olivares, Giovanni Perosa, Daniele Bajoni, Simone Di Mitri, Roberto Floreanini, Ludovico Ratti, and Fulvio Parmigiani. Quantum state features of the fel radiation from the occupation number statistics. *Optics Express*, 29(24):40374–40396, 2021.

37. P Cinquegrana, S Cleva, A Demidovich, G Gaio, R Ivanov, G Kurdi, I Nikolov, P Sigalotti, and MB Danailov. Optical beam transport to a remote location for low jitter pump-probe experiments with a free electron laser. *Physical Review Special Topics-Accelerators and Beams*, 17(4):040702, 2014.

38. Miltcho B Danailov, Filippo Bencivenga, Flavio Capotondi, Francesco Casolari, Paolo Cinquegrana, Alexander Demidovich, Erika Giangrisostomi, Maya P Kiskinova, Gabor Kurdi, Michele Manfredda, et al. Towards jitter-free pump-probe measurements at seeded free electron laser facilities. *Optics express*, 22(11):12869–12879, 2014.

39. Cristian Svetina, Daniele Cocco, Nicola Mahne, Lorenzo Raimondi, Eugenio Ferrari, and Marco Zangrando. Presto, the on-line photon energy spectrometer at fermi: design, features and commissioning results. *Journal of Synchrotron Radiation*, 23(1):35–42, 2016.

40. Alberto Simoncig, Michele Manfredda, Giulio Gaio, Nicola Mahne, Lorenzo Raimondi, Claudio Fava, Simone Gerusina, Riccardo Gobessi, Alessandro Abrami, Flavio Capotondi, et al. Ac/dc: The fermi fel split and delay optical device for ultrafast x-ray science. *Photonics*, 9(5):314, 2022.

41. Andrew M Weiner. *Ultrafast optics*. John Wiley & Sons, 2011.

42. Shaul Mukamel. *Principles of nonlinear optical spectroscopy*. Oxford University Press, 1995.

43. F Bencivenga, F Capotondi, L Foglia, R Mincigrucci, and C Masciovecchio. Extreme ultraviolet transient gratings. *Advances in Physics: X*, 8(1):2220363, 2023.

44. Tina Jingyan Miao and Junwang Tang. Characterization of charge carrier behavior in photocatalysis using transient absorption spectroscopy. *The Journal of Chemical Physics*, 152(19), 2020.

45. Daniel Fersch, Pavel Malý, Jessica Rühe, Victor Lisinetskii, Matthias Hensen, Frank Würthner, and Tobias Brixner. Single-molecule ultrafast fluorescence-detected pump-probe microscopy. *The Journal of Physical Chemistry Letters*, 14:4923–4932, 2023.

46. Saifollah Rasouli and Mahnaz Ghorbani. Nonlinear refractive index measuring using a double-grating interferometer in pump-probe configuration and fourier transform analysis. *Journal of Optics*, 14(3):035–203, 2012.

47. GT Purves, G Jundt, CS Adams, and IG Hughes. Refractive index measurements by probe-beam deflection. *The European Physical Journal D-Atomic, Molecular, Optical and Plasma Physics*, 29(3):433–436, 2004.

48. BV Semak and OS Vasyutinskii. Linear dichroism and birefringence of probe radiation in pump-probe spectroscopy of polyatomic molecules. *Optics and Spectroscopy*, 129(9):1007–1017, 2021.

49. R. Mincigrucci, A. Cannizzo, F. Capotondi, P. Cinquegrana, R. Cucini, F. Dallari, M. B. Danailov, G. De Ninno, S. Di Mitri, T. Feurer, L. Foglia, H.-M. Frei, M. Manfredda, A. A. Maznev, G. Monaco, D. Naumenko, I. Nikolov, Z. Ollmann, E. Paltanin, G. Pamfilidis, E. Pedersoli, E. Principi, J. Rehault, A. Simoncig, C. Svetina, G. Knopp, C. Masciovecchio, and F. Bencivenga. Noncollinear, inelastic four-wave mixing in the extreme ultraviolet. *Optica*, 10(10):1383–1388, Oct 2023.

50. Yong-Xin Yan, Edward B Gamble Jr, and Keith A Nelson. Impulsive stimulated scattering: General importance in femtosecond laser pulse interactions with matter, and spectroscopic applications. *The Journal of chemical physics*, 83(11):5391–5399, 1985.

51. Yu-Ming Chang, Li Xu, and Harry WK Tom. Coherent phonon spectroscopy of gaas surfaces using time-resolved second-harmonic generation. *Chemical Physics*, 251(1-3):283–308, 2000.

52. Matthew Walbran, Alexander Gliserin, Kwangyun Jung, Jungwon Kim, and Peter Baum. 5-femtosecond laser-electron synchronization for pump-probe crystallography and diffraction. *Physical Review Applied*, 4(4):044–013, 2015.

53. Lin X Chen. X-ray transient absorption spectroscopy. *X-Ray Absorption and X-Ray Emission Spectroscopy: Theory and Applications*, pages 213–249, 2016.

54. Marcos Dantus, Mark J Rosker, and Ahmed H Zewail. Real-time femtosecond probing of "transition states" in chemical reactions. *The Journal of Chemical Physics*, 87:2395–2397, 1987.

55. Melanie Saes, Christian Bressler, Rafael Abela, Daniel Grolimund, Steven L Johnson, Philip A Heimann, and Majed Chergui. Observing photochemical transients by ultrafast x-ray absorption spectroscopy. *Physical Review Letters*, 90(4):047403, 2003.

56. Keith A Nelson and MD Fayer. Laser induced phonons: A probe of intermolecular interactions in molecular solids. *The Journal of Chemical Physics*, 72(9):5202–5218, 1980.

57. Hans Joachim Eichler, Peter Günter, and Dieter W Pohl. *Laser-induced dynamic gratings*, volume 50. Springer, 2013.

58. L Foglia, R Mincigrucci, AA Maznev, G Baldi, F Capotondi, F Caporaletti, R Comin, D De Angelis, RA Duncan, D Fainozzi, et al. Extreme ultraviolet transient gratings: A tool for nanoscale photoacoustics. *Photoacoustics*, 29:100453, 2023.

59. David T Attwood. *Soft x-rays and extreme ultraviolet radiation, David T. Attwood*. Cambridge University Press, 1999.

60. Andrea Di Cicco, Francesco d'Amico, Goran Zgrablic, Emiliano Principi, Roberto Gunnella, Filippo Bencivenga, Cristian Svetina, Claudio Masciovecchio, Fulvio Parmigiani, and Adriano Filipponi. Probing phase transitions under extreme conditions by ultrafast techniques: Advances at the fermi@ elettra free-electron-laser facility. *Journal of non-crystalline solids*, 357(14):2641–2647, 2011.

61. Andrea Di Cicco, Filippo Bencivenga, Andrea Battistoni, Daniele Cocco, Riccardo Cucini, Francesco D'Amico, Silvia Di Fonzo, Adriano Filipponi, Alessandro Gessini, Erika Giangrisostomi, et al. Probing matter under extreme conditions at fermi@ elettra: the timex beamline. In *Damage to VUV, EUV, and X-ray Optics III*, volume 8077, pages 18–27. SPIE, 2011.

62. C Svetina, G Sostero, R Sergo, R Borghes, C Callegari, F D'Amico, F Bencivenga, C Masciovecchio, A Di Cicco, and D Cocco. A beam-shaping system for timex beamline. *Nuclear Instruments and Methods in Physics Research Section A: Accelerators, Spectrometers, Detectors and Associated Equipment*, 635(1):S12–S15, 2011.

63. Claudio Masciovecchio, Andrea Battistoni, Erika Giangrisostomi, Filippo Bencivenga, Emiliano Principi, Riccardo Mincigrucci, Riccardo Cucini, Alessandro Gessini, Francesco D'Amico, Roberto Borghes, et al. Eis: the scattering beamline at fermi. *Journal of synchrotron radiation*, 22(3):553–564, 2015.

64. Emiliano Principi, Cristian Svetina, Dario De Angelis, Claudio Fava, Riccardo Mincigrucci, Laura Foglia, Alberto Simoncig, Michele Manfredda, Nicola Mahne, Riccardo Gobessi, Martin Scarcia, Alessandro Gessini, Filippo Bencivenga, Flavio Capotondi, Marco Zangrando, and Claudio Masciovecchio. A versatile wide energy range spectrometer for soft x-rays fels [submitted]. *Nuclear Instruments and Methods in Physics Research Section A: Accelerators, Spectrometers, Detectors and Associated Equipment*, 2023.

65. E Principi, E Giangrisostomi, R Mincigrucci, M Beye, G Kurdi, R Cucini, A Gessini, F Bencivenga, and C Masciovecchio. Extreme ultraviolet probing of nonequilibrium dynamics in high energy density germanium. *Physical Review B*, 97(17):174107, 2018.

66. E Principi, S Krylow, ME Garcia, A Simoncig, L Foglia, R Mincigrucci, G Kurdi, A Gessini, F Bencivenga, A Giglia, et al. Atomic and electronic structure of solid-density liquid carbon. *Physical Review Letters*, 125(15):155703, 2020.

67. Jacopo Stefano Pelli Cresi, Emiliano Principi, Eleonora Spurio, Daniele Catone, Patrick O'Keeffe, Stefano Turchini, Stefania Benedetti, Avinash Vikatakavi, Sergio D'Addato, Riccardo Mincigrucci, et al. Ultrafast dynamics of plasmon-mediated charge transfer in ag@ ceo2 studied by free electron laser time-resolved x-ray absorption spectroscopy. *Nano Letters*, 21(4):1729–1734, 2021.

68. R Mincigrucci, JR Rouxel, B Rossi, E Principi, C Bottari, S Catalini, JS Pelli-Cresi, D Fainozzi, L Foglia, A Simoncig, et al. Element-and enantiomer-selective visualization of molecular motion in real-time. *Nature communications*, 14(1):386, 2023.

69. Carino Ferrante, Emiliano Principi, Andrea Marini, Giovanni Batignani, Giuseppe Fumero, Alessandra Virga, Laura Foglia, Riccardo Mincigrucci, Alberto Simoncig, Carlo Spezzani, et al. Non-linear self-driven spectral tuning of extreme ultraviolet femtosecond pulses in monoatomic materials. *Light: Science & Applications*, 10(1):92, 2021.

70. Craig P Schwartz, Sumana L Raj, Sasawat Jamnuch, Chris J Hull, Paolo Miotti, Royce K Lam, Dennis Nordlund, Can B Uzundal, Chaitanya Das Pemmaraju, Riccardo Mincigrucci, et al. Angstrom-resolved interfacial structure in buried organic-inorganic junctions. *Physical review letters*, 127(9):096801, 2021.

71. Lars Hoffmann, Sasawat Jamnuch, Craig P Schwartz, Tobias Helk, Sumana L Raj, Hikaru Mizuno, Riccardo Mincigrucci, Laura Foglia, Emiliano Principi, Richard J Saykally, et al. Saturable absorption of free-electron laser radiation by graphite near the carbon k-edge. *The journal of physical chemistry letters*, 13(39):8963–8970, 2022.

72. Eric Beaurepaire, J-C Merle, A Daunois, and J-Y Bigot. Ultrafast spin dynamics in ferromagnetic nickel. *Physical review letters*, 76(22):4250, 1996.

73. Sonja R Tauchert, Mikhail Volkov, Dominik Ehberger, D Kazenwadel, Martin Evers, Hannah Lange, Andreas Donges, Alexander Book, W Kreuzpaintner, U Nowak, et al. Polarized phonons carry angular momentum in ultrafast demagnetization. *Nature*, 602(7895):73–77, 2022.

74. Claudiu D Stanciu, Fredrik Hansteen, Alexey V Kimel, Andrei Kirilyuk, Arata Tsukamoto, Achioshi Itoh, and Th Rasing. All-optical magnetic recording with circularly polarized light. *Physical review letters*, 99(4):047601, 2007.

75. Dennis Rudolf, Chan La-O-Vorakiat, Marco Battiato, Roman Adam, Justin M Shaw, Emrah Turgut, Pablo Maldonado, Stefan Mathias, Patrik Grychtol, Hans T Nembach, et al. Ultrafast magnetization enhancement in metallic multilayers driven by superdiffusive spin current. *Nature communications*, 3(1):1037, 2012.

76. Filippo Bencivenga, R Mincigrucci, F Capotondi, L Foglia, D Naumenko, AA Maznev, E Pedersoli, A Simoncig, F Caporaletti, Vazrik Chiloyan, et al. Nanoscale transient gratings excited and probed by extreme ultraviolet femtosecond pulses. *Science advances*, 5(7):eaaw5805, 2019.

77. H Goldschmidt. New thermite reactions. *Iron age*, 82:232, 1908.

78. Roberto Orru and Giacomo Cao. On the exploitation of self-propagating high-temperature reactions for environmental protection. *Current Environmental Issues and Challenges*, pages 169–182, 2014.

79. Marke Kallio, Pekka Ruuskanen, J Mäki, E Pöyliö, and S Lähteenmäki. Use of the aluminothermic reaction in the treatment of steel industry by-products. *Journal of Materials Synthesis and Processing*, 8:87–92, 2000.

80. LL Wang, ZA Munir, and YM Maximov. Thermite reactions: their utilization in the synthesis and processing of materials. *Journal of Materials Science*, 28:3693–3708, 1993.

81. Sh H Fischer and MC Grubelich. Theoretical energy release of thermites, intermetallics, and combustible metals. Technical report, Sandia National Lab.(SNL-NM), Albuquerque, NM (United States), 1998.

82. Mehdi Bahrami, Guillaume Taton, Véronique Conédéra, Ludovic Salvagnac, Christophe Tenailleau, Pierre Alphonse, and Carole Rossi. Magnetron sputtered al-cuo nanolaminates: effect of stoichiometry and layers thickness on energy release and burning rate. *Propellants, Explosives, Pyrotechnics*, 39(3):365–373, 2014.

83. R Ross Nellums, Steven F Son, and Lori J Groven. Preparation and characterization of aqueous nanothermite inks for direct deposition on scb initiators. *Propellants, Explosives, Pyrotechnics*, 39(3):463–470, 2014.

84. Eric J Faierson, Kathryn V Logan, Brian K Stewart, and Michael P Hunt. Demonstration of concept for fabrication of lunar physical assets utilizing lunar regolith simulant and a geothermite reaction. *Acta Astronautica*, 67(1-2):38–45, 2010.

85. Gianluca Corrias, Roberta Licheri, Roberto Orrù, and Giacomo Cao. Optimization of the self-propagating high-temperature process for the fabrication in situ of lunar construction materials. *Chemical engineering journal*, 193:410–421, 2012.

86. Francisco Alvarez, Christopher White, Ashvin Kumar Narayana Swamy, and Evgeny Shafirovich. Combustion wave propagation in mixtures of jsc-1a lunar regolith simulant with magnesium. *Proceedings of the Combustion Institute*, 34(2):2245–2252, 2013.

87. Michelle L Pantoya and John J Granier. Combustion behavior of highly energetic thermites: Nano versus micron composites. *Propellants, Explosives, Pyrotechnics: An International Journal Dealing with Scientific and Technological Aspects of Energetic Materials*, 30(1):53–62, 2005.

88. Luísa Durães, Benilde F.O. Costa, Regina Santos, António Correia, José Campos, and António Portugal. Fe_2O_3/aluminum thermite reaction intermediate and final products characterization. *Materials Science and Engineering: A*, 465(1-2):199–210, 2007.

89. Yi Wang, X.L. Song, Wei Jiang, G.D. Deng, X. De Guo, H.Y. Liu, and F.S. Li. Mechanism for thermite reactions of aluminum/iron-oxide nanocomposites based on residue analysis. *Trans. Nonferrous Met. Soc. China*, 24(1):263–270, 2014.

90. Melissa L. Mileham, Michael P. Kramer, and A.E. Stiegman. Laser initiation processes in thermite energetic materials using laser desorption ionization time-of-flight mass spectrometry. *The Journal of Physical Chemistry C*, 111(45):16883–16888, 2007.

91. Albert E. Stiegman, Chi-Dong Park, Melissa Mileham, Lambertus J. Van de Burgt, and Michael P. Kramer. Dynamics of Al/Fe_2O_3 mic combustion from short single-pulse photothermal initiation and time-resolved spectroscopy. *Propellants, Explosives, Pyrotechnics:*

An International Journal Dealing with Scientific and Technological Aspects of Energetic Materials, 34(4):293–296, 2009.

92. John J. Granier and Michelle L. Pantoya. Laser ignition of nanocomposite thermites. *Combustion and Flame*, 138(4):373–383, 2004.

93. Josh Vura-Weis, Chang-Ming Jiang, Chong Liu, Hanwei Gao, J. Matthew Lucas, Frank M.F. De Groot, Peidong Yang, A. Paul Alivisatos, and Stephen R. Leone. Femtosecond M2, 3-edge spectroscopy of transition-metal oxides: photoinduced oxidation state change in $\alpha-Fe_2O_3$. *The Journal of Physical Chemistry Letters*, 4(21):3667–3671, 2013.

94. Lucas M. Carneiro, Scott K. Cushing, Chong Liu, Yude Su, Peidong Yang, A. Paul Alivisatos, and Stephen R. Leone. Excitation-wavelength-dependent small polaron trapping of photoexcited carriers in $\alpha-Fe_2O_3$. *Nature Materials*, 16(8):819–825, August 2017.

95. Andrew R. Attar, Aditi Bhattacherjee, C. D. Pemmaraju, Kirsten Schnorr, Kristina D. Closser, David Prendergast, and Stephen R. Leone. Femtosecond x-ray spectroscopy of an electrocyclic ring-opening reaction. *Science*, 356(6333):54–59, April 2017.

96. Shashank Pathak, Lea M. Ibele, Rebecca Boll, Carlo Callegari, Alexander Demidovich, Benjamin Erk, Raimund Feifel, Ruaridh Forbes, Michele Di Fraia, Luca Giannessi, Christopher S. Hansen, David M. P. Holland, Rebecca A. Ingle, Robert Mason, Oksana Plekan, Kevin C. Prince, Arnaud Rouzée, Richard J. Squibb, Jan Tross, Michael N. R. Ashfold, Basile F. E. Curchod, and Daniel Rolles. Tracking the ultraviolet-induced photochemistry of thiophenone during and after ultrafast ring opening. *Nature Chemistry*, 12(9):795–800, September 2020.

97. B Rethfeld, A Kaiser, M Vicanek, and GJPRB Simon. Ultrafast dynamics of nonequilibrium electrons in metals under femtosecond laser irradiation. *Physical Review B*, 65(21):214303, 2002.

98. BY Mueller and B Rethfeld. Relaxation dynamics in laser-excited metals under nonequilibrium conditions. *Physical Review B*, 87(3):035139, 2013.

99. Hong Tang, Mingze Bai, Yusheng Dou, Qi Ran, and Glenn V Lo. Computer simulations of laser-induced melting of aluminum. *Nuclear Instruments and Methods in Physics Research Section B: Beam Interactions with Materials and Atoms*, 301:36–40, 2013.

100. Alexander JE Rettie, William D Chemelewski, David Emin, and C Buddie Mullins. Unravelling small-polaron transport in metal oxide photoelectrodes. *The journal of physical chemistry letters*, 7(3):471–479, 2016.

101. David Emin. *Polarons*. Cambridge University Press, 2013.

102. Isabel M Klein, Hanzhe Liu, Danika Nimlos, Alex Krotz, and Scott Kevin Cushing. Ab initio prediction of excited-state and polaron effects in transient xuv measurements of α-Fe_2O_3. *Journal of the American Chemical Society*, 144(28):12834–12841, 2022.

103. S Sonntag, J Roth, F Gaehler, and H-R Trebin. Femtosecond laser ablation of aluminium. *Applied surface science*, 255(24):9742–9744, 2009.

104. Jan Winter, Stephan Rapp, Maximilian Spellauge, Constanze Eulenkamp, Michael Schmidt, and Heinz P Huber. Ultrafast pump-probe ellipsometry and microscopy reveal the surface

dynamics of femtosecond laser ablation of aluminium and stainless steel. *Applied Surface Science*, 511:145514, 2020.

105. Johannes Roth, Steffen Sonntag, Johannes Karlin, Carolina Trichet Paredes, Marc Sartison, Armin Krauß, and Hans-Rainer Trebin. Molecular dynamics simulations studies of laser ablation in metals. In *AIP Conference Proceedings*, volume 1464, pages 504–523. American Institute of Physics, 2012.

106. Masahiro Okazaki, Akihiro Furube, and Liang-Yih Chen. Charge generation dynamics in hematite photoanodes decorated with gold nanostructures under near infrared excitation. *The Journal of Chemical Physics*, 152(4):041106, 2020.

107. Li Dong, Hongwei Chu, Ying Li, Shengzhi Zhao, Guiqiu Li, and Dechun Li. Nonlinear optical responses of α-Fe_2O_3 nanosheets and application as a saturable absorber in the wide near-infrared region. *Optics & Laser Technology*, 136:106812, 2021.

108. Maxim V Shugaev, Chengping Wu, Oskar Armbruster, Aida Naghilou, Nils Brouwer, Dmitry S Ivanov, Thibault J-Y Derrien, Nadezhda M Bulgakova, Wolfgang Kautek, Baerbel Rethfeld, et al. Fundamentals of ultrafast laser–material interaction. *Mrs Bulletin*, 41(12):960–968, 2016.

109. Fuyuki Shimojo, Aiichiro Nakano, Rajiv K Kalia, and Priya Vashishta. Electronic processes in fast thermite chemical reactions: A first-principles molecular dynamics study. *Physical Review E*, 77(6):066103, 2008.

110. John Vinson. Advances in the ocean-3 spectroscopy package. *Physical Chemistry Chemical Physics*, 24(21):12787–12803, 2022.

111. J Vinson, JJ Rehr, JJ Kas, and EL Shirley. Bethe-salpeter equation calculations of core excitation spectra. *Physical Review B*, 83(11):115106, 2011.

112. Paolo Giannozzi, Stefano Baroni, Nicola Bonini, Matteo Calandra, Roberto Car, Carlo Cavazzoni, Davide Ceresoli, Guido L Chiarotti, Matteo Cococcioni, Ismaila Dabo, et al. Quantum espresso: a modular and open-source software project for quantum simulations of materials. *Journal of physics: Condensed matter*, 21(39):395502, 2009.

113. John P Perdew, Kieron Burke, and Matthias Ernzerhof. Generalized gradient approximation made simple. *Physical review letters*, 77(18):3865, 1996.

114. Satoshi Tanaka and Shaul Mukamel. X-ray four-wave mixing in molecules. *The Journal of chemical physics*, 116(5):1877–1891, 2002.

115. Shaul Mukamel. Multiple core-hole coherence in x-ray four-wave-mixing spectroscopies. *Physical Review B*, 72(23):235110, 2005.

116. Sharon Shwartz, Matthias Fuchs, JB Hastings, Y Inubushi, T Ishikawa, T Katayama, DA Reis, T Sato, K Tono, M Yabashi, et al. X-ray second harmonic generation. *Physical review letters*, 112(16):163901, 2014.

117. Emily Sistrunk, Jakob Grilj, Jaewoo Jeong, Mahesh G Samant, Alexander X Gray, Hermann A Dürr, Stuart SP Parkin, and Markus Gühr. Broadband extreme ultraviolet probing of transient gratings in vanadium dioxide. *Optics express*, 23(4):4340–4347, 2015.

118. F Bencivenga, R Cucini, Flavio Capotondi, A Battistoni, R Mincigrucci, E Giangrisostomi, A Gessini, M Manfredda, IP Nikolov, E Pedersoli, et al. Four-wave mixing experiments with extreme ultraviolet transient gratings. *Nature*, 520(7546):205–208, 2015.

119. Royce K Lam, SL Raj, TA Pascal, CD Pemmaraju, L Foglia, A Simoncig, N Fabris, P Miotti, CJ Hull, AM Rizzuto, et al. Soft x-ray second harmonic generation as an interfacial probe. *Physical review letters*, 120(2):023901, 2018.

120. Jeremy R Rouxel, Danny Fainozzi, Roman Mankowsky, Benedikt Rösner, Gediminas Seniutinas, Riccardo Mincigrucci, Sara Catalini, Laura Foglia, Riccardo Cucini, Florian Döring, et al. Hard x-ray transient grating spectroscopy on bismuth germanate. *Nature Photonics*, 15(7):499–503, 2021.

121. Horst Rottke, Robin Y Engel, Daniel Schick, Jan O Schunck, Piter S Miedema, Martin C Borchert, Marion Kuhlmann, Nagitha Ekanayake, Siarhei Dziarzhytski, Günter Brenner, et al. Probing electron and hole colocalization by resonant four-wave mixing spectroscopy in the extreme ultraviolet. *Science advances*, 8(20):eabn5127, 2022.

122. Filippo Bencivenga, Marco Zangrando, Cristian Svetina, Alessandro Abrami, Andrea Battistoni, Roberto Borghes, Flavio Capotondi, Riccardo Cucini, Francesco Dallari, Miltcho Danailov, et al. Experimental setups for fel-based four-wave mixing experiments at fermi. *Journal of Synchrotron Radiation*, 23(1):132–140, 2016.

123. Flavio Capotondi, Emanuele Pedersoli, Filippo Bencivenga, Michele Manfredda, Nicola Mahne, Lorenzo Raimondi, Cristian Svetina, Marco Zangrando, Alexander Demidovich, Ivaylo Nikolov, et al. Multipurpose end-station for coherent diffraction imaging and scattering at fermi@ elettra free-electron laser facility. *Journal of synchrotron radiation*, 22(3):544–552, 2015.

124. Emanuele Pedersoli, Flavio Capotondi, Daniele Cocco, Marco Zangrando, Burkhard Kaulich, Ralf H Menk, Andrea Locatelli, Tevfik O Mentes, Carlo Spezzani, Gilio Sandrin, et al. Multipurpose modular experimental station for the diproi beamline of fermi@ elettra free electron laser. *Review of Scientific Instruments*, 82(4), 2011.

125. Stephen M Durbin. X-ray induced optical reflectivity. *AIP Advances*, 2(4), 2012.

126. Yu Zhang, Daniel Healion, Jason D Biggs, and Shaul Mukamel. Double-core excitations in formamide can be probed by x-ray double-quantum-coherence spectroscopy. *The Journal of Chemical Physics*, 138(14), 2013.

127. Shaul Mukamel, Daniel Healion, Yu Zhang, and Jason D Biggs. Multidimensional attosecond resonant x-ray spectroscopy of molecules: Lessons from the optical regime. *Annual review of physical chemistry*, 64:101–127, 2013.

128. VI Gavrilenko and F Rebentrost. Nonlinear optical susceptibility of the surfaces of silicon and diamond. *Surface science*, 331:1355–1360, 1995.

129. F Trojánek, K Žídek, B Dzurňák, M Kozák, and P Malỳ. Nonlinear optical properties of nanocrystalline diamond. *Optics Express*, 18(2):1349–1357, 2010.

130. Sean Reilly, Vasili G Savitski, Hangyu Liu, Stuart Reid, Des Gibson, Harpreet Dhillon, Stefan Olsson Robbie, Erdan Gu, Martin D Dawson, Andrew Bennett, et al. Laser induced

damage threshold of cvd-grown single crystal diamond surfaces with various surface finishes. In *Advanced Solid State Lasers*, pages ATu2A–6. Optica Publishing Group, 2015.

131. ID Abella, NA Kurnit, and SR Hartmann. Photon echoes. *Physical review*, 141(1):391, 1966.

132. Riccardo Mincigrucci, Emiliano Principi, Filippo Bencivenga, Laura Foglia, Alessandro Gessini, Gabor Kurdi, Alberto Simoncig, and Claudio Masciovecchio. Transient euv reflectivity measurements of carbon upon ultrafast laser heating. In *Photonics*, volume 4, page 23. MDPI, 2017.

133. SA Solin and AK Ramdas. Raman spectrum of diamond. *Physical Review B*, 1(4):1687, 1970.

134. Iestyn Pope, Lukas Payne, George Zoriniants, Evan Thomas, Oliver Williams, Peter Watson, Wolfgang Langbein, and Paola Borri. Coherent anti-stokes raman scattering microscopy of single nanodiamonds. *Nature nanotechnology*, 9(11):940–946, 2014.

135. A Laubereau, D Von der Linde, and W_ Kaiser. Direct measurement of the vibrational lifetimes of molecules in liquids. *Physical review letters*, 28(18):1162, 1972.

136. A Laubereau and W Kaiser. Vibrational dynamics of liquids and solids investigated by picosecond light pulses. *Reviews of Modern Physics*, 50(3):607, 1978.

137. Tsung-Yu Chen, Yu-Tung Chen, Cheng-Liang Wang, Ivan M Kempson, Wah-Keat Lee, Yong S Chu, Y Hwu, and G Margaritondo. Full-field microimaging with 8 kev x-rays achieves a spatial resolutions better than 20 nm. *Optics express*, 19(21):19919–19924, 2011.

138. HJ Leamy. Charge collection scanning electron microscopy. *Journal of Applied Physics*, 53(6):R51–R80, 1982.

139. Ludwig Reimer. *Scanning electron microscopy: physics of image formation and microanalysis*, volume 45. Springer, 1985.

140. Daniel Rugar and Paul Hansma. Atomic force microscopy. *Physics today*, 43(10):23–30, 1990.

141. Werner Kühlbrandt. Cryo-em enters a new era. *elife*, 3:e03678, 2014.

142. Takanori Nakane, Abhay Kotecha, Andrija Sente, Greg McMullan, Simonas Masiulis, Patricia MGE Brown, Ioana T Grigoras, Lina Malinauskaite, Tomas Malinauskas, Jonas Miehling, et al. Single-particle cryo-em at atomic resolution. *Nature*, 587(7832):152–156, 2020.

143. Mengyu Wu, Gabriel C Lander, and Mark A Herzik Jr. Sub-2 angstrom resolution structure determination using single-particle cryo-em at 200 kev. *Journal of Structural Biology: X*, 4:100020, 2020.

144. G Toraldo Di Francia. Super-gain antennas and optical resolving power. *Il Nuovo Cimento (1943-1954)*, 9:426–438, 1952.

145. Stefan W Hell and Jan Wichmann. Breaking the diffraction resolution limit by stimulated emission: stimulated-emission-depletion fluorescence microscopy. *Optics letters*, 19(11):780–782, 1994.

146. Mickaël Lelek, Melina T Gyparaki, Gerti Beliu, Florian Schueder, Juliette Griffié, Suliana Manley, Ralf Jungmann, Markus Sauer, Melike Lakadamyali, and Christophe Zimmer. Single-molecule localization microscopy. *Nature Reviews Methods Primers*, 1(1):39, 2021.

147. Susanne CM Reinhardt, Luciano A Masullo, Isabelle Baudrexel, Philipp R Steen, Rafal Kowalewski, Alexandra S Eklund, Sebastian Strauss, Eduard M Unterauer, Thomas Schlichthaerle, Maximilian T Strauss, et al. Ångström-resolution fluorescence microscopy. *Nature*, 617(7962):711–716, 2023.

148. Mats GL Gustafsson. Surpassing the lateral resolution limit by a factor of two using structured illumination microscopy. *Journal of microscopy*, 198(2):82–87, 2000.

149. Mats GL Gustafsson, Lin Shao, Peter M Carlton, CJ Rachel Wang, Inna N Golubovskaya, W Zacheus Cande, David A Agard, and John W Sedat. Three-dimensional resolution doubling in wide-field fluorescence microscopy by structured illumination. *Biophysical journal*, 94(12):4957–4970, 2008.

150. Rainer Heintzmann and Christoph G Cremer. Laterally modulated excitation microscopy: improvement of resolution by using a diffraction grating. In *Optical biopsies and microscopic techniques III*, volume 3568, pages 185–196. SPIE, 1999.

151. Rainer Heintzmann and Thomas Huser. Super-resolution structured illumination microscopy. *Chemical reviews*, 117(23):13890–13908, 2017.

152. Riccardo Mincigrucci, Ettore Paltanin, Jacopo Stefano Pelli Cresi, Laura Foglia, Dario De Angelis, Danny Fainozzi, Alessandro Gessini, Daniel Santiago Penagos Molina, Ondrej Stranik, Felix Wechsler, Rainer Heintzmann, Filippo Bencivenga, and Claudio Masciovecchio. First step towards structured illumination microscopy with extreme ultraviolet pulses [in preparation].

153. Benedikt Günther, Lorentz Hehn, and Franz" Pfeiffer. Full-field structured illumination super-resolution x-ray transmission microscopy. *Nature Communications*, 10:2494, 2019.

154. Henry Fox Talbot. Lxxvi. facts relating to optical science. no. iv. *The London, Edinburgh, and Dublin Philosophical Magazine and Journal of Science*, 9(56):401–407, 1836.

155. Ren-yuan Zhu. Radiation damage in scintillating crystals. *Nuclear Instruments and Methods in Physics Research Section A: Accelerators, Spectrometers, Detectors and Associated Equipment*, 413(2-3):297–311, 1998.

156. Martin Nikl, Eva Mihokova, Valentin Laguta, Jan Pejchal, Stefania Baccaro, and Anna Vedda. Radiation damage processes in complex-oxide scintillators. In *Damage to VUV, EUV, and X-ray Optics*, volume 6586, pages 98–110. SPIE, 2007.

157. P Novotnỳ and V Linhart. Radiation damage study of thin yag: Ce scintillator using low-energy protons. *Journal of Instrumentation*, 12(07):P07021, 2017.

158. Valentin Viktorovich Lider. X-ray crystal interferometers. *Physics-Uspekhi*, 57(11):1099, 2014.

159. E Burkel, J Peisl, and B Dorner. Observation of inelastic x-ray scattering from phonons. *Europhysics Letters*, 3(8):957, 1987.

160. Christophe Nicolas and Catalin Miron. Lifetime broadening of core-excited and-ionized states. *Journal of Electron Spectroscopy and Related Phenomena*, 185(8-9):267–272, 2012.

161. Satoshi Matsuyama, Jumpei Yamada, Yoshiki Kohmura, Makina Yabashi, Tetsuya Ishikawa, and Kazuto Yamauchi. Full-field x-ray fluorescence microscope based on total-reflection advanced kirkpatrick–baez mirror optics. *Optics express*, 27(13):18318–18328, 2019.

162. Carlos Sanchez-Cano, Isolda Romero-Canelón, Yang Yang, Ian J Hands-Portman, Sylvain Bohic, Peter Cloetens, and Peter J Sadler. Synchrotron x-ray fluorescence nanoprobe reveals target sites for organo-osmium complex in human ovarian cancer cells. *Chemistry–A European Journal*, 23(11):2512–2516, 2017.

163. Koen Janssens, G Vittiglio, I Deraedt, A Aerts, Bart Vekemans, Laszlo Vincze, F Wei, I De Ryck, O Schalm, F Adams, et al. Use of microscopic xrf for non-destructive analysis in art and archaeometry. *X-Ray Spectrometry: An International Journal*, 29(1):73–91, 2000.

164. Elias Diesen, Hsin-Yi Wang, Simon Schreck, Matthew Weston, Hirohito Ogasawara, Jerry LaRue, Fivos Perakis, Martina DellÁngela, Flavio Capotondi, Luca Giannessi, et al. Ultrafast adsorbate excitation probed with subpicosecond-resolution x-ray absorption spectroscopy. *Physical Review Letters*, 127(1):016802, 2021.

165. Jerry LaRue, Boyang Liu, Gabriel LS Rodrigues, Chang Liu, Jose Antonio Garrido Torres, Simon Schreck, Elias Diesen, Matthew Weston, Hirohito Ogasawara, Fivos Perakis, et al. Symmetry-resolved co desorption and oxidation dynamics on o/ru (0001) probed at the c k-edge by ultrafast x-ray spectroscopy. *The Journal of Chemical Physics*, 157(16), 2022.

166. CT Campbell, G Ertl, H Kuipers, and J Segner. A molecular beam study of the catalytic oxidation of co on a pt (111) surface. *The Journal of Chemical Physics*, 73(11):5862–5873, 1980.

167. Rustem Kecili and Chaudhery Mustansar Hussain. Mechanism of adsorption on nanomaterials. In *Nanomaterials in chromatography*, pages 89–115. Elsevier, 2018.

168. HJ Eichler, U Klein, and D Langhans. Coherence time measurement of picosecond pulses by a light-induced grating method. *Applied physics*, 21:215–219, 1980.

169. Christoph Leithold, Jan Reislöhner, Holger Gies, and Adrian N Pfeiffer. Characterization of two ultrashort laser pulses using interferometric imaging of self-diffraction. *Optics Letters*, 42(24):5246–5249, 2017.

170. Rick Trebino, Eric K Gustafson, and Anthony E Siegman. Fourth-order partial-coherence effects in the formation of integrated-intensity gratings with pulsed light sources. *JOSA B*, 3(10):1295–1304, 1986.

171. T Rappen, U Peter, M Wegener, and W Schäfer. Coherent dynamics of continuum and exciton states studied by spectrally resolved fs four-wave mixing. *Physical Review B*, 48(7):4879, 1993.

172. Nikita Medvedev, U Zastrau, E Förster, Dirk O Gericke, and B Rethfeld. Short-time electron dynamics in aluminum excited by femtosecond extreme ultraviolet radiation. *Physical Review Letters*, 107(16):165003, 2011.

Appendix A

Fits

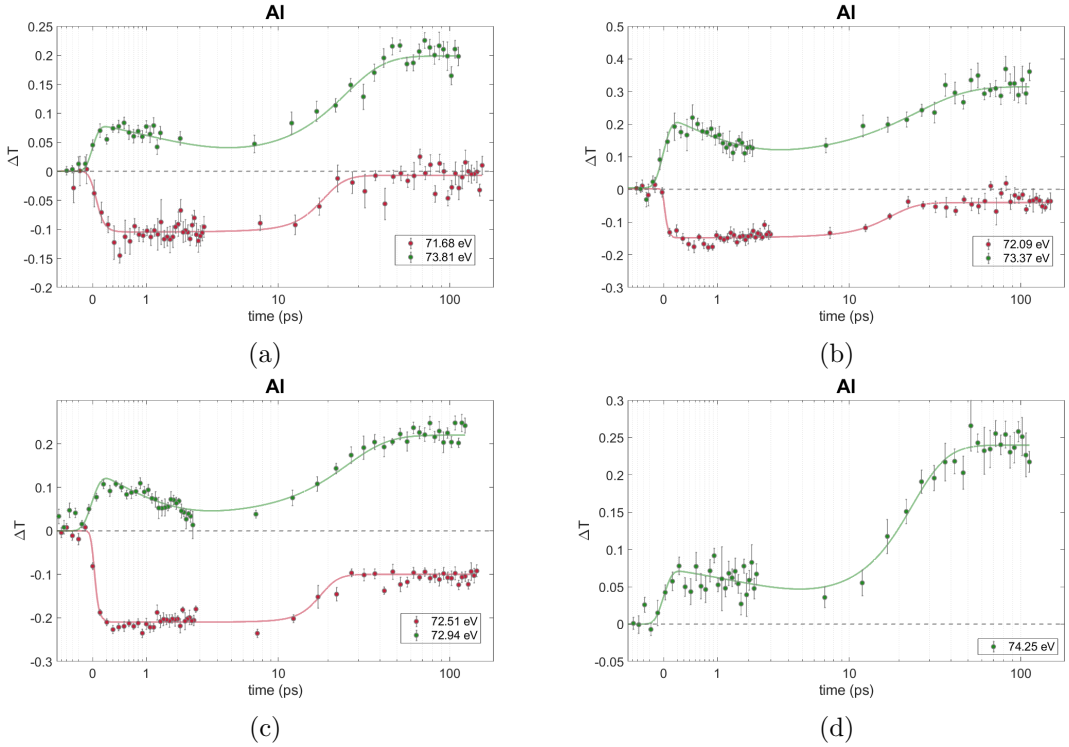

Figure A.1: Dynamics of the different photon energies measured across Al $L_{2,3}$ absorption edge with their associated fits.

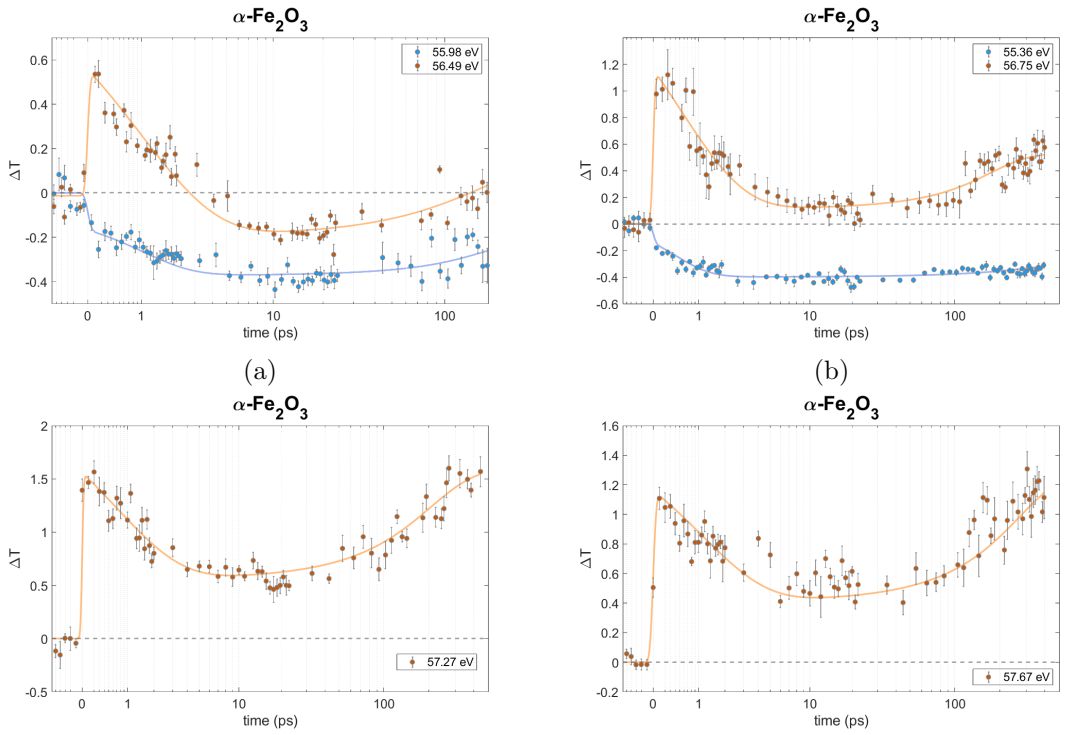

Figure A.2: Dynamics of the different photon energies measured across Fe $M_{2,3}$ absorption edge with their associated fits.

Acknowledgements

In the first place, I would like to aknowledge the SMART-X network, which funded my PhD theough the European Union's Horizon 2020 research and innovation program under the Marie Skłodowska-Curie Grant Agreement No. 860553. I would like to make a particular mention to the coordinator of the network and my mentor, Caterina Vozzi, whose efforts have made this collective networking experience possible and to Egle Molotokaite, the project manager, who helped me in these years with all the administrative and organizational issues.

I would like to thank the collaborators from CALTECH, Scott K. Cushing and Wonseok Lee, that have been available to work on two different projects with our group, the study of thermite reaction and the self-diffraction of Co.

I would like to thank Alexei Maznev from MIT and Dmitriy Ksenzov from University of Siegen, to allow me to work with them on the self-diffractin project on Co.

I would like to thank my supervisor, Claudio Masciovecchio, for the opportunity of joining the FERMI team for the past three years, and the whole FERMI team for the support and the positive energy I have benefit along the way. More than everybody else, I would like to thank Riccardo Mincigrucci, for pushing me to grow as a scientist and for guiding me through the whole journey of the PhD, both in the funny and in the stressful moments, relentlessly available for answering my questions at whatever time of the day and of the night (referring here to the night shifts of the beamtimes) and for having some good time at work as well as outside. I will always keep a pleasant memory of our peripatetic open-air meetings, where we talked about science while having a healthy walk in the woods around Elettra. A very special thanks to Jacopo Stefano Pelli Cresi, who had hold my hand in the first part of my PhD and has helped me to move my first steps towards becoming (almost) independent, and to Valentina Pastorello, who started together with me the adventure at Elettra, sharing the struggle and making the working environment so pleasant; you both have become the dearest friends.

Thanks to the current and former members of the EIS team, Dario, Laura, Filippo, Emiliano, Marija, Zeinab, Den, where I have found my self at home, always received positive feedbacks to my questions and curiosities and shared pleasant moment at the coffee machine as well as hard times on the beamlines.

A warm thanks goes to Cristian Svetina, with whom I had the privilege of collaborating in the XTG beamtime at XFEL and te crosspol beamtime at FERMI, I learned a lot on how to make a working place pleasant, fun and efficient at the same time.

Thanks to my more recent office mates, Wibke, Manuel and Nupur, with which I have had some nice chats and some high-quality cups of tea. I cannot avoid saying a huge thank to Denny, 'the captain' of our office crew, who never 'left the ship', and granted me several times with his providential advice on the PhD administrative issues and his good company.

Maybe the biggest thank of all, goes to all the friends and people that I met outside work (too many to mention all of them and I am also too afraid of forgetting somebody), who have made my personal life good, which, at the end of the day, it is the most important of all things.

Last, but not least, I would like to thank my parents, who supported me and gave me the chance of getting here, where I have arrived today.